

Dissertation
submitted to the
Combined Faculty of Mathematics, Engineering and Natural Sciences
of Heidelberg University, Germany
for the degree of
Doctor of Natural Sciences

Put forward by
Lynn Buchele
born in: Lamar, CO, USA
Oral examination: May 28th, 2025

Asteroseismic Structure Inversions of Solar-like Oscillators

Lynn Lou Buchele

SUPERVISOR

Prof. Dr. ir. Saskia Hekker

EXAMINATION COMMITTEE

Prof. Dr. ir. Saskia Hekker (referee)
Priv.-Doz. Dr. Coryn Bailer-Jones (referee)
Prof. Dr. Matthias Bartelmann
Priv.-Doz. Dr. Sabine Reffert

And I will bloom here in my room
With a little water and a little bit of sunlight
And a little bit of tender mercy, tender mercy
Absolute Lithops Effect, The Mountain Goats

Summary

The study of stars through their global oscillations, i.e., asteroseismology, has provided unprecedented insight into stellar interiors. One of the most powerful techniques of asteroseismology is that of structure inversions. This technique can localize and quantify differences in sound speed between a star and its best-fit model. These differences, then, are a direct test of the accuracy of our stellar models.

The first part of this thesis outlines the specifics of the inversion procedure and then applies it to 55 main-sequence stars observed by the *Kepler* mission with masses between 1 and $1.6M_{\odot}$. This discussion is split into stars with radiative and convective cores. Overall, the inversions reveal that our best-fit models match the sound speed profile in around half of the stars studied. In the remaining half of the sample, there is an even split between cases where the model sound speed is too high and cases where it is too low.

The second part of this thesis explores whether current inversion techniques are suitable for subgiant stars. These stars exhibit mixed modes that are sensitive to deeper regions of stellar cores. As the sensitivity of these mixed modes changes on a very short timescale, obtaining reliable inversion results will require modifications to current techniques.

Zusammenfassung

Die Erforschung von Sternen anhand ihrer globalen Schwingungen, auch bekannt als Asteroseismologie, hat einen noch nie dagewesenen Einblick in das Innere von Sternen ermöglicht. Eine der leistungsfähigsten Techniken der Asteroseismologie sind sogenannte Strukturinversionen. Mit dieser Technik lassen sich Unterschiede in der Schallgeschwindigkeit zwischen einem Stern und einem bestmöglich angepassten Referenzmodell lokalisieren und quantifizieren. Diese Unterschiede sind ein direkter Test für die Genauigkeit unserer Sternmodelle.

Der erste Teil dieser Arbeit beschreibt die Einzelheiten des Inversionsverfahrens und wendet dieses dann auf 55 von der Kepler-Mission beobachtete Hauptreihensterne mit Massen zwischen 1 und $1,6 M_{\odot}$ an. Die Diskussion wird in Sterne mit radiativen und konvektiven Kernen unterteilt. Insgesamt zeigen die Inversionen, dass unsere Referenzmodelle bei etwa der Hälfte der untersuchten Sterne mit dem beobachteten Schallgeschwindigkeitsprofil übereinstimmen. In der verbleibenden Hälfte der Stichprobe gibt es eine gleichmäßige Verteilung zwischen Fällen, in denen die Schallgeschwindigkeit des Referenzmodells zu hoch ist, und Fällen, in denen sie zu niedrig ist.

Im zweiten Teil dieser Arbeit wird untersucht, ob die derzeit verwendeten Inversionstechniken für Unterriesensterne geeignet sind. Diese Sterne weisen gemischte Schwingungsmoden auf, die auch die Untersuchung von tieferen Regionen im Kern des Sterns ermöglichen. Da sich die Empfindlichkeit dieser gemischten Moden auf einer sehr kurzen Zeitskala entwickelt, müssen die derzeit verwendeten Techniken modifiziert werden, um zuverlässige Inversionsergebnisse zu erhalten.

List of physical constants

Symbol	Name	Value in cgs units
G	Gravitational constant	$6.6743 \times 10^{-8} \text{ g}^{-1} \cdot \text{cm}^3 \cdot \text{s}^{-2}$
c_l	Speed of light in a vacuum	$2.99792458 \times 10^{10} \text{ cm} \cdot \text{s}^{-1}$
a	Radiation density constant	$7.565733 \times 10^{-15} \text{ erg} \cdot \text{cm}^{-3} \cdot \text{K}^{-4}$
M_{\odot}	Solar mass	$1.9884099 \times 10^{33} \text{ g}$
R_{\odot}	Solar radius	$6.957 \times 10^{10} \text{ cm}$
L_{\odot}	Solar luminosity	$3.828 \times 10^{33} \text{ erg} \cdot \text{s}^{-1}$
$T_{\text{eff},\odot}$	Solar effective temperature	5777 K
$\nu_{ac,\odot}$	Solar acoustic cutoff frequency	5000 μHz

Contents

Summary	vii
Zusammenfassung	vii
List of physical constants	ix
1 Context and theoretical background	1
1.1 Introduction and Motivation	1
1.2 Stellar Modeling	5
1.2.1 Equations of Stellar Structure	5
1.2.2 Constructing a Stellar Model	7
1.3 Asteroseismology	8
1.3.1 Oscillation Equations	8
1.3.2 Types of Modes	11
1.3.3 Asteroseismic modeling	14
1.3.4 Best-fit Asteroseismic Models	18
1.4 Structure Inversions	18
1.4.1 Mode Kernels	19
1.4.2 OLA Inversions	21
1.5 Summary of Thesis	26
2 Inversions of Main-sequence Stars with Radiative Cores	27
2.1 Introduction	28
2.2 Forward Modeling	29
2.3 Inversions	30
2.3.1 Localized averaging kernels	31
2.3.2 Trade-off parameters	32
2.3.3 Stellar mass & radius	33
2.3.4 Overall inversion significance	33
2.4 Results and Discussion	34
2.4.1 Individual Stars	38
2.4.2 Exploring the effects of microphysics	38
2.5 Conclusions	41

3	Inversions of Main-sequence Stars with Convective Cores	43
3.1	Introduction	44
3.2	Forward Modeling	44
3.3	Structure Inversions	47
3.4	Results	49
3.4.1	KIC 6225718	49
3.4.2	KIC 10162436 and KIC 5773345	52
3.4.3	KIC 11807274	53
3.4.4	Changes in Input Physics	53
3.5	Conclusions	56
4	Linearity of Structure Kernels	59
4.1	Introduction	60
4.2	Kernels and Inversions	61
4.3	Main-Sequence Stars	62
4.3.1	Kernel Errors	62
4.3.2	OLA Inversions	63
4.4	Subgiant Stars	65
4.4.1	Kernel Errors	65
4.4.2	OLA Inversions	69
4.5	Conclusions	69
5	Conclusions and Outlook	73
5.1	Main-sequence Solar-like Oscillators	73
5.2	Evolved Solar-like Oscillators	74
A	Appendix for Chapter 1: Context and Background	77
A.1	Derivation of Kernels	77
A.1.1	$\Gamma_{1,\rho}$ Kernels	84
A.1.2	u, Y Kernels	85
B	Appendices for Chapter 2: Inversions of Main-sequence Stars with Radiative Cores	87
B.1	Reference Model Parameters	87
B.2	Inversion Details	87
B.2.1	Inversion Parameter Selection	87
B.2.2	Mean Density Scaling	89
B.2.3	Sun as a star	90
B.3	Full Inversion Results	92
C	Appendices for Chapter 3: Inversions of Main-sequence Stars with Convective Cores	97
C.1	Appendix Modeling Details	97
C.1.1	Model Grids	97
C.1.2	Modeling Information	98

D Appendices for Chapter 4: Linearity of Structure Kernels	103
D.1 Propagation of Kernel Errors	103
D.2 Subgiant Higher Degree Modes and Singularity	103
D.2.1 Higher degree modes	103
D.2.2 Singularity	104
List of publications	109
Bibliography	111
Acknowledgments	127



Context and theoretical background

1.1. Introduction and Motivation

As the source of much of the light we observe, stars play an important role in our understanding of the universe. By better understanding stars, we are able to increase our understanding of other astrophysical systems. Exoplanet properties such as mass, radius, and age are inferred from the properties of the host star. Better age determinations of the various stellar populations in the Milky Way help to reconstruct the history of our galaxy. On even larger scales, variable stars and supernovas form important rungs on the distance ladder used to measure cosmological distances. Fully understanding stellar interiors and evolution requires proper descriptions for a wide range of physical phenomena. This is particularly challenging as the physics happening in stars spans a wide range of scales, both in space and time.

Stars are a diverse group of objects, differing in their mass, age, composition, rotation, and interaction history with other stars and/or planets. Regardless of the kind of star, we are limited to observing only the light emitted from the stellar surface¹. Fortunately, the light of stars provides a wealth of information that can be extracted by astronomers, including:

- **Brightness:** The intrinsic brightness of a star is an important indication of the mass and/or evolutionary stage of the star. However, we are only able to observe the apparent brightness. In order to determine the intrinsic brightness, the distance to the star must be known. For the nearby stars, such as those considered in this thesis, this is often found using their parallaxes as measured by the Gaia satellite (Gaia Collaboration et al., 2016, 2018; Creevey et al., 2023).
- **Spectrum:** The pattern of absorption and emission lines in the stellar spectrum provides information about the temperature and atomic elements present at the stellar surface. High-resolution spectroscopy can be used to determine the effective temperature of a star as well as its composition. Typically, the surface composition is given in terms of an overall metallicity $[M/H]$ or parametrized by the iron abundance $[Fe/H]$,

¹Gravitational waves provide another avenue, however, at present gravitational waves are detected from merges of black holes or neutron stars.

although detailed spectroscopic analysis can provide the abundances of many different individual atomic elements. The spectroscopic data for the stars discussed here are taken from several ground-based surveys (Furlan et al., 2018; Mathur et al., 2017; Morel et al., 2021).

- **Polarization:** The light emitted by stars can be polarized by a magnetic field at the stellar surface. This polarization combined with detailed spectroscopic analysis of the Zeeman splittings of atomic lines can be used to measure the strength of surface magnetic fields.
- **Variation:** Stellar brightness and spectra are not constant over time. These changes can be single-time events, such as a supernova at the end of a massive star’s life. Other changes, however, are recurring, such as those caused by orbital companions or stellar pulsations.

All of these observations are important to our understanding of stellar evolution theory. This thesis focuses on the variation due to intrinsic global oscillation modes. The power of these observations stems from the fact that unlike the luminosity, effective temperature, and surface composition, the oscillation modes are directly sensitive to the interior structure of a star. This makes these oscillation modes the best way, at present, to test and improve our understanding of stellar interiors.

Many stars oscillate due to a variety of different mechanisms, as can be seen in Figure 1.1. These oscillations can be classified by the restoring force of the mode and also by the mechanism which excites the oscillation. This work concentrates on solar-like oscillators. As the name suggests, the archetypal example of this class of oscillators is our Sun, which exhibits oscillation modes with periods of around 5 minutes. These modes are excited by turbulence in the outer convection zone (Leighton et al., 1962; Evans and Michard, 1962; Claverie et al., 1979). Any star with a convective envelope is expected to exhibit these solar-like oscillations, even if the overall structure differs from that of the Sun. These stars can exist across a range of masses and evolutionary stages including²:

- **Main-sequence stars:** Stars with masses roughly between 0.8 and $1.5M_{\odot}$ have an outer convection zone during the main sequence and thus exhibit solar-like oscillations. This category includes stars with both radiative and convective cores, with the crossover occurring at roughly $1.2M_{\odot}$, depending on composition.
- **Subgiant stars:** As stars with $M \lesssim 1.1M_{\odot}$ exhaust the hydrogen in their cores, the core begins to contract as the envelope expands and the star enters a short-lived evolutionary stage known as the subgiant branch. This is the low-mass equivalent to the Hertzsprung gap stage in more massive stars. In contrast to the Hertzsprung gap, stars spend enough of their lives in the subgiant branch that we expect to, and in fact, do, observe a significant number of stars in this stage.
- **Red giant branch stars:** Whether a star transitions from the end of the main sequence to the red giant branch star as a subgiant or by crossing the Hertzsprung gap, the structure of stars with $M \lesssim 10M_{\odot}$ are similar. These stars are fueled by a layer of hydrogen shell burning in the interior and have deep convective envelopes in the outer layers.

²For a more detailed description of the evolution of these stars see Hekker and Christensen-Dalsgaard (2017).

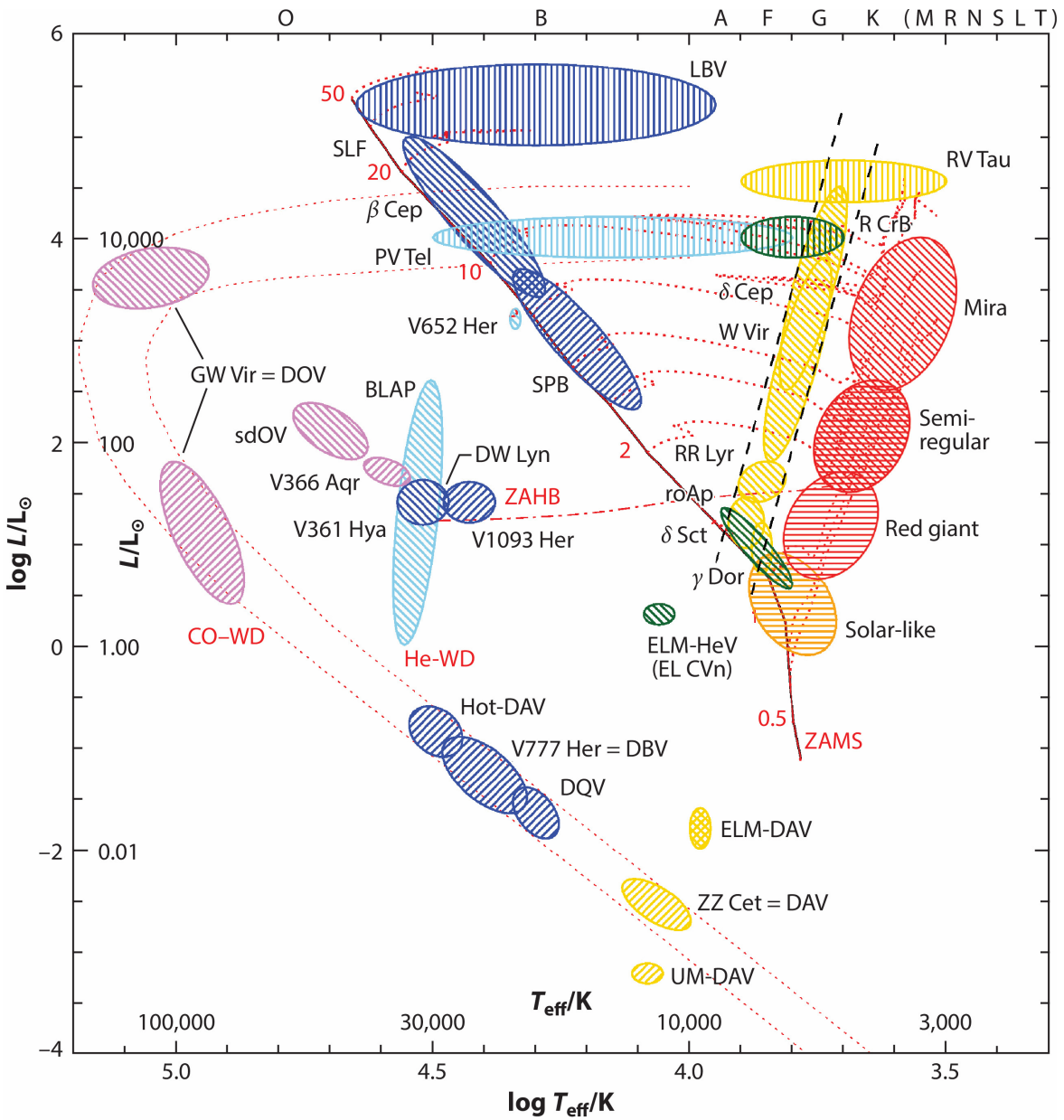
- Red clump/ Secondary clump: When the core temperature of the star is high enough, it will begin to burn helium. For lower-mass stars ($M \lesssim 2M_{\odot}$) helium burning begins suddenly due to the degenerate core. The star then enters the red clump. In more massive stars, helium burning begins more gradually, and the stars enter what is called the secondary clump. Both red clump and secondary clump stars have convective envelopes and hence they exhibit solar-like oscillations.

While red giants (including red-giant branch, red clump, and secondary clump stars) make up the vast majority of stars with observed solar-like oscillations, I focus on the two previous stages of evolution: the main sequence and subgiant branch. In addition to a general increased understanding of stellar evolution, studying these stars and improving our models of them is interesting for several reasons. First, as the oscillations are similar to those observed in the Sun, a number of techniques developed for helioseismology can be (relatively) easily applied to other solar-like oscillators.

Second, the current search for habitable exoplanets is focused on Earth-like planets orbiting Sun-like stars. The properties of exoplanets, including mass, radius, and age, are inferred relative to their host stars. Thus, increased precision and accuracy of our estimates of stellar mass, radius, and age is essential to know which planets are potentially habitable. Of these three stellar parameters, the most difficult to determine is the stellar age. As no observations directly probe the age, it must always be inferred from stellar models, where even small changes to the modeling physics result in significant age differences (e.g., Farnir et al., 2020).

Finally, although this work does not discuss red giant stars in detail, these stars must first evolve through the main sequence. Stellar processes on the main sequence, such as core boundary mixing, can carry forward onto the red giant branch and even all the way to the asymptotic giant branch (Bertelli et al., 1986). In this way, a better understanding of the main-sequence lives of these stars can improve age estimates of red giants used for galactic archaeology (e.g., Anders et al., 2023; Pinsonneault et al., 2025) and nucleosynthetic yields from asymptotic giant branch stars (Busso et al., 1999).

Asteroseismic observations of solar-like oscillators can be used to infer estimates of the stellar mass and radius directly through scaling relations (Brown et al., 1991; Kjeldsen and Bedding, 1995). For detailed analysis of stellar interiors, however, these observations must be compared to stellar models. At present, even the best models are unable to fully reproduce the observed oscillation frequencies. These discrepancies suggest that our stellar models are not fully reproducing the interior of observed stars. The technique of structure inversions provides a way to use the differences in frequencies to infer the underlying structure differences. Before discussing the process of a structure inversion in detail, I begin by reviewing the equations of stellar structure and the process of obtaining stellar models. I then review the principles of asteroseismology and various approaches to finding best-fit asteroseismic models.



 Kurtz DW. 2022
Annu. Rev. Astron. Astrophys. 60:31–71

Figure 1.1: Hertzsprung-Russel Diagram showing the different classes of pulsating stars. For reference, the solid red line shows the zero-age main sequence. Evolutionary tracks for several masses up to the first red giant stage are shown by the red dotted lines. The Cepheid instability strip is bounded by the black dashed lines. The excitation mechanism and mode type of the oscillations are indicated by the hashing where (\\) indicates opacity-driven p-modes, (/) indicates opacity-driven g-modes, (≡) indicates stochastic oscillations, and (|||) indicates strange modes. The names of different classes of pulsators are taken from Aerts et al. (2010, their Chapter 2). Used with permission of Annual Review, from Kurtz (2022).

1.2. Stellar Modeling

In order to construct a stellar model, we first need to describe the physics of stars in a set of equations called the stellar structure equations. Here, I briefly review these equations in the form presented in Kippenhahn et al. (2013). For all the stellar models used in this work, I assume the star to be spherically symmetric.

1.2.1. Equations of Stellar Structure

1.2.1.1 Mass Continuity

The first equation of stellar structure describes how mass is distributed in the star. The way the structure variables change throughout the star can be described in terms of the mass coordinate, m , or the radial coordinate, r . These two coordinates are related through the density, ρ by the equation of mass continuity,

$$\frac{\partial r}{\partial m} = \frac{1}{4\pi r^2 \rho}. \quad (1.1)$$

1.2.1.2 Hydrostatic Equilibrium

In general, stars are assumed to be in hydrostatic equilibrium, meaning that the force of gravity is balanced by the pressure, P . This is expressed in the equation of hydrostatic equilibrium,

$$\frac{\partial P}{\partial m} = -\frac{Gm}{4\pi r^2}, \quad (1.2)$$

where G is the gravitational constant.

1.2.1.3 Energy Flux

In order for stars to continue emitting light, there must be an internal source of energy and this energy must be conserved throughout the star. The energy flux, l , is given by

$$\frac{\partial l}{\partial m} = \epsilon_n - \epsilon_\nu - \epsilon_g. \quad (1.3)$$

This equation accounts for several processes that can change l including nuclear reactions ϵ_n , neutrinos ϵ_ν , and gravitational potential changes due to expansion or contraction ϵ_g . This last term is

$$\epsilon_g = -T \frac{\partial s}{\partial r}, \quad (1.4)$$

where s is the specific entropy. The calculation of the partial derivative in Equation 1.4 requires knowledge of the equation of state of stellar material. While it is tempting to treat the stellar material as an ideal gas, there are a number of interaction forces that are not described by the ideal gas law including pressure ionization, van der Waals forces, crystallization, and other quantum interactions.

1.2.1.4 Energy Transport

Most of the energy of a star is generated from nuclear reactions in the interior of the star. This energy is then transported through the rest of the star either by convection or radiation, leading to the equation of energy transport:

$$\boxed{\frac{\partial T}{\partial m} = -\frac{GmT}{4\pi r^4 P} \nabla_T.} \quad (1.5)$$

Here T is the temperature and $\nabla_T = d \ln T / d \ln P$ is the temperature gradient. The exact form that ∇_T takes is dependent on the dominant type of energy transport. In stellar regions where radiation dominates

$$\nabla_T = \nabla_{\text{rad}} = \frac{3}{16\pi a c_l G} \frac{\kappa l P}{m T^4}, \quad (1.6)$$

where a is the radiation density constant, c_l is the speed of light, and κ is the mean opacity of the material (including both radiative and conductive opacity).

When energy is carried by convection, ∇_T is obtained from a full description of convection (or a simplified implementation). In convective regions that are deep in the stellar interior

$$\nabla_T = \nabla_{\text{ad}} = \left(\frac{P}{T} \frac{dT}{dP} \right)_s, \quad (1.7)$$

where the derivative dT/dP is taken with respect to constant specific entropy, s .

Whether a given region in a star is convective is determined using the temperature gradients introduced above and the chemical composition gradient,

$$\nabla_\mu = \frac{d \ln \mu}{d \ln P}, \quad (1.8)$$

where μ is the mean molecular weight. Under the Ledoux criterion, a region is stable against convection if

$$\nabla_{\text{rad}} < \nabla_{\text{ad}} + \nabla_\mu. \quad (1.9)$$

If this relation does not hold, then the region of the star is convective.

1.2.1.5 Composition Changes

The nuclear reactions responsible for generating the energy of a star also change the composition. The change in mass fraction X_i of the i th element due to nuclear reactions is given by

$$\boxed{\frac{\partial X_i}{\partial t} = \frac{m_i}{\rho} \left(\sum_j r_{ji} - \sum_k r_{ik} \right), i = 1, \dots, I} \quad (1.10)$$

In this equation, r_{ji} is the reaction rate or the number of reactions per unit volume per time that turn the j th element into the i th element and I is the total number of elements being tracked. The sum accounts for the fact that one element can be involved in several different reactions.

There are additional processes that can change the composition of a given part of the star by transporting material from another part of the star, either by convection or by diffusive processes such as gravitational settling or radiative acceleration.

1.2.1.6 Boundary Conditions

To solve the equations of stellar structure, it is necessary to specify a set of boundary conditions. One factor that complicates the process of obtaining a solution is that the boundary conditions are split between those applied to the center of the star ($m = 0$) and those applied at the surface ($m = M$). The central boundary conditions are quite clear, as we wish for regular behavior in the center of the star:

$$r(m = 0) = 0 \quad l(m = 0) = 0. \quad (1.11)$$

The outer boundary conditions are more complicated. The simplest approach is to assume that the temperature and pressure vanish at the stellar surface.

$$T(m = M) = 0 \quad P(m = M) = 0. \quad (1.12)$$

However, this is not strictly true, as the interstellar material has non-zero temperature and pressure. This also makes it difficult to define the stellar surface, where $r = R$. A common approach is to define the surface as the layer that emits most of the stellar radiation into space. This region is known as the photosphere and is defined as the location where the optical depth τ equals $2/3$. The values of temperature and pressure at the photosphere can then be given by a $T(\tau)$ relation, such as the Eddington gray atmosphere ($T^4(\tau) = 3/4T_{\text{eff}}^4(\tau + 2/3)$), or from precomputed tables obtained from models of stellar atmospheres (e.g., Hauschildt et al., 1999a,b; Castelli and Kurucz, 2003).

1.2.2. Constructing a Stellar Model

Under some simplifying assumptions, the system of differential equations given by Equations 1.2-1.10 can be solved analytically. However, these assumptions are not realistic for real stars. Instead, the equations of stellar structure must be solved numerically using a stellar modeling code. Thus, when creating any given stellar model, there are a number of choices that must be made by the modeler. These include:

- **Initial Conditions:** The first step is to decide what type of star will be modeled. At a minimum, this involves specifying the initial mass and composition of the star. Typically, the composition is described by the initial hydrogen (X), helium (Y), and metal (Z) mass fractions (or rather two out of the three as $X + Y + Z = 1$). Since only the metal abundance is given it is standard to assume that the relative abundances of individual metals scale according to the solar abundances (e.g., Grevesse and Sauval, 1998; Asplund et al., 2009; Magg et al., 2022).
- **Additional Physical Data:** For computational efficiency, some of the parameters in the stellar structure equations are computed outside of stellar modeling codes and stored in tables which can be interpolated during a stellar structure calculation. These data typically include: nuclear reaction rates, radiative opacity values, equation of state data, and diffusion coefficients. Usually, there are a variety of sources of data for any given parameters. For example, radiative opacity tables can be obtained from OPAL (Iglesias and Rogers, 1993, 1996), OP (Seaton, 2005), or OPLIB (Colgan et al., 2016). The situation is similar for low-temperature radiative opacity (Alexander and Ferguson, 1994; Ferguson et al., 2005; Marigo and Aringer, 2009), nuclear reaction rates (Angulo et al., 1999; Cyburt et al., 2010), and equation of state data (Irwin, 2004; Saumon et al., 1995; Rogers and Nayfonov, 2002; Jermyn et al., 2021).

- **Free Parameters:** Some physical processes that are important for stellar evolution are impossible to fully describe in only one dimension, i.e., convection, or do not yet have descriptions from first principles and must be described empirically, i.e., mass loss. These processes are often included in stellar modeling codes with simplified prescriptions involving a free parameter that must be somehow calibrated, either to observations or 3D simulations. For example, mixing length theory (for a review see, Joyce and Tayar, 2023), requires a choice of a mixing length parameter to describe convection.
- **Boundary conditions:** As discussed above, one must choose how to obtain the temperature and pressure at the surface of the star.
- **Numerical Parameters:** These describe the resolution of the desired stellar solution, both in terms of time (how large are the time steps between models) and space (how large are the mass steps used to discretize the equations). In addition, there are convergence parameters that describe how well a given numerical solution must satisfy equations 1.1, 1.2, 1.3, 1.5, and 1.10. These parameters must be chosen to balance the need for a well-resolved solution with computational efficiency. For asteroseismic modeling, proper choices of these parameters are particularly important (Li and Joyce, 2025).

An important assumption that is made in stellar evolution codes is that the derivatives with respect to time can be separated from the spatial derivatives. With this assumption, the process of calculating evolution over time is to alternate between solving the structure equations 1.1, 1.2, 1.3, 1.5 and then applying the time-dependent changes in equations 1.4 and 1.10. This process results in a series of static solutions at a given time. For clarity, I use ‘model’ to refer to the solution at a given time step and ‘track’ to refer to the evolutionary sequence. I refer to a collection of tracks with varying initial and free parameters as a ‘grid’.

1.3. Asteroseismology

I provide here an overview of the equations used to describe stellar oscillations, the different modes of oscillations, and the process of obtaining an asteroseismic best-fit model.

1.3.1. Oscillation Equations

The oscillations are treated as a time-dependent perturbation to the equilibrium structure (represented by the subscript such as ρ_0). In the following discussion, a bar over a variable, such as $\bar{\rho}$, indicates that it is time-dependent and a bold quantity is a 3D vector. The displacement due to this perturbation is $\underline{\xi}(r, \theta, \phi, t)$. In general, the perturbation is a function of the coordinates r, θ, ϕ , and time t . These perturbations also change the stellar structure variables P, ρ , and Φ (the gravitational potential). These perturbations can be described either as Eulerian perturbations (perturbations at a given point, represented with primed variables),

$$\bar{P} = P_0 + \bar{P}', \quad \bar{\rho} = \rho_0 + \bar{\rho}', \quad \bar{\Phi} = \Phi_0 + \bar{\Phi}' \quad (1.13)$$

or as Lagrangian perturbations (perturbation in the reference frame following the motion, denoted³ with D),

$$\bar{P} = P_0 + \overline{DP}, \quad \bar{\rho} = \rho_0 + \overline{D\rho}, \quad \bar{\Phi} = \Phi_0 + \overline{D\Phi}. \quad (1.14)$$

One type of perturbation can be converted to the other using

$$\overline{Dq} = \bar{q}' + \bar{\xi} \cdot \nabla q_0, \quad (1.15)$$

for any variable q . Unlike the equilibrium stellar structure described above, the oscillations are not spherically symmetric, and so their derivation requires the use of hydrodynamic equations in three dimensions.

1.3.1.1 Perturbed Equations of Stellar Structure

I start with the time-dependent equation of mass conservation,

$$\frac{\partial \bar{\rho}}{\partial t} + \nabla(\bar{\rho}\bar{\mathbf{v}}) = 0, \quad (1.16)$$

where $\bar{\mathbf{v}}$ is the velocity of the stellar material. For an equilibrium model $\bar{\mathbf{v}} = 0$. Substituting in the Eulerian perturbations from Equation 1.13,

$$\frac{\partial \rho_0 + \bar{\rho}'}{\partial t} + \nabla((\rho_0 + \bar{\rho}')\bar{\mathbf{v}}') = 0. \quad (1.17)$$

Here, $\bar{\mathbf{v}}' = d\bar{\xi}/dt$ is the velocity due to the perturbation. Keeping only the terms that are linear in the perturbation results in

$$\frac{\partial \bar{\rho}'}{\partial t} + \nabla(\rho_0\bar{\mathbf{v}}') = 0. \quad (1.18)$$

This can be integrated with respect to time to yield the perturbed equation of continuity

$$\boxed{\bar{\rho}' + \nabla(\rho_0\bar{\xi}) = 0.} \quad (1.19)$$

The next hydrodynamical equation is the equation of motion,

$$\bar{\rho} \frac{d\bar{\mathbf{v}}}{dt} = -\bar{\rho}\nabla\bar{\Phi} - \nabla\bar{P}, \quad (1.20)$$

where the gravitational potential Φ is given by Poisson's equation

$$\nabla^2\bar{\Phi} = 4\pi G\bar{\rho}. \quad (1.21)$$

³Here I adopt the notation used in Kippenhahn et al. (2013). It is also common to use δ to denote a Lagrangian perturbation. However, I reserve δ to denote the perturbations used to derive the mode kernels, detailed in the following section.

Following the same procedure as for the equation of continuity the perturbed form of Equation 1.20 is

$$\boxed{\rho_0 \frac{d^2 \bar{\xi}}{dt^2} = -\rho_0 \nabla \bar{\Phi}' - \bar{\rho}' \nabla \Phi_0 - \nabla \bar{P}'}, \quad (1.22)$$

where $\bar{\Phi}'$ can be calculated through the perturbed Poisson equation,

$$\boxed{\nabla^2 \bar{\Phi}' = 4\pi G \bar{\rho}'}. \quad (1.23)$$

An additional constraint can be added by assuming the oscillations to be adiabatic. The condition for adiabaticity of a Lagrangian perturbation is

$$\frac{D\bar{P}}{P_0} = \Gamma_1 \frac{D\bar{\rho}}{\rho_0}, \quad (1.24)$$

where $\Gamma_1 = \partial P / \partial \rho$ at constant specific entropy is the first adiabatic exponent. Converting this to the Eulerian perturbations gives

$$\boxed{\bar{P}' + \bar{\xi} \cdot \nabla P_0 = c_0^2 (\bar{\rho}' + \bar{\xi} \cdot \nabla \rho_0)}, \quad (1.25)$$

where $c^2 = \Gamma_1 / P \rho$ is the sound speed.

Equations 1.19, 1.22, 1.23, and 1.25 form a complete set of equations that can be solved given a choice of boundary conditions. However, further simplifications can be made using the expected form of the solutions. As we are looking for oscillatory solutions, it is natural to express the time-dependent displacement vector as

$$\bar{\xi}(r, \theta, \phi, t) = \xi(r, \theta, \phi) e^{-i\omega t}. \quad (1.26)$$

Here ξ is the time-independent displacement vector and ω is the angular frequency of the oscillation. In a spherically symmetric star, it is natural to express this in terms of the spherical harmonics

$$\xi = \xi(r) Y_{\ell m} \hat{r} + \eta(r) \left(\frac{\partial Y_{\ell m}}{\partial \theta} \hat{\theta} + \frac{1}{\sin \theta} \frac{\partial Y_{\ell m}}{\partial \phi} \hat{\phi} \right), \quad (1.27)$$

where ξ is the radial component of the displacement, η is the horizontal component, $Y_{\ell m}$ is the spherical harmonic function for a given spherical degree (ℓ) and azimuthal order (m), and $\hat{r}, \hat{\theta}, \hat{\phi}$ are the unit vectors. The only term that depends explicitly on time in our oscillation equations is

$$\frac{d^2 \bar{\xi}}{dt^2} = -\omega^2 \xi e^{-i\omega t}. \quad (1.28)$$

The perturbed quantities carry the same dependence on time as the displacement function, and thus the time dependence of all terms in Equations 1.19, 1.22, 1.23, and 1.25 cancels out. Going forward, I will consider only the time-independent perturbations. As a further simplification to the notation, I also drop the subscript on the equilibrium solution. Using Equation 1.27, Equation 1.19 reduces to

$$\boxed{\rho' = -\rho \left[\frac{2}{r} \xi + \frac{d\xi}{dr} - \frac{\ell(\ell+1)}{r} \eta \right] - \xi \frac{d\rho}{dr}}. \quad (1.29)$$

Equation 1.22 yields an equation for the radial component

$$\boxed{-\rho\omega^2\xi = -\rho\frac{d\Phi'}{dr} - \rho'\frac{d\Phi}{dr} - \frac{dP'}{dr}} \quad (1.30)$$

and an equation for the horizontal component

$$\boxed{-\rho\omega^2\eta = \frac{1}{r}\left(\frac{1}{\rho}P' - \Phi'\right)}. \quad (1.31)$$

Finally Equation 1.23 reduces to

$$\boxed{\frac{1}{r^2}\frac{d}{dr}\left(r^2\frac{d\Phi'}{dr}\right) - \frac{\ell(\ell+1)}{r^2}\Phi' = 4\pi G\rho'}. \quad (1.32)$$

Equations 1.29, 1.30, 1.31, and 1.32 form the system of equations that are solved numerically to obtain the eigenfunctions and eigenfrequencies of a stellar model.

1.3.2. Types of Modes

To discuss the general properties of different types of oscillation modes, it is useful to make several simplifying assumptions to the oscillation equations presented above. First, is what is known as the Cowling approximation, which neglects the perturbation to the gravitational potential ($\Phi' = 0$). The second is to assume that the eigenfunctions vary rapidly compared to the underlying equilibrium quantities. This approximation is typically valid only for modes with high radial order. With these two assumptions, the oscillation equations can be reduced to one second-order equation (Deubner and Gough, 1984)

$$\frac{d^2\xi}{dr^2} = \frac{\omega^2}{c^2}\left(1 - \frac{N^2}{\omega^2}\right)\left(\frac{S_\ell^2}{\omega^2} - 1\right)\xi. \quad (1.33)$$

Here I have introduced two characteristic frequencies: the Brunt-Väisälä, or buoyancy, frequency

$$N^2 = g\left(\frac{1}{\Gamma_1}\frac{d\ln P}{dr} - \frac{d\ln\rho}{dr}\right), \quad (1.34)$$

and the Lamb, or acoustic, frequency

$$S_\ell^2 = \frac{\ell(\ell+1)c^2}{r^2}. \quad (1.35)$$

For an oscillatory solution to exist, the right-hand side of Equation 1.33 must be positive. This is true under two conditions:

$$1) \quad |\omega| > N \quad \text{and} \quad |\omega| > S_\ell \quad (1.36)$$

or

$$2) \quad |\omega| < N \quad \text{and} \quad |\omega| < S_\ell. \quad (1.37)$$

In the first case, the mode is called a pressure mode or p-mode, and in the second case, the mode is a gravity mode or g-mode. As N and S_ℓ vary with the radial coordinate, whether conditions 1 or 2 are met varies throughout the star. The regions where modes can propagate, called oscillation cavities, differ between stars of different structures. These oscillation cavities can be visualized using a propagation diagram that shows the characteristic frequencies as a function of the radius, as shown for several stars in Figure 1.2.

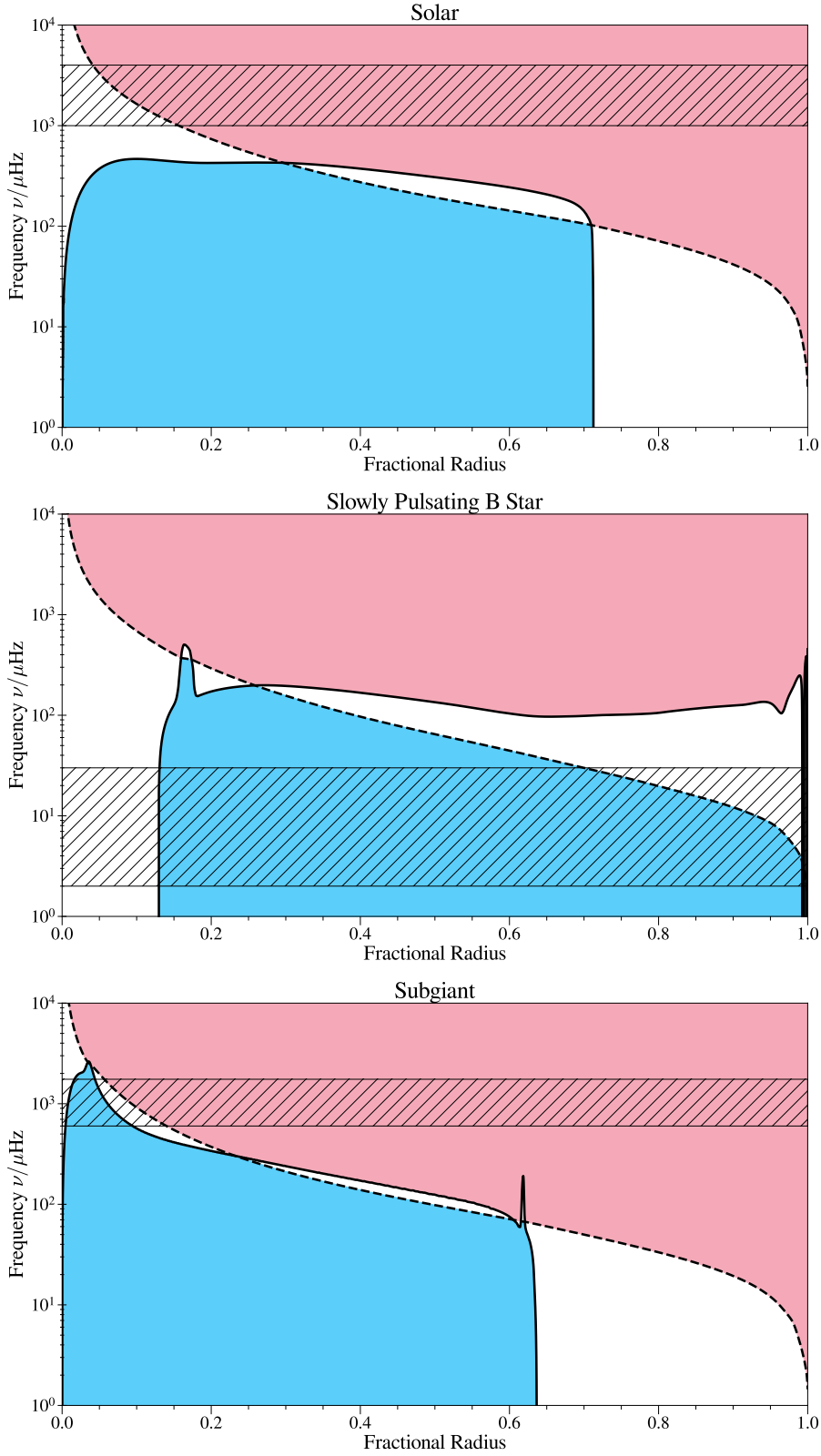


Figure 1.2: Propagation diagrams for modes of the Sun (top), a slowly pulsating B star (middle), and a subgiant star (bottom). The solid black lines show the buoyancy frequency defined in Equation 1.34. The dashed black lines show the acoustic frequency defined in Equation 1.35, for dipole ($\ell = 1$) modes. The p-mode cavities are shaded pink and the g-mode cavities blue. The hatched region indicates the range of observable frequencies for each type of star. The x -axis is fractional radius, r/R .

1.3.2.1 p-modes in Main-sequence Solar-like Oscillators

The excitation mechanism in solar-like oscillations excites modes around a characteristic frequency, ν_{\max} , which is related to the surface gravity of the star. Looking at the propagation diagram for a main-sequence solar-like oscillator, shown in Figure 1.2, reveals that the frequencies around ν_{\max} (indicated with hatching) satisfy the criteria in Equation 1.36 and thus are p-modes.

Further analysis of the asymptotic properties of p-modes shows that the modes of successive radial orders are evenly spaced in frequency. In the asymptotic limit, the mode frequencies are given by (Tassoul, 1980)

$$\nu_{n,\ell} = \frac{\omega_{n,\ell}}{2\pi} \simeq \left(n + \frac{\ell}{2} + \frac{1}{4} + \alpha_p \right) \Delta\nu. \quad (1.38)$$

Here ν is the linear frequency for a mode of a given radial order n and spherical degree ℓ , α_p is a function of frequency sensitive to the near-surface regions (Christensen-Dalsgaard and Berthomieu, 1991; Christensen-Dalsgaard and Perez Hernandez, 1992), and $\Delta\nu$ is the large frequency separation, which is related to the sound crossing time of the star

$$\Delta\nu = \left[2 \int_0^R \frac{dr}{c} \right]^{-1} \propto \sqrt{\frac{M}{R^3}}. \quad (1.39)$$

1.3.2.2 g-modes in Main-sequence Slowly Pulsating B Stars

Although not the focus of this work, I include in Figure 1.2 an example of the propagation diagram of a g-mode pulsator, in this case a slowly pulsating B (SPB) star. As seen from Figure 1.1, this class of pulsators is also on the main sequence. However, they have higher masses ($2-7M_{\odot}$) than main-sequence solar-like oscillators. In these stars, oscillations have periods ranging roughly from 0.8 to 3 days. From the propagation diagram, it is clear that these oscillations satisfy the criteria in Equation 1.37 and thus are g-modes. It is typical to talk about g-modes in terms of period rather than frequency as, in contrast to p-modes, g-modes are evenly spaced in frequency. From asymptotic analysis, the period of a mode Π is given by (Tassoul, 1980)

$$\Pi = \frac{\Pi_0}{L} (n + \alpha_{\ell,g}), \quad (1.40)$$

where $L = \sqrt{\ell(\ell+1)}$, $\alpha_{\ell,g}$ is a phase term that depends on the boundaries of the mode cavities, and Π_0 is the asymptotic period spacing

$$\Pi_0 = 2\pi^2 \left(\int_{r_1}^{r_2} N \frac{dr}{r} \right)^{-1}. \quad (1.41)$$

Here r_1, r_2 are the boundaries of the g-mode cavity. The period spacing for a given degree of modes is $\Delta\Pi_{\ell} = \Pi_0/L$.

1.3.2.3 Mixed Modes in Evolved Solar-like Oscillators

In certain cases, modes can be excited which oscillate in two cavities: one which is acoustic (satisfies criteria of Equation 1.36) and one which is buoyant⁴ (satisfies criteria of Equation 1.37). If the region between these two cavities is small enough, non-radial modes can

⁴It is also possible for stars to have multiple oscillation cavities of other configurations, for example after a stellar merger (Henneco et al., 2024).

propagate in both. These modes exhibit mixed character, behaving like p-modes in the outer layers and g-modes in the inner layers, and so are called mixed modes. Mixed modes were first predicted in massive stars (Osaki, 1975; Aizenman et al., 1977). More relevant for this work, however, is that mixed modes also occur in more evolved solar-like oscillators (e.g., Deheuvels and Michel, 2011). The propagation diagram shown in Figure 1.2 is for a subgiant star. As with the main-sequence solar-like oscillator, the relevant frequency range around ν_{\max} is indicated with hatching. This frequency range satisfies both criteria in Equations 1.36 and 1.37 in different parts of the star, and the zone between the two cavities is small enough that the non-radial modes exhibit a mixed nature.

These modes are neither equally spaced in frequency nor in period. However, they can be described as the coupling of a fictitious pure p-mode and a fictitious pure g-mode. The mode frequency is then given by (Shibahashi, 1979; Unno et al., 1989; Mosser et al., 2012)

$$\nu = \nu_{n_p, \ell} + \frac{\Delta\nu}{\pi} \arctan \left[q \tan \pi \left(\frac{L}{\nu \Delta \Pi_\ell} - \alpha_{\ell, g} \right) \right], \quad (1.42)$$

where $\nu_{n_p, \ell}$ is the frequency of the pure p-mode, and $\alpha_{\ell, g}$ is a phase term.

1.3.3. Asteroseismic modeling

In order to find an asteroseismic best-fit model, one requires frequencies of an observed star, a grid of stellar models, and some method of defining ‘best-fit’. Below, I discuss each of these steps in turn.

1.3.3.1 Observed Frequencies

Here, I provide a brief overview of the process of obtaining frequencies from observations. For more details, I refer the reader to Davies et al. (2016); Lund et al. (2017); Basu and Chaplin (2017). Asteroseismic observations require repeated observations over a long time, as the frequency resolution is given by the inverse of the total span of the data. It is also easier to extract genuine oscillation frequencies when the observations are uninterrupted. For this reason, long-term space missions like *Kepler* (Borucki et al., 2010; Koch et al., 2010) are the preferred sources of asteroseismic data. Although for a limited number of stars, data are also available from the ground-based SONG network (Grundahl et al., 2007). As we are looking for the oscillation frequencies, it is best to work in the frequency domain. Thus, after the light curve has been corrected for instrumental effects the first step is a Fourier transform. There are other sources of variability beyond the oscillations. These include additional instrumental effects and intrinsic variability due to granulation, rotation, and stellar spots. Removing these effects allows the oscillation signal to be isolated. In a power density spectrum, the signal of solar-like oscillations is a Gaussian-shaped excess of power. The central frequency of this power excess is the ν_{\max} value discussed above. An example a power density spectrum for the solar analog 16 Cyg A is shown in Figure 1.3.

Given high enough resolution, it is possible to identify not only the presence of solar-like oscillations but also to identify the frequencies of individual modes through a process known as peak bagging. The repeating pattern of p-modes can be used to identify the spherical degree of the fitted modes. When fully resolved in frequency space, solar-like oscillation modes are expected to exhibit a Lorentzian profile (Batchelor, 1953; Kumar et al., 1988). This profile can be fit, for example using Markov Chain Monte Carlo methods, to obtain the oscillation mode frequencies and their uncertainties.

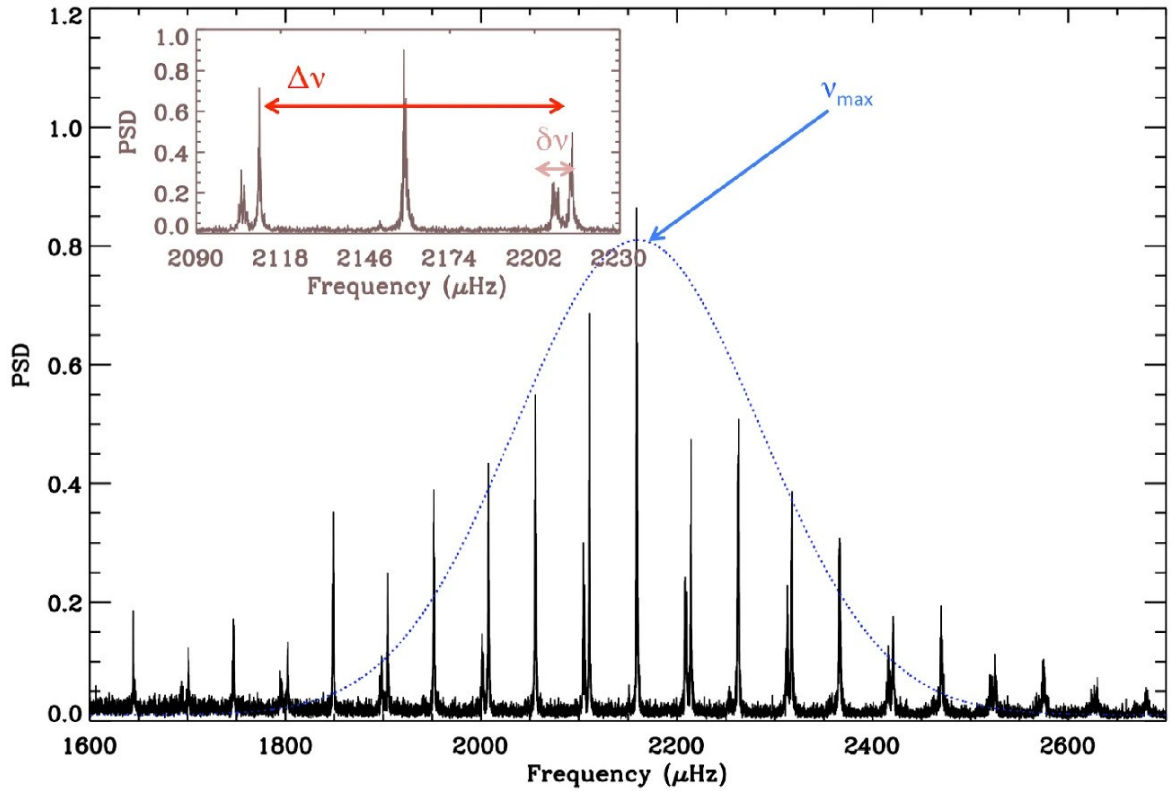


Figure 1.3: Power density spectrum of the solar analog 16 Cyg A. The Gaussian envelope of power is indicated with a blue dashed line. The central frequency of this envelope is the frequency of maximum power ν_{\max} . The inset zooms into to show the large frequency separation $\Delta\nu$, and the small frequency separation $\delta\nu_{02} = \nu_{n,\ell} - \nu_{n-1,\ell+2}$. While $\Delta\nu$ is related to the mean density of the star, $\delta\nu_{02}$ is related to the sound speed gradient in the core of the star. Figure taken from García and Ballot (2019) under the Creative Commons Attribution 4.0 License.

1.3.3.2 Model Frequencies

The oscillation equations can be solved numerically for a given stellar model using an oscillation code. Equations 1.29 through 1.32 form a fourth-order system of equations and thus require four boundary conditions. Two can be provided by enforcing regularity at $r = 0$:

$$\rho'(r = 0) = 0 \quad \text{and} \quad P'(r = 0) = 0. \quad (1.43)$$

As with the equations of stellar structure, the outer boundary conditions can be more complex. There are several different formulations used (e.g., Dziembowski, 1971; Unno et al., 1989). Most relevant for this work are the boundary conditions necessary to satisfy the variational principle (Chandrasekhar, 1964) used to derive the mode kernel, discussed in the following section,

$$\rho(r = R) = 0 \quad \text{and} \quad P'(r = R) = 0. \quad (1.44)$$

As the oscillation equations are solved numerically, there are numerical parameters that must be chosen. The most important of these controls set the spatial resolution of the mesh and the time resolution of the frequency grid used to calculate the oscillation.

The goal of asteroseismic modeling is to obtain a stellar model that matches the observed mode frequencies and surface properties (such as luminosity, effective temperature, and surface composition) as closely as possible. Directly comparing modeled frequencies to observed frequencies, however, is complicated by our poor modeling of the outer layers of a star.

1.3.3.3 Surface Term

The outer layers of stars remain difficult to model properly. For asteroseismic analysis, we also run into difficulties due to the assumption of adiabatic oscillations and the lack of a clear description of the interaction between oscillations and convective motions. All of these factors result in a frequency-dependent shift between observed frequencies and the frequencies of stellar models. It is common to lump these difficulties together into a so-called ‘surface term’.

In asteroseismic modeling, there are two main approaches to dealing with the surface term. The first is to use an empirical relation to correct the mode frequencies. The most common of these was proposed by Ball and Gizon (2014). This semi-empirical approach begins by noting the expected form of several possible perturbations to the near-surface layers (Gough, 1990; Goldreich et al., 1991). These perturbations take the form ν^{-1}/E and ν^3/E where E is the normalized mode inertia given by

$$E = \frac{4\pi \int_0^R [\xi^2 + \ell(\ell + 1)\eta^2] \rho r^2 dr}{M [\xi^2(R) + \ell(\ell + 1)\eta^2(R)]}. \quad (1.45)$$

The expected shift due to these perturbations $\delta\nu_S$ is

$$\delta\nu_S = \frac{1}{E} \left(a_{-1} \left(\frac{\nu}{\nu_{ac}} \right)^{-1} + a_3 \left(\frac{\nu}{\nu_{ac}} \right)^3 \right). \quad (1.46)$$

Here ν_{ac} is the acoustic cutoff frequency, which can be found by a scaling relation from the solar value, $\nu_{ac,\odot} = 5000 \mu\text{Hz}$,

$$\nu_{ac} = \frac{M}{M_\odot} \left(\frac{R}{R_\odot} \right)^{-2} \left(\frac{T_{\text{eff}}}{T_{\text{eff},\odot}} \right)^{-1/2} \cdot \nu_{ac,\odot}. \quad (1.47)$$

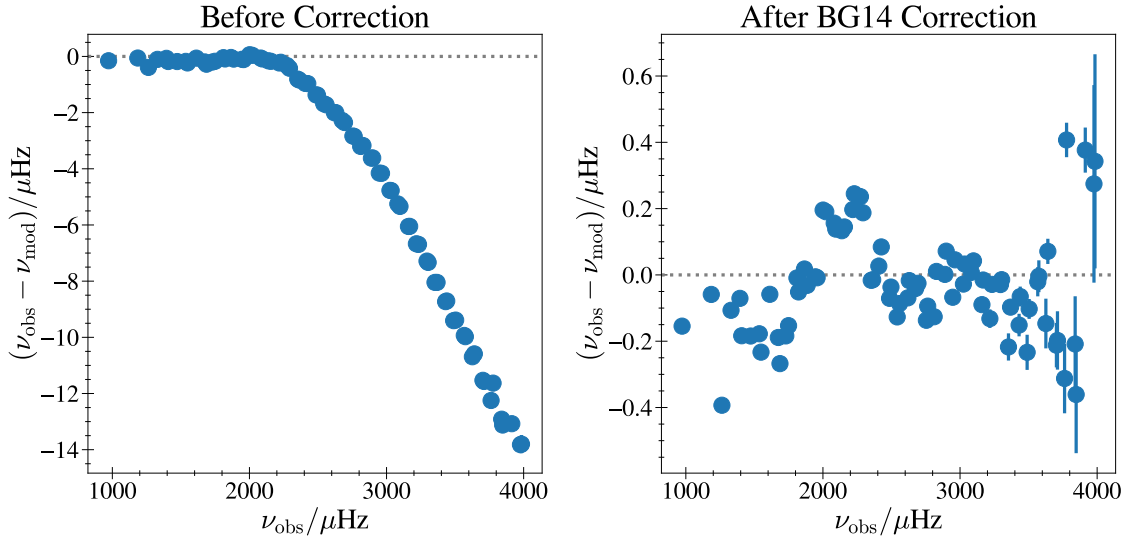


Figure 1.4: Frequency differences between the low-degree oscillation modes of the Sun (Broomhall et al., 2009) and a standard solar model (Model S, Christensen-Dalsgaard et al., 1996). The left (right) panel shows the frequency differences before (after) the surface term correction has been applied. Note that the y -axis scale differs significantly between the two panels. In both panels, the 1σ uncertainty of the observed frequencies is shown, although in most cases it is smaller than the size of the points.

The coefficients a_{-1}, a_3 are found through a least-squares fit to the frequency differences between observation and model. With these coefficients, a correction can be applied to the model frequencies $\nu_{\text{mod, cor}} = \nu_{\text{mod}} + \delta\nu_S$. In Figure 1.4, I show the frequency differences between the Sun (Broomhall et al., 2009) and a standard solar model (Model S, Christensen-Dalsgaard et al., 1996) before and after applying the surface term correction.

The other approach to dealing with the surface term is to construct combinations of frequencies such that the combinations are less sensitive to the surface (Roxburgh and Vorontsov, 2003). These frequency separation ratios are defined as

$$r_{01}(n) = \frac{1}{8} \frac{\nu_{n-1,0} - 4\nu_{n-1,1} + 6\nu_{n,0} - 4\nu_{n,1} + \nu_{n+1,0}}{\nu_{n,1} - \nu_{n-1,1}}, \quad r_{02}(n) = \frac{\nu_{n,0} - \nu_{n-1,2}}{\nu_{n,1} - \nu_{n-1,1}}. \quad (1.48)$$

Taking the frequency separation ratios removes information about the mean density of the star and so often ratios are used in combination with a value of $\Delta\nu$, which must be corrected for surface effects.

For more evolved stars, the surface term problem becomes more complicated due to the emergence of mixed modes whose sensitivity to surface effects is different (Kjeldsen et al., 2008). Recent work has suggested a way forward by decomposing the mixed mode into the underlying pure acoustic and gravity modes (Ong and Basu, 2020). The surface term correction can then be applied only to the pure acoustic mode. The corrected acoustic mode can then be recoupled with the pure gravity mode into a surface term corrected mixed mode (Ong et al., 2021b,a; Lindsay et al., 2024).

1.3.4. Best-fit Asteroseismic Models

Without asteroseismic observations, stellar modeling is limited only to surface properties of a star such as luminosity, effective temperature, and surface composition. With these parameters alone, there are many degeneracies that make it difficult to infer precise stellar parameters. By providing direct constraints on the interiors of stars, asteroseismology provides a wealth of information that can be used to model stars and better constrain their global parameters and internal structures. For the solar-like oscillators which are the focus of this work, the additional observations provided by asteroseismology are the oscillation mode frequencies⁵.

There are many different ways to obtain a best-fit model. A representative sample is provided by the various pipelines used in Silva Aguirre et al. (2015) and Silva Aguirre et al. (2017). These pipelines differ in the asteroseismic observations fit (frequencies and/or frequency separation ratios), and the optimization procedure used. All pipelines begin by constructing an initial grid of models with various initial conditions. The best-fit model within each grid can be found using Bayesian χ^2 minimization, Monte Carlo, or Markov Chain Monte Carlo methods depending on the pipeline. In some cases, the initial grid serves only to provide the initial guess of an optimization procedure, such as downhill simplex (Nelder and Mead, 1965) or Levenberg-Marquardt (Levenberg, 1944).

The best-fit asteroseismic models are used to infer the properties of the star such as its mass, radius, or age (e.g., Silva Aguirre et al., 2015; Bellinger et al., 2016; Silva Aguirre et al., 2017). Of course, these inferences are only as accurate as the stellar model used. Thus, another important use of asteroseismic modeling is to test the quality of stellar modeling physics. This can be done in a variety of ways. A common method is to construct several grids of models with differing physics and obtain best-fit models for a large number of stars from each grid. Then, some inferences can be made by looking for the choices in modeling that returned the better fit to observations across the entire sample (e.g, B  trisey et al., 2023; Wang and Zhang, 2023).

However, even in the best case, differences remain between models and observations. While these differences are small (the frequencies of main-sequence models typically match observations within 0.5% after correcting for surface effects), the high precision of asteroseismic observations means that these differences are still statistically significant. This leads to another approach to test the quality of stellar models: that of structure inversions.

1.4. Structure Inversions

The goal of a structure inversion is to use the inherent sensitivity of the oscillation modes to infer information about structure differences between a star and its model (typically a best-fit model, as discussed above). These inferred differences are then used to assess how well the internal structure of a star is reproduced by a given stellar model, as well as to explore potential improvements to stellar modeling. The roots of this approach lie in the field of geology, which uses oscillations excited by earthquakes to infer the interior structure of the Earth (Backus and Gilbert, 1968, 1970). The techniques were then adapted by helioseismologists to study the internal structure of the Sun (e.g., Gough and Thompson, 1991; Christensen-Dalsgaard, 2002; Basu, 2016).

⁵Other properties of the oscillation modes, such as the lifetime, can be obtained, however without a complete theoretical description of the excitation mechanism these are difficult to compare to models.

In anticipation of high-quality asteroseismic data, helioseismologists began testing what changes would be necessary to apply structure inversions to stars other than the Sun (Gough and Kosovichev, 1993; Basu et al., 2002; Basu, 2003). Much of this work focused on adapting existing helioseismic techniques to the higher uncertainties and reduced number of modes that can be observed in other stars. Initial observations of solar-like oscillations in other stars from ground-based campaigns (Brown et al., 1991; Kjeldsen et al., 1995; Bedding et al., 2001; Bedding and Kjeldsen, 2007) and early space-based missions such as CoRoT (Auvergne et al., 2009; Baglin et al., 2009) did not provide enough identified modes to perform structure inversions. The first asteroseismic structure inversions were performed on the solar analogs 16 Cyg A and B (Bellinger et al., 2017), using data from *Kepler*.

In this work, I focus specifically on inversions to infer stellar structure at specific target radii (e.g., Bellinger et al., 2017, 2019a; Kosovichev and Kitiashvili, 2020; Bellinger et al., 2021; Buldgen et al., 2022b; Buchele et al., 2024b,a). However, similar inverse techniques are used to infer a broader range of internal properties of an observed star. These internal properties can include global indicators (e.g., Reese et al., 2012; Buldgen et al., 2015b,a, 2018), rotational profiles (e.g., Kurtz et al., 2014; Deheuvels et al., 2014; Benomar et al., 2015; Triana et al., 2017; Ahlborn et al., 2020, 2022, 2025), and more recently, the strength of internal magnetic fields (Li et al., 2022, 2023).

1.4.1. Mode Kernels

Structure inversions exploit the inherent sensitivity of oscillation mode frequencies to the underlying structure of the star. This sensitivity can be expressed in functions calculated from the structure variables of a stellar model called mode kernels. Mathematically, this is expressed as (Dziembowski et al., 1990)

$$\frac{\delta v_i}{v_i} = \int K_i^{(f_1, f_2)} \frac{\delta f_1}{f_1} dr + \int K_i^{(f_2, f_1)} \frac{\delta f_2}{f_2} dr, \quad (1.49)$$

where the subscript i indicates a mode with a specific combination of radial order and spherical degree, v_i is the corresponding mode frequency, K_i are the mode kernels, and f_1, f_2 indicate the stellar structure variables being considered. We define the relative difference of a given quantity y , which can represent either a mode frequency or structure variable, as $\delta y/y \equiv (y_{\text{obs}} - y_{\text{mod}})/y_{\text{mod}}$. Where the subscripts ‘obs’ and ‘mod’ refer to quantities of the observed star and the reference model, respectively.

The mode kernels, $K_i^{(f_1, f_2)}, K_i^{(f_2, f_1)}$ are derived through a linear perturbation of the variational formulation of the adiabatic eigenvalue problem (e.g., Ledoux and Walraven, 1958). Derivations of these kernels typically begin by deriving K_i in terms of the squared sound speed ($f_1 = c^2$) and density ($f_2 = \rho$) (e.g., Gough and Thompson, 1991; Kosovichev, 1999). Using the c^2, ρ kernels as a starting point, kernels of other variable pairs may be derived including: density and the first adiabatic exponent (e.g., Gough and Thompson, 1991; Gough and Kosovichev, 1993), squared isothermal sound speed ($u = c^2/\Gamma_1$) and helium mass fraction (Y) (e.g., Basu and Christensen-Dalsgaard, 1997; Kosovichev, 1999; Buldgen et al., 2015a, 2017), and the convective stability parameter (A) and Γ_1 (e.g., Elliott, 1996; Kosovichev, 1999; Buldgen et al., 2017). In Appendix A, I provide a detailed derivation of kernels for several different variable pairs. In Figure 1.5, I show the c^2, ρ and u, Y kernels of several modes of a solar model.

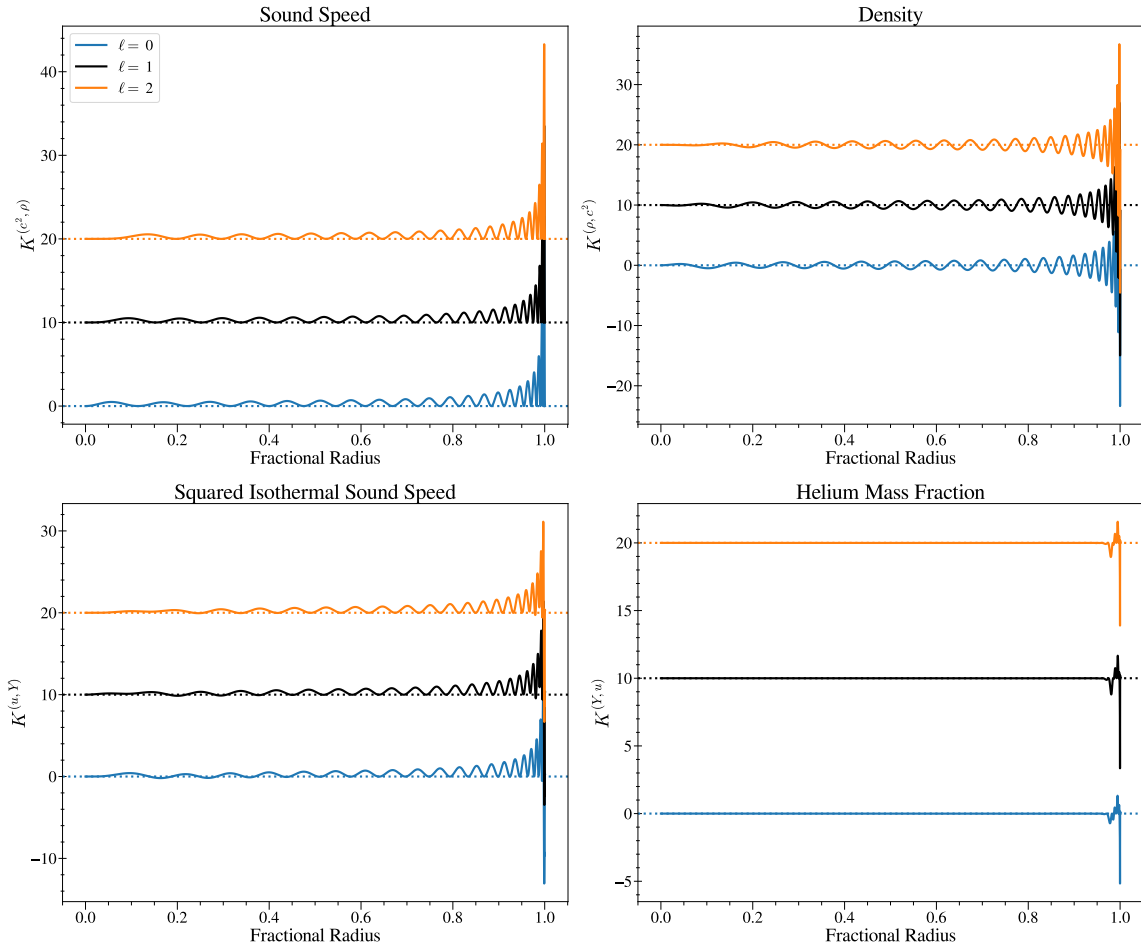


Figure 1.5: Mode kernels of a solar model (Model S, Christensen-Dalsgaard et al., 1996) for two variable pairs. The first row plots the c^2, ρ pair, and the second row the u, Y pair. Each kernel is offset for visibility and the color of the line corresponds to the spherical degree of the mode, as indicated.

In asteroseismic inversions, the most common variable pair used is u, Y . This is because the oscillations are insensitive to Y outside the helium ionization zone. This low sensitivity to Y makes it easier to localize sensitivity to changes in u . In the solar case, the use of u, Y kernels is disfavored as it requires the assumption of an equation of state. This assumption can introduce significant errors when compared to the extreme precision of the solar data (Basu and Christensen-Dalsgaard, 1997), however, it is expected that these errors will be smaller than the observational uncertainties of other stars (Basu, 2003).

There is another complication that arises when studying stars other than the Sun: the lack of precise values of the stellar age, mass, and radius. As the oscillation frequencies scale with the mean density of the star, a mismatch in mean density can introduce error into inversion results (Basu, 2003). To avoid this, it is common to perform asteroseismic inversions with respect to dimensionless variables, for example, $\hat{u} = uR/M$. This requires the use of dimensionless frequencies

$$\hat{\nu} = \sqrt{\frac{R^3}{GM}} \nu. \quad (1.50)$$

This scaling also means that the structure differences are inferred at constant fractional radii $x = r/R$ rather than at constant physical radius. For an observed star, where M and R are uncertain, the dimensionless frequency differences, $\delta\hat{\nu}/\hat{\nu}$, cannot be determined exactly, as the model is not guaranteed to have exactly the same value of $\sqrt{R^3/GM}$ as the star.

There are several different approaches to resolve this potential source of error, at various steps in the inversion process. Errors due to mean density differences can be handled by including an additional term in the inversion cost function (discussed below), as was done by Kosovichev and Kitiashvili (2020). Alternatively, this issue can be addressed at the stage of determining a best-fit model as was the case in Buldgen et al. (2022b), who used mean density inversions to ensure that the mean density of the model matched the star close enough to assume that $\delta\nu/\nu \approx \delta\hat{\nu}/\hat{\nu}$. There are also two existing approaches to approximate the dimensionless frequency differences, which can then be used directly in the inversion procedure. Roxburgh et al. (1998); Basu (2003) proposed that $\delta\hat{\nu}/\hat{\nu}$ can be calculated by subtracting a weighted mean of the radial mode frequency differences. This approach was used by Bellinger et al. (2021). In Chapter 2, I propose another approach that utilizes the dependence of the $\Delta\nu$ on the mean density to scale the frequency differences. This approach is also used in Chapter 3.

In addition to potential mean differences, the inversion procedure also needs to account for differences due to the surface effects discussed in Section 1.3.3.3. Here again, there are several possible approaches. The most common is to include an additional F_{surf} term in Equation 1.49. This term is then accounted for during the inversion procedure, as described below. The other option is to correct the frequency differences used outside of the inversion procedure, for example when calculating $\delta\hat{\nu}/\hat{\nu}$. I take the last approach in this thesis.

1.4.2. OLA Inversions

Equation 1.49 describes the sensitivity of a single mode, however, it is insufficient to infer anything about the differences in structure because each oscillation mode is sensitive to many points within the star. Therefore, to infer localized differences we must take a linear combination of modes constructed such that the resulting "averaging" kernel has sensitivity only around a chosen target radius, x_0 . This is the method of optimally localized averages

(OLA) (Backus and Gilbert, 1968, 1970). Taking a linear combination of different modes turns Equation 1.49 into:

$$\sum_{i=0}^N c_i \frac{\delta \hat{v}_i}{\hat{v}_i} = \int \mathcal{K}(x_0, x) \frac{\delta \hat{u}}{\hat{u}} dx + \int C(x_0, x) \delta Y dx. \quad (1.51)$$

In this equation, N is the total number of observed modes, c_i are the coefficients of the linear combination for a given target radius, called inversion coefficients, $\mathcal{K}(x_0, x) = \sum_{i=0}^N c_i K_i^{(\hat{u}, Y)}$ is the averaging kernel for a given target radius, $C(x_0, x) = \sum_{i=0}^N c_i K_i^{(Y, \hat{u})}$ is the cross-term kernel. $\mathcal{K}(x_0, x)$ is called an averaging kernel because if it is normalized to 1 and $C(x_0, x)$ is small, then Equation 1.51 becomes

$$\sum_{i=0}^N c_i \frac{\delta \hat{v}_i}{\hat{v}_i} = \int \mathcal{K}(x_0, x) \frac{\delta \hat{u}}{\hat{u}} dx \approx \left\langle \frac{\delta \hat{u}}{\hat{u}} \right\rangle_{x_0}, \quad (1.52)$$

and the linear combination of frequency differences can be interpreted as the average of the structure differences at the target radius, where \mathcal{K}_{x_0} is the weighting function.

There are two common approaches to determine the coefficients which construct the localized averaging kernel: multiplicative optimally localized averages (MOLA) (Backus and Gilbert, 1968, 1970) and subtractive optimally localized averages (SOLA) (Pijpers and Thompson, 1992, 1994). Regardless of whether MOLA or SOLA is used, the problem is cast as a matrix equation

$$\mathbf{A} \mathbf{c} = \mathbf{b} \quad (1.53)$$

where the vector \mathbf{c} contains the desired inversion coefficients c_i . The elements of the matrix \mathbf{A} and the vector \mathbf{b} depend on the OLA method chosen as described below.

1.4.2.1 MOLA

MOLA constructs an averaging kernel by using a penalty function, typically $J(x_0, x) = (x - x_0)^2$, to suppress amplitude away from the target radius. This is done by minimizing

$$\int \left(\sum_{i=0}^N c_i K_i^{(\hat{u}, Y)} \right)^2 J(x_0, x) dx + \beta \int \left(\sum_{i=0}^N c_i K_i^{(Y, \hat{u})} \right)^2 dx + \mu \sum_{i,j} c_i c_j E_{ij}, \quad (1.54)$$

where β is the cross-term suppression parameter, μ is the error suppression parameter, and E_{ij} are the elements of the error covariance matrix. The two trade-off parameters β and μ are chosen to balance the localization of the averaging kernel, amplitude of the cross-term kernel, and amplification of the uncertainties.

In addition to minimizing Equation 1.54, the inversion must also ensure that $\int \mathcal{K}(x_0, x) dx = 1$ and potentially correct the frequencies for surface terms, such as by using the prescription of Ball and Gizon (2014). The elements of \mathbf{A} and \mathbf{b} are given by⁶

⁶If the surface term correction has been applied outside of the inversion procedure then the matrix \mathbf{A} contains only the $i, j, \leq N + 1$ terms and the \mathbf{b} vector contains only the $i \leq N + 1$ elements.

$$A_{ij} = \begin{cases} \int (x - x_0)^2 K_i^{(\hat{u}, Y)} K_j^{(\hat{u}, Y)} dx + \beta \int K_i^{(Y, \hat{u})} K_j^{(Y, \hat{u})} dx + \mu E_{ij}, & (i, j \leq N) \\ \int K_i^{(\hat{u}, Y)} dx, & (i \leq N, j = N + 1) \\ \int K_j^{(\hat{u}, Y)} dx, & (i = N + 1, j \leq N) \\ \left(\frac{v_i}{v_{ac}}\right)^{-2} \frac{1}{E_i}, & (i = N + 2, j \leq N) \\ \left(\frac{v_j}{v_{ac}}\right)^{-2} \frac{1}{E_j}, & (i \leq N, j = N + 2) \\ \left(\frac{v_j}{v_{ac}}\right)^2 \frac{1}{E_j}, & (i = N + 3, j \leq N) \\ 0, & (i \leq N, j = N + 3) \\ 0, & \text{otherwise,} \end{cases} \quad (1.55)$$

$$b_i = \begin{cases} 1, & (i = N + 1) \\ 0, & \text{otherwise.} \end{cases} \quad (1.56)$$

1.4.2.2 SOLA

The other common way of constructing an averaging kernel, SOLA, begins by defining a target kernel \mathcal{T} and constructs an averaging kernel that resembles the target kernel. In this case, the function to be minimized is

$$\int \left(\sum_{i=0}^N c_i K_i^{(\hat{u}, Y)} - \mathcal{T} \right)^2 dx + \beta \int \left(\sum_{i=0}^N c_i K_i^{(Y, \hat{u})} \right)^2 dx + \mu \sum_{i,j} c_i c_j E_{ij}. \quad (1.57)$$

A common form of the target kernel is a modified Gaussian, such as

$$\mathcal{T}(x_0, r) = A \exp \left(- \left[\frac{x - x_0}{D(x_0, \Delta)} + \frac{D(x_0, \Delta)}{2x_0} \right]^2 \right), \quad (1.58)$$

where A is a normalization factor chosen to ensure $\int \mathcal{T} dx = 1$, and the width of the target kernel is set by the function

$$D(x_0, \Delta) = \Delta \frac{c(x_0)}{c(x_f)}. \quad (1.59)$$

In this function Δ is an additional free parameter, which as with β and μ must be chosen to balance the trade-off between resolution and precision, c without any subscript is the sound speed, and x_f is an arbitrary reference point. The function D is used to change the width of the target kernel according to variations in c since it is the sound speed that ultimately sets the resolution. Using Equation 1.57, and including the same additional normalization and surface terms as for MOLA, the elements of \mathbf{A} and \mathbf{b} are given by⁷

⁷As with MOLA, if the surface term correction has been applied outside of the inversion procedure then the matrix \mathbf{A} contains only the $i, j, \leq N + 1$ terms and the \mathbf{b} vector contains only the $i \leq N + 1$ elements.

$$A_{ij} = \begin{cases} \int K_i^{(\hat{u},Y)} K_j^{(\hat{u},Y)} dx + \beta K_i^{(Y,\hat{u})} K_j^{(Y,\hat{u})} dx + \mu E_{ij}, & (i, j \leq N) \\ \int K_i^{(\hat{u},Y)} dx, & (i \leq N, j = N + 1) \\ \int K_j^{(\hat{u},Y)} dx, & (i = N + 1, j \leq N) \\ \int K_j^{(\hat{u},Y)} dx, & (i = N + 1, j \leq N) \\ \left(\frac{v_i}{v_{ac}}\right)^{-2} \frac{1}{E_i}, & (i = N + 2, j \leq N) \\ \left(\frac{v_j}{v_{ac}}\right)^{-2} \frac{1}{E_j}, & (i \leq N, j = N + 2) \\ \left(\frac{v_j}{v_{ac}}\right)^2 \frac{1}{E_j}, & (i = N + 3, j \leq N) \\ \left(\frac{v_i}{v_{ac}}\right)^2 \frac{1}{E_i}, & (i \leq N, j = N + 3) \\ 0, & \text{otherwise,} \end{cases} \quad (1.60)$$

$$b_i = \begin{cases} \int K_i^{(\hat{u},Y)} \mathcal{T} dr & i \leq N \\ 1, & (i = N + 1) \\ 0, & \text{otherwise.} \end{cases} \quad (1.61)$$

1.4.2.3 Inversion Procedure

In both SOLA and MOLA, the free parameters must be chosen to balance forming a well-localized averaging kernel, suppressing the amplitude of the cross-term kernel, and moderating the uncertainty of the final result. I show several possible parameter choices in Figure 1.6. Once the elements of \mathbf{A} and \mathbf{b} have been calculated using the chosen method, the inversion coefficients are given by

$$\mathbf{A}^{-1} \mathbf{b} = \mathbf{c}, \quad (1.62)$$

where \mathbf{A}^{-1} is the inverse of the matrix \mathbf{A} . In summary, the steps to performing a structure inversion include: finding a suitable reference model (typically a best-fit model), using this model to calculate a set of mode kernels, combining these mode kernels into a suitable averaging kernel using either SOLA or MOLA, and using the inversion coefficients to obtain the final inversion result.

Typically, the uncertainty of each observed frequency is assumed to be independent. In this case, the uncertainty of the final inversion result is given by

$$\sigma_{\text{inv}}^2 = \sum_{i=0}^N c_i^2 \sigma_i^2, \quad (1.63)$$

where σ_i is the relative uncertainty of the i th mode. When the frequency differences used are corrected for mean density differences or surface effects outside of the inversion, this can introduce error correlation, as these corrections depend on all the frequencies. In this case, more care is required when calculating the uncertainty of an inversion result as is discussed in Section 2.3.3.

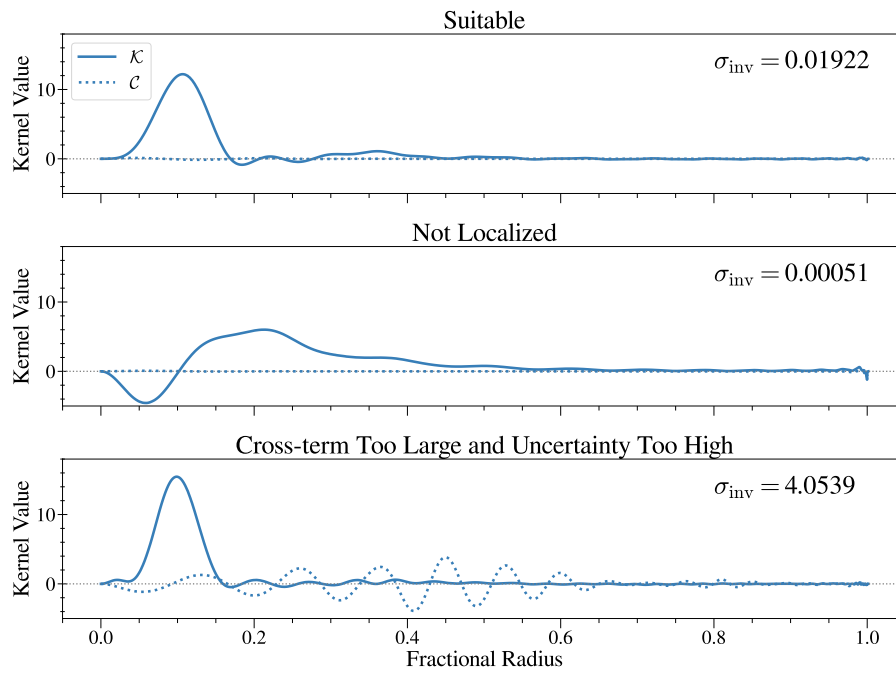


Figure 1.6: Averaging kernels and cross-term kernels constructed using MOLA, with varying values of μ and $\beta = 0$. These kernels have been constructed using the mode set and best-fit model of 16 Cyg A from Chapter 2. The top row shows a ‘suitable’ averaging kernel that is well localized, keeps the amplitude of the cross-term kernel low, and mitigates the uncertainty of the final results σ_{inv} . The bottom two rows show averaging kernels that do not meet these criteria, either due to poor localization (middle) or high amplitude of cross-term kernel and large uncertainties (bottom).

1.5. Summary of Thesis

Before the work presented in this thesis, structure inversions had been used to study six stars other than the Sun. The first targets were the solar analogs 16 Cyg A and B, which were first studied by Bellinger et al. (2017) and then later examined by Buldgen et al. (2022b). Both works find that the structures of their respective reference models agree with the structure of the observed stars in the regions where inversions are sensitive. The case is quite different for the star studied in Bellinger et al. (2019a). This star is slightly more massive and so is expected to exhibit a small convective core. The structure inversions performed in Bellinger et al. (2019a) reveal significant structure differences across the entire region probed with inversions.

Two different works have used structure inversions to study stars exhibiting mixed modes. Kosovichev and Kitiashvili (2020) present results for two stars in which they identify mixed modes, although this identification has been challenged (Buchele et al., 2024a). In both stars studied by Kosovichev and Kitiashvili (2020), the inversions reveal significant differences between their models and the stars. Bellinger et al. (2021) perform inversions to investigate the core, hydrogen-burning shell, and envelope of the subgiant HR 7322. They find good agreement between their reference models and the star at all three target radii. There is some suggestion that the core temperature may be too low in the models, however, this disagreement is resolved when an outlier mode is removed from the analysis.

These inversion results show that our ability to accurately model the interior structure of solar-like oscillators is mixed. Drawing broader conclusions is hindered by the small sample size and the challenge of comparing inversion results across different works. This is because inversions infer structure differences relative to a reference model and as weighted by an averaging kernel. Thus, to draw broader conclusions about the overall quality of stellar models, it is important to increase the sample of stars probed with structure inversions. To facilitate easier comparisons, the modeling and inversion procedures should be kept as consistent as possible across different stellar targets. In expanding the sample of stars that can be studied with inversions, it becomes necessary to expand the type of star that can be studied. However, doing so brings into question the validity of the underlying assumptions of a structure inversion, particularly in the case of mixed modes.

With this context in mind, the goals of this thesis are as follows:

1. Broaden the sample of main-sequence stars studied with inversions using a consistent modeling and inversion procedure.
2. Use the inversion results to look for trends that may suggest how these models can be improved.
3. Test the reliability of structure inversions beyond the Main Sequence.

The first two goals are addressed in Chapters 2 and 3. Chapter 2 details my approach to structure inversions and uses it to study the structure of 12 main-sequence solar-like oscillators with radiative cores. Chapter 3 extends this analysis to an additional 43 main-sequence stars with convective cores. The third goal is addressed in Chapter 4 which examines the validity of the key assumptions of structure inversions using models of main-sequence and subgiant stars. Chapter 5 summarizes the previous chapters and suggests several next steps to improve our understanding of the internal structure of solar-like oscillators.

Asteroseismic Inversions for Internal Sound Speed Profiles of Main-sequence Stars with Radiative Cores

AUTHORS Lynn Buchele, Earl P. Bellinger, Saskia Hekker, Sarbani Basu, Warrick Ball, and Jørgen Christensen-Dalsgaard

CHAPTER INFO This chapter is a reproduction of Buchele et al. (2024b), *ApJ*, vol. 961, 198B. It details my inversion procedure and applies this procedure to 12 main-sequence stars with radiative cores observed by *Kepler*. As the main author of this work, I computed the model grids, found the best-fit models, and performed the inversions. Throughout this process, I was advised and mentored by Earl P. Bellinger, Saskia Hekker, Sarbani Basu, and Jørgen Christensen-Dalsgaard. Warrick Ball contributed by writing code to calculate the equation of state derivatives necessary to calculate the u, Y kernels within MESA. The text was written by myself with guidance from my supervisor Saskia Hekker and comments from all co-authors.

ABSTRACT The theoretical oscillation frequencies of even the best asteroseismic models of solar-like oscillators show significant differences from observed oscillation frequencies. Structure inversions seek to use these frequency differences to infer the underlying differences in stellar structure. While used extensively to study the Sun, structure inversion results for other stars have so far been limited. Applying sound speed inversions to more stars allows us to probe stellar theory over a larger range of conditions, as well as look for overall patterns that may hint at deficits in our current understanding. To that end, we present structure inversion results for 12 main-sequence solar-type stars with masses between $1 M_{\odot}$ and $1.15 M_{\odot}$. Our inversions are able to infer differences in the isothermal sound speed in the innermost 30% by radius of our target stars. In half of our target stars, the structure of our best-fit model fully agrees with the observations. In the remainder, the inversions reveal significant differences between the sound speed profile of the star and that of the model. We find five stars where the sound speed in the core of our stellar models is too low and one star showing the opposite behavior. For the two stars in which our inversions reveal the most significant differences, we examine whether changing the microphysics of our models improves them and find that changes to nuclear reaction rates or core opacities can reduce, but do not fully resolve, the differences.

2.1. Introduction

The combination of high-precision photometric time series data from *Kepler* (Borucki et al., 2010), astrometric parallax data from Gaia (Gaia Collaboration et al., 2016), and high-resolution spectroscopic measurements of effective temperatures and metallicities (for example from the *Kepler* Follow-up Program, Furlan et al., 2018) provides an opportunity to test stellar evolution theory at unprecedented precision.

In particular, asteroseismology, which uses oscillation frequencies obtained from analysis of stellar light curves, provides a direct way to test the physics of stellar interiors (Aerts et al., 2010; Basu and Chaplin, 2017). This is possible because the star’s oscillation frequencies are sensitive to the internal structure of the star. By constructing stellar evolution models that seek to reproduce a star’s observed oscillation frequencies and surface properties (for example, luminosity, effective temperature, and metallicity), asteroseismology can be used to study a broad range of physics, including atomic diffusion, rotation, magnetic fields, and convection (for an overview, see, e.g., Chaplin and Miglio, 2013; García and Ballot, 2019). These asteroseismic models can be found using a variety of techniques, including Bayesian inference (e.g., Silva Aguirre et al. 2015, 2017; Aguirre Børsen-Koch et al. 2022), MCMC (e.g., Bazot et al. 2008; Gruberbauer et al. 2012, 2013; Rendle et al. 2019; Bellinger and Christensen-Dalsgaard 2019; Jiang and Gizon 2021), machine learning (e.g., Bellinger et al. 2016, 2019b, 2020b; Angelou et al. 2020; Hon et al. 2020; Guo and Jiang 2023), genetic algorithms (e.g., Metcalfe and Charbonneau 2003; Charpinet et al. 2005; Metcalfe et al. 2009, 2014, 2023), and Levenberg-Marquardt algorithms (e.g., Frandsen et al. 2002; Teixeira et al. 2003; Miglio and Montalbán 2005).

However, for stars with the highest quality asteroseismic data, there are still discrepancies between models and observations. This tension between theoretical and observed frequencies suggests that our models need to be improved, although it does not directly suggest what those improvements should be.

We aim to gain insight into the potential underlying structural differences between stellar models and observations using the technique of asteroseismic structure inversions. This technique uses the differences between the frequencies of an observed star and its model to infer localized information about the structure differences (see e.g., Gough and Thompson 1991; Gough 1993; Pijpers 2006; Bellinger et al. 2020a; Buldgen et al. 2022a).

In the case of the Sun, structure inversions have been used to study the equation of state, diffusion of heavier elements, and nuclear reaction rates in connection to the solar neutrino problem, (for a review see, for example, Basu, 2016; Christensen-Dalsgaard, 2021). The high precision and large number of modes observed for the Sun allow structure inversions to probe a large extent of the solar interior, from $0.06 R_{\odot}$ to $0.96 R_{\odot}$. This, however, is not the case for other stars. Current asteroseismic observations are typically limited to modes of spherical degree $\ell = 0, 1, 2$, with a few $\ell = 3$ modes being observed in the best target stars. This limits the range that can be probed with local structure inversions to the near-core region, fractional radii between ~ 0.05 and 0.35 (Bellinger et al., 2020a).

Nevertheless, there are several examples of structure inversions performed on stars other than the Sun, including the solar analogs 16 Cyg A and 16 Cyg B (Bellinger et al., 2017; Buldgen et al., 2022b), a main-sequence star with a convective core (Bellinger et al., 2019a), and a few subgiants with mixed modes (Kosovichev and Kitiashvili, 2020; Bellinger et al., 2021). Inversion techniques are also being developed for more massive stars (Vanlaer et al., 2023) and more evolved stars (Giannichele et al., 2018). By looking at a larger number

Table 2.1: Grid Parameters

Parameter	Minimum Value	Maximum Value
$M[M_{\odot}]$	0.7	1.2
Y_{initial}	0.24	0.29
Z_{initial}	0.0005	0.07
α_{mlt}	1.3	2.4

of stars, we can test the theory of stellar structure and evolution under a broader range of conditions, such as different masses, metallicities, ages, and evolutionary stages. Examining several stars at once also provides the opportunity to look for overall trends that may hint at deficits in our current understanding of stars. In this work, we focus on studying the most solar-like stars—main-sequence stars with radiative cores—using structure inversions.

2.2. Forward Modeling

The goal of a structure inversion is to infer the differences between the actual stellar structure and that of a reference model. As the structure inversion equation is based on a linear perturbation approach, the reference model must be suitably close to the actual star. Hence, we typically use the best-fit model obtained with some modeling procedure called forward modeling. Here, we describe the forward modeling procedure used to obtain our reference model for each target star. We created a grid of 16384 tracks using the r22.05.01 version of the stellar evolution code MESA (Paxton et al., 2011a, 2013a, 2015a, 2018, 2019a; Jermyn et al., 2022). We vary the initial mass, initial helium mass fraction, metallicity, and mixing-length parameter using a Sobol sequence (see Appendix B of Bellinger et al., 2016; Sobol', 1967). Table 2.1 gives the range that was covered in each parameter.

All models in this grid use metal abundances scaled to the GS98 solar composition (Grevesse and Sauval, 1998), and the corresponding opacity tables from OPAL (Iglesias and Rogers, 1993, 1996) in the high-temperature range, and Ferguson et al. (2005) in the low-temperature range. The equation of state data are calculated with the MESA default blend of OPAL (Rogers and Nayfonov, 2002), SCVH (Saumon et al., 1995), FreeEOS (Irwin, 2004), and Skye (Jermyn et al., 2021). For details of how this blending is handled, see Jermyn et al. (2022). We use the `pp_cno_extras_o18_ne22.net` reaction network and take our reaction rates from JINA REACLIB (Cyburt et al., 2010) and NACRE (Angulo et al., 1999), with additional tabulated weak reaction rates (Fuller et al., 1985; Oda et al., 1994; Langanke and Martínez-Pinedo, 2000). Electron screening is included via the prescription of Chugunov et al. (2007). Thermal neutrino loss rates are from Itoh et al. (1996). Convection in the models is described using the time-dependent local convection formalism of Kuhfuss (1986), which in the limit of long time steps reduces to standard mixing length theory as described in Cox and Giuli (1968). The implementation details are given in Jermyn et al. (2022). We account for atomic diffusion through gravitational settling, as described in Paxton et al. (2011a). We use an Eddington-gray atmosphere and include the structure of the atmosphere out to an optical depth of $\tau = 10^{-3}$ when calculating both our oscillation frequencies and structure kernels. The adiabatic frequencies of the models were computed using GYRE (Townsend and Teitler, 2013; Townsend et al., 2018).

For each target star, we find reference models by fitting the observed frequencies, effective temperature, and metallicity of each star. We take our frequency data from the *Kepler* LEGACY sample (Lund et al., 2017) and the *Kepler* ages (KAGES) sample (Davies et al., 2016). In the case of 16 Cyg A and 16 Cyg B, we use the frequencies given in Roxburgh (2017) labeled as Roxburgh(Davies). Spectroscopic measurements of the effective temperature and metallicity are from the combined stellar parameters reported by the *Kepler* Follow-Up program (Furlan et al., 2018, their Table 9). These values are computed by combining the results of four different spectroscopic analysis pipelines. We also adopt their suggested uncertainties of 100 K, 0.1 dex for T_{eff} and [Fe/H] respectively. The observational parameters we consider for each star are listed in Appendix B.1. For each target star, we search our grid to find the model that minimizes

$$\chi_{\text{fit}}^2 = \chi_{\nu}^2 + \chi_{T_{\text{eff}}}^2 + \chi_{[\text{Fe}/\text{H}]}^2 \quad (2.1)$$

where

$$\chi_{\nu}^2 = \frac{1}{N} \sum_i^N \frac{(v_{i,\text{obs}} - v_{i,\text{mod}})^2}{\sigma_{\nu,i}^2}, \quad (2.2)$$

$$\chi_{T_{\text{eff}}}^2 = \frac{(T_{\text{eff,obs}} - T_{\text{eff,mod}})^2}{\sigma_{T_{\text{eff}}}^2}, \quad (2.3)$$

and

$$\chi_{[\text{Fe}/\text{H}]}^2 = \frac{([\text{Fe}/\text{H}]_{\text{obs}} - [\text{Fe}/\text{H}]_{\text{mod}})^2}{\sigma_{[\text{Fe}/\text{H}]}^2}. \quad (2.4)$$

Here N is the number of frequencies and the subscripts ‘obs’ and ‘mod’ refer to the observations and the model respectively. The model frequencies used to calculate χ_{ν}^2 are first corrected for surface effects using the two-term correction from Ball and Gizon (2014).

We scan our grid to find the parameters ($M, Y_{\text{initial}}, Z_{\text{initial}}, \alpha_{\text{mlt}}, X_c$) that minimize χ_{fit}^2 . In the process, we interpolate in central hydrogen abundance along each track, but we do not interpolate between the tracks. In order to reduce the computational time necessary to find a best-fit model, we consider for subsequent analysis only models that are within 6σ of the effective temperature and metallicity values, as well as within 10σ of the FLAME luminosity value from Gaia DR3 (Gaia Collaboration et al., 2016, 2022; Creevey et al., 2023). We then use these parameters, given in Appendix B.1, to compute the reference model that will be used for structure inversions of each star. We have made the FGONG structure files of our reference models as well as the inlists used to generate them publicly available.¹

2.3. Inversions

With a suitable reference model, we aim to use the differences between the frequencies of an observed star and the frequencies of the reference model to infer the underlying structure differences. We do this through the use of stellar structure kernels, which express the sensitivity of an oscillation mode frequency to a small perturbation to the structure. Mathematically, this is expressed in the kernel equation (Dziembowski et al., 1990):

$$\frac{\delta v_i}{v_i} = \int K_i^{(f_1, f_2)}(r) \frac{\delta f_1}{f_1} dr + \int K_i^{(f_2, f_1)}(r) \frac{\delta f_2}{f_2} dr + O(\delta^2) \quad (2.5)$$

¹<https://zenodo.org/records/10391300>

Here i is the index of the mode which corresponds to a specific pair of radial order (n) and spherical degree (ℓ), $\delta v_i/v_i = (v_{i,\text{obs}} - v_{i,\text{mod}})/v_{i,\text{mod}}$ is the relative difference in frequency between the observed mode ($v_{i,\text{obs}}$) and the corresponding mode of the reference model ($v_{i,\text{mod}}$), f_1 and f_2 are the stellar structure variables being considered, and K_i are the kernel functions of each mode.

The mode kernel functions (K_i) are obtained through a linear perturbation of the oscillation equation (for more details, see Gough and Thompson 1991, Kosovichev 1999, or Thompson and Christensen-Dalsgaard 2002). Initially, mode kernels were derived in terms of the squared sound speed c^2 and density ρ (Dziembowski et al., 1990). From this expression, mode kernels for other pairs of variables have been derived, including for density and the first adiabatic exponent Γ_1 (e.g., Gough and Thompson 1991; Gough 1993), isothermal sound speed $u = c^2/\Gamma_1$ and helium mass fraction Y (e.g., Basu and Christensen-Dalsgaard 1997; Kosovichev 1999; Buldgen et al. 2015a, 2017), and convective stability parameter A and Γ_1 (e.g., Elliott 1996; Kosovichev 1999; Buldgen et al. 2017). For more details on changing the structure variable pair, see Kosovichev (2011); Buldgen et al. (2017). Equation 2.5 can also include a term that corrects for the surface effect; however, we instead correct for this in the calculation of the frequency differences. For the remainder of this paper, when we discuss model frequencies, we refer to the frequencies that have been corrected for surface effects.

Each oscillation mode is sensitive to many points within the star, so to obtain localized information we implement the method of optimally localized averages (OLA, Backus and Gilbert 1968, 1970) which uses a linear combination of the frequency differences. Neglecting second-order effects, Equation 2.5 becomes

$$\sum_{i=1,N} c_i \frac{\delta v_i}{v_i} = \int \mathcal{K}(r) \frac{\delta f_1}{f_1} dr + \int C(r) \frac{\delta f_2}{f_2} dr. \quad (2.6)$$

Here \mathcal{K} is the averaging kernel and C is the cross-term kernel. These are constructed using a set of inversion coefficients c_i :

$$\mathcal{K} = \sum_{i=1,N} c_i K_i^{(f_1, f_2)} \quad \text{and} \quad C = \sum_{i=1,N} c_i K_i^{(f_2, f_1)}. \quad (2.7)$$

If \mathcal{K} is normalized to 1 and C is small, then Equation 2.8 reduces to

$$\sum_{i=1,N} c_i \frac{\delta v_i}{v_i} \approx \int \mathcal{K}(r) \frac{\delta f_1}{f_1} dr \approx \left\langle \frac{\delta f_1}{f_1} \right\rangle, \quad (2.8)$$

and \mathcal{K} can be interpreted as the weight function of a mean over the structure difference $\delta f_1/f_1$. This is why \mathcal{K} is called the averaging kernel. In other words, if the coefficients c_i are chosen such that \mathcal{K} has most of its amplitude around a single target radius, r_0 , then the same linear combination of frequency differences provides a localized average difference of the structure variable f_1 at that target radius.

2.3.1. Localized averaging kernels

To construct a localized averaging kernel, we use the method of multiplicative optimally localized averages (MOLA). For a MOLA inversion, we define a weight function, $J = (r - r_0)^2$, that penalizes any amplitude of the averaging kernel away from the target radius.

In addition to the target radius, there are two trade-off parameters that must be chosen: the error suppression parameter, μ , and the cross-term suppression parameter, β . The inversion coefficients are found by minimizing

$$\int \left(\sum_{i=1,N} c_i K_i^{(f_1, f_2)} \right)^2 J(r_0, r) dr + \beta \int \left(\sum_{i=1,N} c_i K_i^{(f_2, f_1)} \right)^2 dr + \mu \sum_{i=1,N} c_i c_j E_{ij}, \quad (2.9)$$

where E_{ij} are the elements of the error-covariance matrix. Strictly speaking, there is another trade-off parameter in this formulation, the normalization of J , which we have set to 1, while other implementations often use 12. However, this only changes the relative weight of the first term in Equation 2.9 and can be counteracted by changing μ or β . Thus, while the optimal values of μ and β vary with the normalization of J , the inversion results do not.

The other standard method of constructing an averaging kernel is a variant of MOLA known as the method of subtractive optimally localized averages (SOLA, Pijpers and Thompson 1992, 1994). Previous works studying 16 Cyg A and 16 Cyg B have used SOLA (Bellinger et al., 2017; Buldgen et al., 2022b). We choose to use MOLA because it requires setting only two free parameters, as opposed to the three required for a SOLA inversion. Additionally, we find that MOLA is better able to suppress the amplitude of the averaging kernel at the surface. For details on the differences between MOLA and SOLA see Basu and Chaplin (2017, Chapter 10).

The next important consideration for a structure inversion is which pair of structure variables to use. We use the u, Y pair because the Y kernels have low amplitude everywhere except in helium ionization zones (Basu, 2003), which naturally suppresses the cross-term kernel at the radii we are targeting. The trade-off to this approach is that using Y as a structure variable requires the assumption of an equation of state. In the solar case, the error introduced by this assumption is significant in comparison to the other sources of uncertainty (Basu and Christensen-Dalsgaard, 1997); however, due to the larger uncertainties on asteroseismic frequencies this is not the case for stars other than the Sun. Using Y as a structure variable requires calculating several partial derivatives of Γ_1 . To be consistent with the blend of equation of state tables used in MESA, we obtained these directly from MESA's equation of state module.

2.3.2. Trade-off parameters

As Equation 2.9 shows, there are two trade-off parameters that must be chosen in the course of a structure inversion. The parameter μ controls the balance between a well-localized averaging kernel and the amplification of uncertainties. To choose an appropriate value of μ for each inversion, we utilize a set of calibration proxy models. These models are found using the process described in Section 2.2; however, they have slightly higher χ_{fit}^2 values than the reference model. Since the structure of these models is known exactly, they can be used to determine how well the inversion recovers the underlying differences. We provide the details of this process in Appendix B.2.1. Before accepting our inversion results, we visually inspect the averaging and cross-term kernels of all target radii for each star to ensure that the averaging kernels are well localized and the overall amplitudes of the cross-term kernels are low.

2.3.3. Stellar mass & radius

Another complication for inversions of stars other than the Sun is the lack of precise measurements of the stellar mass and radius. Since the frequencies of a star scale with its mean density, a mismatch in the mean density will lead to an offset in the inversion results (Basu, 2003). To minimize this, we invert for the relative difference in $\hat{u} = uR/M$, where R and M are the star's radius and mass, respectively. This is done by using mode kernels computed in a dimensionless form and using the dimensionless frequency differences. Previously, Bellinger et al. (2021) used dimensionless frequency differences calculated by subtracting off the weighted mean of the frequency differences (for details, see Basu 2003).

We have found that this method results in correct dimensionless frequencies only when the frequency differences caused by an incorrect mean density are larger than the differences introduced by the structural variation. Whether this is true cannot be determined purely by comparing the observed and modeled frequencies. Instead, we use a new method of calculating the dimensionless frequency differences using the dependence of the large frequency separation ($\Delta\nu$) on the mean density. The large frequency separation is the mean frequency difference between successive radial modes and is a proxy for the root mean density of the star (Vandakurov, 1967). The details of this method can be found in Appendix B.2.2.

We calculate our value of $\Delta\nu$ by taking the slope of a linear fit to the relationship between the $l = 0$ modes and their respective radial orders and use this to calculate the dimensionless frequency differences. These corrections mean that the uncertainties of our frequency differences are no longer independent, and hence, the error covariance matrix E , used in Equation 2.9 is not diagonal. We calculate it using a Monte Carlo simulation where each frequency is perturbed 10 000 times with Gaussian noise according to their measured uncertainties. These perturbations are applied before the frequencies are corrected for the surface effect, and so this procedure also accounts for the error correlation introduced by the surface term correction. This same set of perturbed frequencies is then used to calculate the final inversion results. We take the average of this distribution as our final inversion result and report the standard deviation as the uncertainty.

This method of uncertainty estimation occurs after both the reference model and inversion parameters have been selected, and only propagates uncertainties due to the underlying frequencies. It is the same as the traditional definition of inversion uncertainties (e.g., Equation 4 of Bellinger et al. 2019a) except that it accounts for any correlation introduced during the pre-processing of our frequency differences.

To validate both our method of finding reference models and our inversion results, we also obtain a reference model and inversion results using solar data that have been degraded to the level that was expected of results from *Kepler*. These results are given in Appendix B.2.3.

2.3.4. Overall inversion significance

For each star, we attempt structure inversions at six target radii,

$$r_0/R = 0.05, 0.10, 0.15, 0.20, 0.25, 0.30,$$

although in some cases we are only able to find suitable averaging kernels at five target radii. To quantify the disagreement between each target star and its model, across all target radii, we calculate a χ_{inv}^2 as follows. For each star, there is a set of inversion results and their associated uncertainties $v_j \pm u_j$. Since all the target radii use the same underlying data, their

errors are correlated. The correlation between two target radii, r_j, r_k , is (Basu and Chaplin, 2017)

$$E_{r_j, r_k} = \frac{\sum_i c_i(r_j) \cdot c_i(r_k) \sigma_i^2}{\left[\sum_i c_i^2(r_j) \sigma_i^2 \right]^{1/2} \left[\sum_i c_i^2(r_k) \sigma_i^2 \right]^{1/2}}, \quad (2.10)$$

where $c_i(r_j)$ is the inversion coefficient of the i -th mode for the j -th target radius and σ_i is the relative uncertainty of the i th mode frequency. The error correlation matrix, \mathbf{E} , is the matrix with components E_{r_j, r_k} between all different target radii. The covariance matrix then is

$$\mathbf{C} = \mathbf{U}^T \mathbf{E} \mathbf{U}, \quad (2.11)$$

where \mathbf{U} is a diagonal matrix with the uncertainty of the inversion result for each target radius. Then

$$\chi_{\text{inv}}^2 = \mathbf{V}^T \mathbf{C}^{-1} \mathbf{V}, \quad (2.12)$$

where \mathbf{V} is the vector of inversion results at each target radius. This χ_{inv}^2 summarizes the overall significance of the inversion results for each star across all target radii, with larger values indicating larger disagreement.

In summary, after finding a reference model, we calculate the surface-term-corrected dimensionless frequency differences between the target star and the model. We then use our set of calibration models to choose μ at each target radius and obtain our set of averaging kernels. With this, we use the inversion coefficients and the frequency differences to obtain our inferred localized differences in \hat{u} between the observed star and our reference model.

2.4. Results and Discussion

Together, the *Kepler* LEGACY and KAGES samples provide oscillation data for 95 stars. Since we are specifically searching for close matches to stars with radiative cores, we apply two criteria to our reference models: that they have a radiative core throughout their main-sequence evolution and that they have a $\chi_{\text{fit}}^2 < 20$. We obtain suitable reference models for 34 stars. Of these, 12 have enough frequencies observed (approximately 35) to form well-localized averaging kernels.

Figure 2.1 shows the inversion results for each of these 12 stars as a function of the target radius. We define our relative differences such that a positive inversion result indicates a sound speed that is higher in the star than in the model. We provide more information about the reference model and averaging kernels of each star in Appendix B.3.

The inversion results of the twelve stars in our sample can be broken down into three groups: (a) those where the \hat{u} of the best-fit model is in agreement with the observations, (b) those where the \hat{u} of the model is too high (resulting in an inversion result below zero), and (c) those where the \hat{u} is too low (resulting in an inversion result above zero). Taking into account the uncertainties of the inversion results, we identify six stars in group a, one star in group b, and six stars in group c. Thus, half of our sample show significant differences, which suggests that there are limitations in the physics of our reference models and that these limitations most often result in internal values of \hat{u} that are too low.

Now we seek to understand why some of our stellar models show good agreement in \hat{u} while others show significant disagreement. We search for correlations between χ_{inv}^2 and properties of the reference model, as well as the surface rotation rate (P_{rot}) and magnetic activity indicator (S_{ph}) values for each star, as given by Santos et al. (2018). We calculate

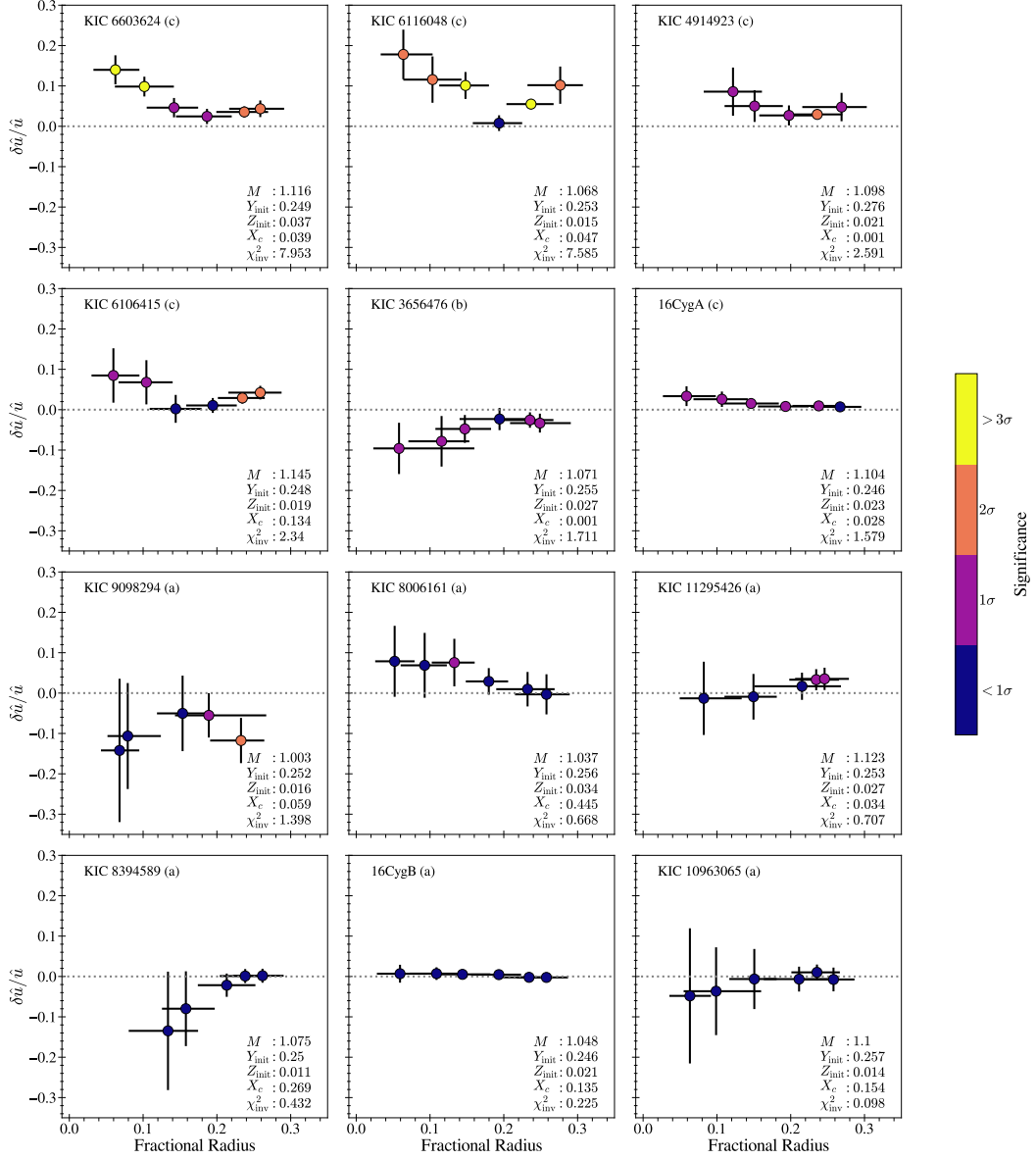


Figure 2.1: Comparisons of the internal structure of stars as revealed by asteroseismology and the structures of best-fitting stellar evolution models. Relative differences are given in terms of the dimensionless squared isothermal sound speed \hat{u} and span the near-core region of 0.05-0.3 away from the stellar center point. The points indicate the inferred value of $\delta\hat{u}/\hat{u}$ between the star and the reference model at the target radius. The vertical error bars indicate the uncertainty of each inversion result from the propagation of the uncertainty of the observed frequencies. The horizontal error bars represent the full width at half maximum of the averaging kernel. The dashed horizontal line indicates complete agreement between the model and observations; points above this line imply that \hat{u} of the star is larger than that of the model. The color bar indicates the statistical significance of the inferred difference, with lighter colors showing more significant results. The letter after the star's identifier indicates which group the star is in, as described in the text. The values given in the lower left of each plot indicate the mass ($M[M_{\odot}]$), initial helium mass fraction (Y_{init}), initial metallicity (Z_{init}), and central hydrogen mass fraction (X_c) of each reference model. We also report the overall significance of the inversion results, χ_{inv}^2 .

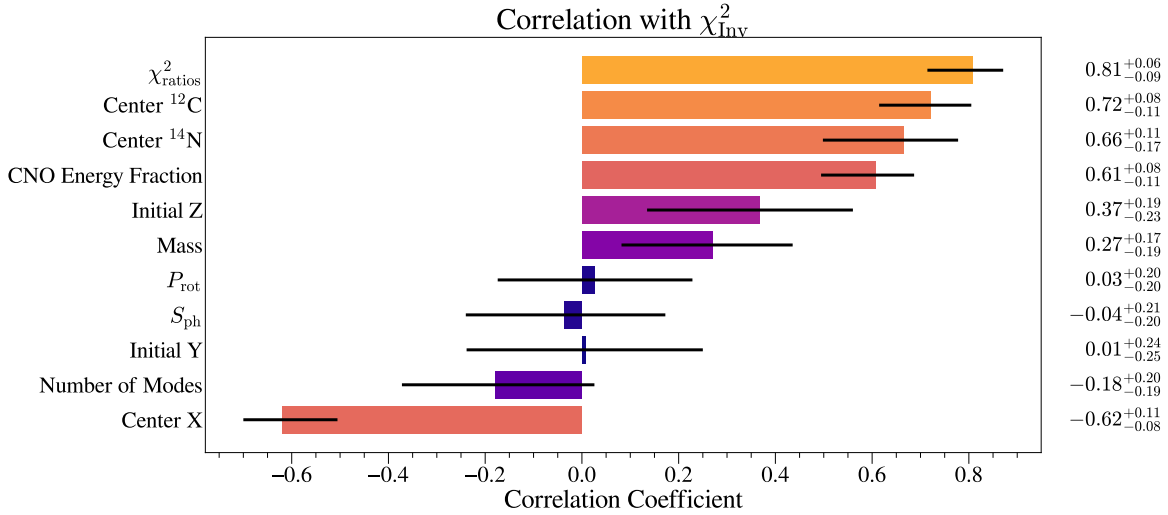


Figure 2.2: Spearman rank correlation between the maximum significance inversion result of each star and various properties of the reference model. The color correlates with the absolute value of the correlation coefficient, which is a measure of the strength of the correlation. The value of each correlation coefficient is provided on the right side of the figure. We estimate the uncertainty of each correlation coefficient using bootstrapping.

Spearman’s rank correlation coefficient, ρ_s , which describes the strength of the monotonic, but not necessarily linear, correlation between two variables. These results are shown in Figure 2.2. We use bootstrapping to obtain estimates of the uncertainty of these coefficients.

The strongest correlation is with χ^2_{ratios} ($\rho_s = 0.81$). This χ^2 is a measure of how well our reference model matches the observed frequency separation ratios (r_{10}, r_{02}) of the observed star. These ratios are known to be insensitive to the surface effect, (Roxburgh and Vorontsov, 2003) and thus χ^2_{ratios} serves as a different metric for how well the internal structure of a star is reproduced in the model. The strong correlation between χ^2_{ratios} and χ^2_{inv} reaffirms that the differences found from structure inversions are internal structure differences rather than problems with the near-surface layers.

We find significant positive correlations of the discrepancies between the star and stellar model with the central abundance of ^{12}C ($\rho_s = 0.72$) and ^{14}N ($\rho_s = 0.66$) of the model, as well as the amount of energy generated by the CNO cycle ($\rho_s = 0.61$). A similar-strength correlation in the opposite direction is found with the central hydrogen abundance ($\rho_s = -0.62$). That all of these properties have a similar strength of correlation is unsurprising, as they are mutually correlated. When the central hydrogen value is lower, reactions other than the pp-chain can happen more easily. Primarily, this is an increase in energy generated by the CNO cycle. At the same time, a very small amount of energy is generated by the triple-alpha process. This is not significant compared to the total energy generation of the star, but it does increase the equilibrium abundance of ^{12}C . Additionally, the CNO-II pathway converts ^{16}O into ^{14}N which increases the equilibrium abundance of ^{14}N . In general, we see a moderate correlation between the significance of the \hat{u} differences inferred by inversions and more evolved main sequence stars.

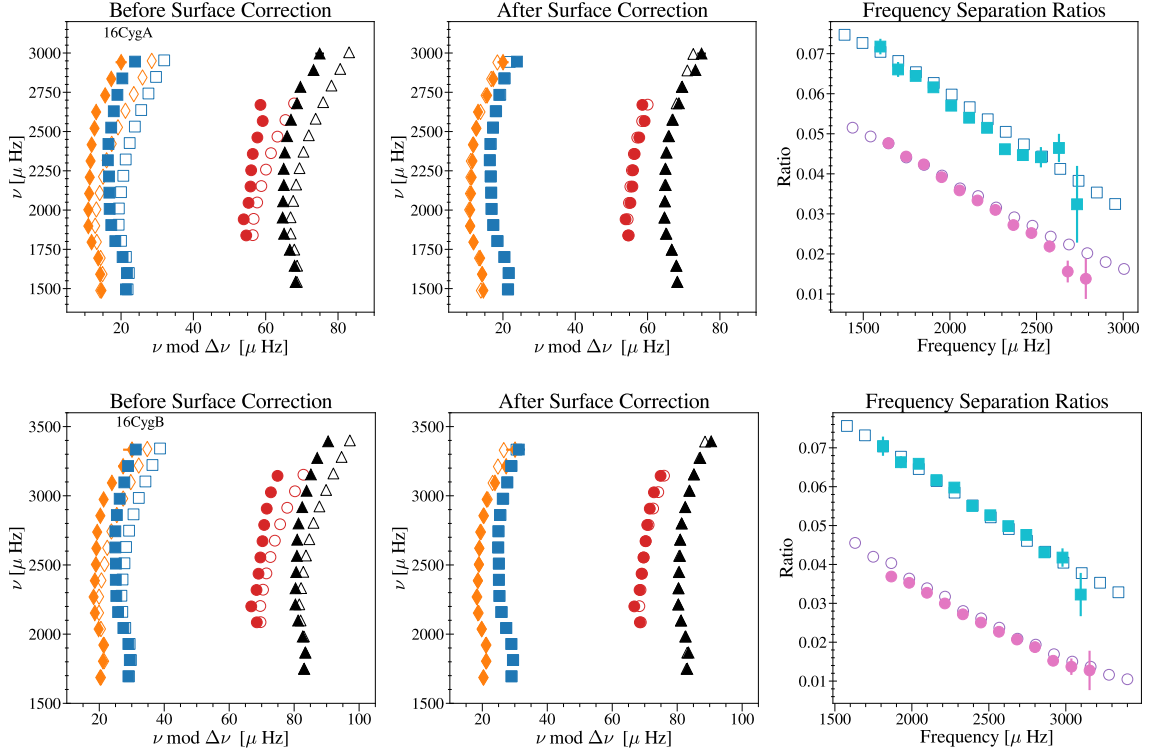


Figure 2.3: Modeling results for 16 Cyg A (top) and 16 Cyg B (bottom). In each case, the left plot shows the Frequency Échelle diagram comparing the frequencies of the reference model to the observations before applying any correction to account for surface effects. The center panel compares the reference model frequencies after applying the two-term surface correction from Ball and Gizon (2014). The color and shape indicate the spherical degree ℓ : 0 (blue squares), 1 (black triangles), 2 (orange diamonds), and 3 (red circles). The right plot shows the frequency separation ratios r_{10} (pink) and r_{02} (light blue). In all plots, the open points represent the values from the reference model and the filled points represent the observed values.

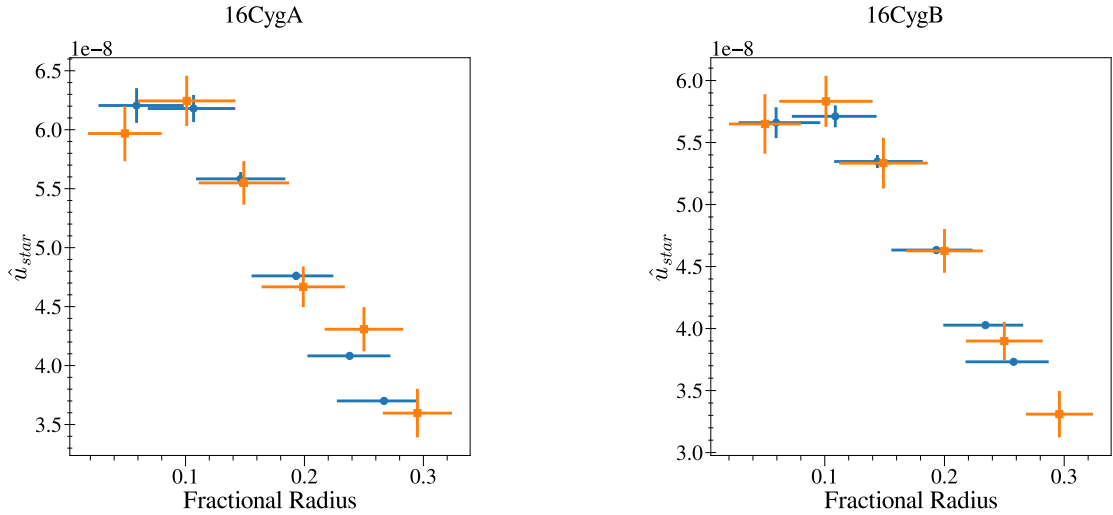


Figure 2.4: Inversion results for 16 Cyg A (left) and 16 Cyg B (right). The blue points show the inversion results from this work. The orange points are the results from Bellinger et al. (2017). Since they report u we use their reported values of M and R to calculate \hat{u} .

2.4.1. Individual Stars

We now discuss the results of both our forward modeling and inversion procedures for a few individual stars.

2.4.1.1 16 Cyg A and 16 Cyg B

First, we focus on the solar analogs 16 Cyg A and 16 Cyg B. In Figure 2.3 we compare the frequencies (before and after surface-term corrections) and frequency separation ratios of our reference models with the observations. As these are two of the most well-studied main sequence stars in the *Kepler* field, they have already been studied using structure inversions by Bellinger et al. (2017); Buldgen et al. (2022b). In our results, as well as the two previous studies, there is excellent agreement between the models and the observations. In the case of 16 Cyg B, the models used in all three works are within 1σ agreement with observations. For the case of 16 Cyg A, our inversions show differences that are less than 1.5σ , which is similar to the values obtained by Bellinger et al. (2017) and Buldgen et al. (2022b). Bellinger et al. (2017) report their inferred u values, as well as their inferred values of the stellar mass and radius, which allows us to compare \hat{u} values directly, as shown in Figure 2.4. All the points for 16 Cyg B are in good agreement. For 16 Cyg A, there is slight disagreement at a target radius of 0.25, but it is not significant. Despite the use of different reference models, a different implementation of OLA, and different inversion parameters, we agree on the internal sound speed profiles of both 16 Cyg A and 16 Cyg B.

2.4.1.2 KIC 6116048 and KIC 6603624

We now turn to the two stars in our sample that show the largest differences with respect to our models: KIC 6603624 and KIC 6116048. We show the frequencies and frequency separation ratios in Figure 2.5. Both of these stars have points where our inversions infer internal sound speed differences greater than 10 percent, and in contrast to other stars in the sample, these large differences are significant compared to their uncertainties, so first we verify that our inversions are able to recover differences of this magnitude. The $\delta\hat{u}/\hat{u}$ between our reference model for KIC 6116048 and our reference model for KIC 6603624 reach $\sim 15\%$ in the region probed by structure inversions, and so we test our averaging kernels by attempting to recover the difference between the two models. We do this twice, once with KIC 6603624 as the reference model and then again using KIC 6116048 as the reference model. The results of these inversions are shown in Figure 2.6. Both sets of averaging kernels infer the correct shape of the true $\delta\hat{u}/\hat{u}$ curve. The averaging kernels of KIC 6603624 infer the correct value of $\delta\hat{u}/\hat{u}$ within the uncertainties at every target radius. This is not the case for the averaging kernels for KIC 6116048, where two points differ from the correct value by $\sim 2\sigma$. Nevertheless, we conclude that our inversion procedure is able to recover differences around 15%.

2.4.2. Exploring the effects of microphysics

We now explore several changes to the microphysics in our models in an attempt to reduce the sound speed differences inferred by our inversions. A full investigation of the microphysics across all twelve of the stars studied here is beyond the scope of this work, and hence we focus on KIC 6603624 and KIC 6116048, the two stars discussed in Section 2.4.1.2. For

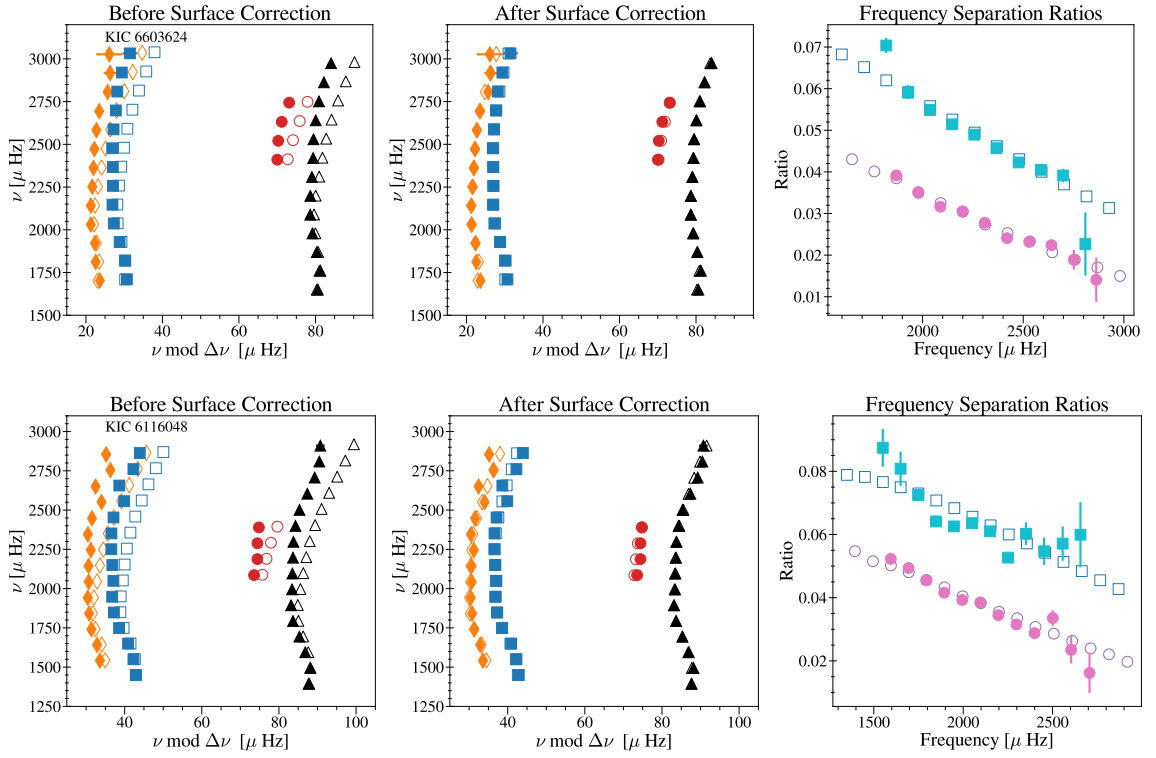


Figure 2.5: Modeling results for KIC 6603624 (top) and KIC 6116048 (bottom). All symbols have the same meaning as in Figure 2.3.

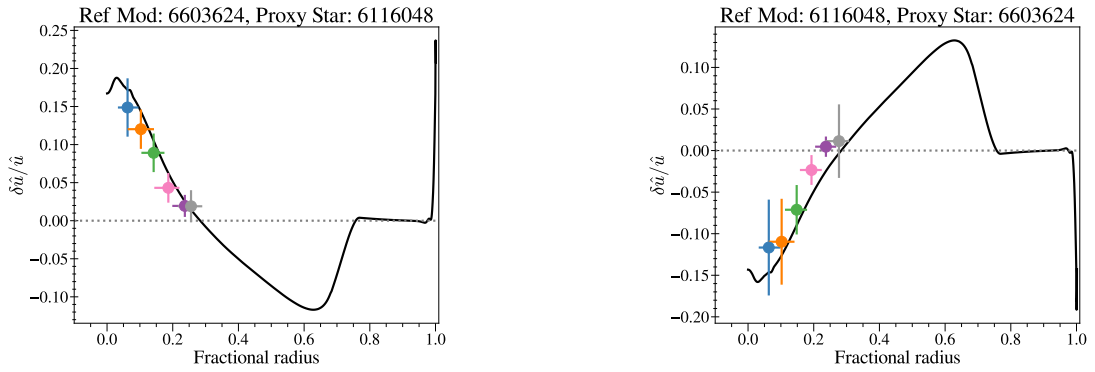


Figure 2.6: Model-model inversions to recover the \hat{u} difference between the model for KIC 6603624 and KIC 6116048. The left figure shows the result of using KIC 6603624 as the reference model, and the right figure shows the result of using KIC 6116048 as the reference model. In both plots, the black line represents the true value of $\delta\hat{u}/\hat{u}$ and the colored points show the result of the inversion. Different target radii are shown in different colors and correspond to the color of the averaging and cross-term kernels shown in Figures B.4 and B.5.

[

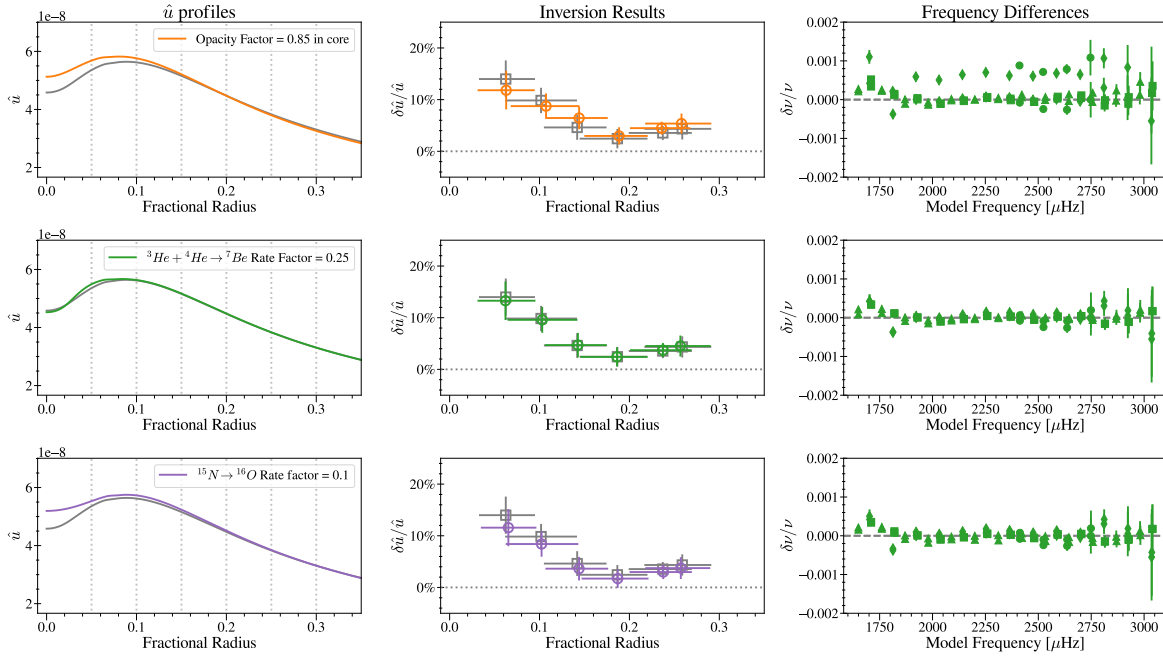


Figure 2.7: Results of modifying the physics used to evolve each model. The \hat{u} profile of each model is shown in the left plot, with light gray dashed vertical lines to indicate the target radii of the inversions. The center plot shows the result of structure inversions using each model as the reference model. The right plot shows the frequency differences between each model and the observed modes of KIC 6603624. The shape of the marker denotes the spherical degree of the mode, with $l = 0, 1, 2, 3$ denoted by squares, triangles, diamonds, and circles respectively. In each plot, gray lines and points represent the values of the original reference model of KIC 6603624.

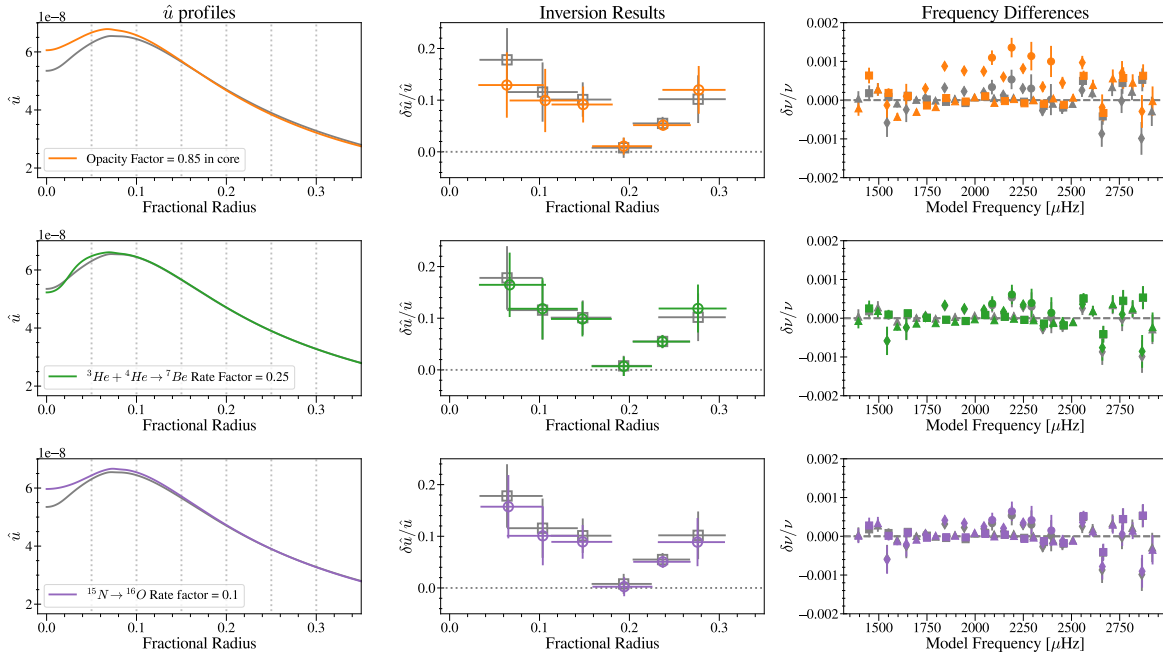


Figure 2.8: Results of modifying the physics used to evolve each model of KIC 6116048. All colors and symbols have the same meaning as in Figure 2.7.

each star, we create three new models using the same mass, initial composition, and mixing-length parameter as our original reference model, although we allow these new models to have a different central hydrogen abundance. For the first model, motivated by the correlation to CNO energy production, we multiply the rate of the $^{14}\text{N} + \text{p} \rightarrow ^{15}\text{O} + \gamma$ reaction by a factor of 0.1. For the second model, we multiply the ppII/ppIII rate $^3\text{He} + ^4\text{He} \rightarrow ^7\text{Be} + \gamma$ by a factor of 0.25. For the last model, we modify the opacity by a factor of 0.85 in the parts of the model with $\log T > 6.7$. For each of these three new tracks, we select a new reference model using the fitting procedure discussed in Section 2.2.

Figures 2.7 and 2.8 show the results of these changes for KIC 6603624 and KIC 6116048, respectively. For each change in the microphysics, we show the \hat{u} profiles of each new reference model as well as the result of structure inversions. The changes to the core opacity and the $^{14}\text{N} + \text{p} \rightarrow ^{15}\text{O} + \gamma$ reaction rate both increase \hat{u} from the original reference model, with the opacity change resulting in a larger difference both to the central \hat{u} and the frequency differences computed with respect to the observations. The change caused by modifying the $^3\text{He} + ^4\text{He} \rightarrow ^7\text{Be} + \gamma$ reaction rate results in a smaller change to the \hat{u} that is only apparent inside $r/R < 0.07$. As expected, when we apply changes that increase the internal \hat{u} , the \hat{u} difference inferred by the structure inversion decreases. We find better agreement in the \hat{u} profile even when the fit of the model is worse than our original reference model. These changes improve our models at the deepest target radii but have little effect at the larger radii probed by inversions.

2.5. Conclusions

Here, we have used asteroseismology to infer the detailed core structure of the best solar-type stars observed by the *Kepler* mission. We focused on main-sequence stars with radiative cores and expanded the number of such stars studied with structure inversions from 2 to 12. After obtaining our reference models from a grid created using MESA, we use a set of calibration models to obtain our inversion parameters. We then use these inversion parameters to infer the relative difference in dimensionless squared isothermal sound speed between our reference model and the target star. In our sample, we identify three groups: those where the \hat{u} of our reference model agrees with the observed star (group a, 6 stars), those where the \hat{u} of our model is higher than that of the star (group b, 1 star), and those where the \hat{u} of our model is lower than that of the star (group c, 5 stars). We also find significant correlations in our results, suggesting that our models of older main-sequence stars with more energy being generated by the CNO cycle have larger differences between the model and the star. To explore how changing the microphysics affects our inversion results, we tested the effects of changing nuclear reaction rates and core opacities, for the two stars with the most significant differences. These changes to the microphysics reduced the discrepancy between the model and the star at the innermost target radii.

In future work, we aim to extend our analysis to an even broader set of stars, including main-sequence stars with convective cores and more evolved stars with mixed-mode oscillations. Main-sequence stars with convective cores are particularly interesting since their dominant source of energy is the CNO cycle. Thus, they are a natural next step to explore the correlations found in this work between the inferred sound speed differences and CNO energy production.

Acknowledgments We thank the anonymous referee for their constructive feedback that improved the manuscript considerably. The research leading to the presented results has received funding from the ERC Consolidator Grant DipolarSound (grant agreement #101000296). SB acknowledges NSF grant AST-2205026. SB would also like to thank the Heidelberg Institute of Theoretical Studies for their hospitality during the early days of this project. This paper includes data collected by the Kepler mission. Funding for the Kepler mission is provided by the NASA Science Mission Directorate. In addition, this work has made use of data from the European Space Agency (ESA) mission *Gaia* (<https://www.cosmos.esa.int/gaia>), processed by the *Gaia* Data Processing and Analysis Consortium (DPAC, <https://www.cosmos.esa.int/web/gaia/dpac/consortium>). Funding for the DPAC has been provided by national institutions, in particular, the institutions participating in the *Gaia* Multilateral Agreement. We have also used the *gaia-kepler.fun* crossmatch database created by Megan Bedell.

Asteroseismic Structure Inversions of Main-Sequence Solar-like Oscillators with Convective Cores

AUTHORS Lynn Buchele, Earl P. Bellinger, Saskia Hekker, and Sarbani Basu

CHAPTER INFO This chapter is a reproduction of a paper that has been submitted¹ to the *Astrophysical Journal* and is currently under review. It extends the analysis introduced in Chapter 2 to 43 main-sequence stars with convective cores. I am the first author. All of the modeling, inversion analysis, and writing was done by me with supervision, advice, and input from all co-authors.

ABSTRACT Asteroseismic inferences of main-sequence solar-like oscillators often rely on best-fit models. However, these models cannot fully reproduce the observed mode frequencies, suggesting that the internal structure of the model does not fully match that of the star. Asteroseismic structure inversions provide a way to test the interior of our stellar models. Recently, structure inversion techniques were used to study 12 stars with radiative cores. In this work, we extend that analysis to 43 main-sequence stars with convective cores observed by *Kepler* to look for differences in the sound speed profiles in the inner 30% of the star by radius. For around half of our stars, the structure inversions show that our models reproduce the internal structure of the star, where the inversions are sensitive, within the observational uncertainties. For the stars where our inversions reveal significant differences, we find cases where our model sound speed is too high and cases where our model sound speed is too low. We use the star with the most significant differences to explore several changes to the physics of our model in an attempt to resolve the inferred differences. These changes include using a different overshoot prescription and including the effects of diffusion, gravitational settling, and radiative levitation. We find that the resulting changes to the model structure are too small to resolve the differences shown in our inversions.

¹A previous draft has already been posted as an e-print at <https://arxiv.org/abs/2412.05094>

3.1. Introduction

Among the stars observed by *Kepler*, high-precision oscillation mode frequencies have been determined for around 100 main-sequence solar-like oscillators (Davies et al., 2016; Lund et al., 2017). This sample has been used to study a variety of physical processes including chemical transport (Nsamba et al., 2018; Deal et al., 2018; Verma and Silva Aguirre, 2019; Moedas et al., 2022, 2024), convection in stellar cores (Angelou et al., 2020; Zhang, 2020; Noll and Deheuvels, 2023), rotation (B  trisey et al., 2023), and magnetic fields (Santos et al., 2018; Salabert et al., 2018; Kiefer and Broomhall, 2020). This work often involves finding a best-fit model for each star using a stellar evolution code. Best-fit models are generally found by matching the observed frequencies of a star or by fitting parameters derived from those frequencies, such as the frequency separation ratios (Roxburgh and Vorontsov, 2003) or glitch signatures due to helium ionization (Verma et al., 2017), while matching the position of the star on the HR diagram. In general, however, these models are unable to fully reproduce the observed parameters, suggesting that there are still some deficits in our understanding of stellar interiors.

Fortunately, the large number of precise oscillation modes observed in these stars makes it possible to take the analysis further using structure inversions. This technique, developed for geology (Backus and Gilbert, 1968) and used extensively in helioseismology (for a review see, for example, Basu, 2016; Christensen-Dalsgaard, 2021), uses the inherent sensitivity of each oscillation mode to infer differences between the interior structure of a star and a given best-fit model (see e.g., Gough and Thompson 1991; Gough 1993; Pijpers 2006; Bellinger et al. 2020a; Buldgen et al. 2022a). These inferred differences can be used to test how well the interior structure of our models matches that of observed stars, as well as provide information on what changes may be necessary to improve our models.

In Figure 3.1, we show the existing sample of main-sequence solar-like oscillators studied using asteroseismic structure inversions. Buchele et al. (2024b), reproduced as Chapter 2 in this thesis, and henceforth B24, presented results for 12 stars with radiative cores, including the solar analogs 16 Cyg A and B which were also studied by Bellinger et al. (2017) and Buldgen et al. (2022b). Structure inversions have also been used to study a main-sequence star with a small convective core (Bellinger et al., 2019a) and two stars evolved enough to exhibit mixed modes (Kosovichev and Kitiashvili, 2020). All three of these stars are in the sample presented here, where we extend the work of B24 to cover main-sequence solar-like oscillators with convective cores observed by *Kepler*.

3.2. Forward Modeling

As structure inversions infer differences between a star and a model, the first step is to find a suitably close reference model, typically the best-fit model from a grid-based modeling or optimization procedure. The process of finding such a model is called forward modeling. To find our reference models, we used a grid-based method similar to that used by B24. We constructed a grid of 24,530 tracks using the stellar evolution code MESA (Paxton et al., 2011a, 2013a, 2015a, 2018, 2019a; Jermyn et al., 2023a). The details of the grid that are unchanged between this work and B24 are provided in Appendix C.1.1. There are two important changes which we discuss here.

It is well known that including diffusion and gravitational settling of elements without also including the effects of radiative levitation produces models with unrealistic surface

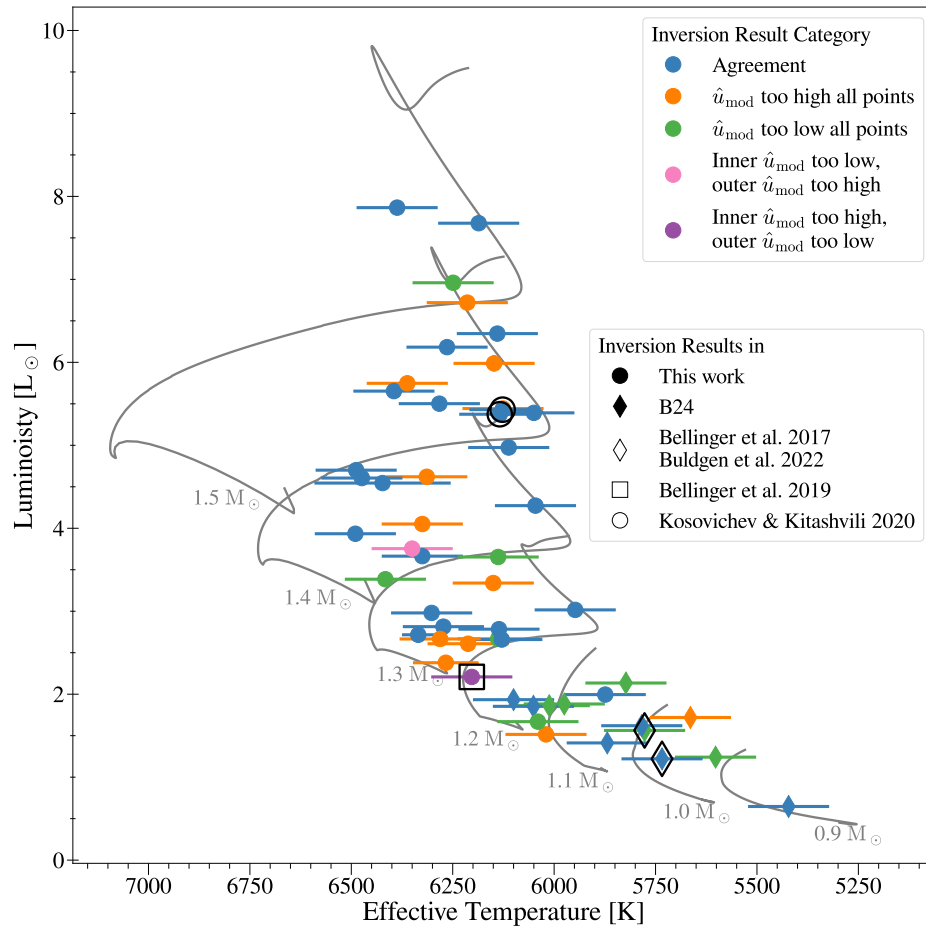


Figure 3.1: Hertzsprung–Russell diagram for main-sequence solar-like oscillators with inversion results available. Stars have been categorized based on their inversion results in this work and in B24, represented by the color of the symbol. Stars with other inversion results available are indicated with larger open symbols. The uncertainties of the luminosity values are smaller than the points. Stellar evolutionary tracks of several masses are shown for reference.

abundances in this mass range (e.g., Michaud et al., 2015; Deal et al., 2018). However, including radiative levitation significantly increases the computation time of models, such that it would be difficult to compute the number of models necessary to cover the parameter space of the observations. We chose to compromise and evolve our tracks without including diffusion, settling, or radiative levitation. Additionally, since we are dealing with stars with convective cores, we use the exponential overshooting (Freitag et al., 1996; Herwig, 2000) scheme implemented in MESA where the overshoot region is treated as fully mixed without changing the thermal gradient. This is described in detail in Paxton et al. (2011a). The parameters varied in this grid are mass, initial helium abundance, initial metallicity, mixing length parameter, and overshooting parameter. To cover the parameter space efficiently, we varied each parameter using a Sobol sequence (see Appendix B of Bellinger et al., 2016; Sobol', 1967) within the ranges listed in Table 3.1. For each model in the grid, we calculated the adiabatic frequencies using GYRE (Townsend and Teitler, 2013).

We then scanned the grid to find the model parameters that best fit the frequencies, effective temperature, and metallicity by minimizing:

$$\chi_{\text{fit}}^2 = \frac{(T_{\text{eff,obs}} - T_{\text{eff,mod}})^2}{\sigma_{T_{\text{eff}}}^2} \quad (3.1)$$

$$+ \frac{([\text{Fe}/\text{H}]_{\text{obs}} - [\text{Fe}/\text{H}]_{\text{mod}})^2}{\sigma_{[\text{Fe}/\text{H}]}^2} \quad (3.2)$$

$$+ \frac{1}{N} \sum_i^N \frac{(\nu_{i,\text{obs}} - \nu_{i,\text{mod}})^2}{\sigma_{\nu,i}^2}, \quad (3.3)$$

where N is the number of observed frequencies, ν_i is the frequency that corresponds to the i -th pair of radial order (n) and spherical degree (ℓ) where the model's frequencies have been corrected for surface effects using the two-term correction from Ball and Gizon (2014), σ denotes the uncertainty of the observed parameter, and the subscripts 'obs' and 'mod' denote the observations and the model, respectively. Our definition of χ_{fit}^2 treats all the frequencies as a single observation with the same weight as each spectroscopic observation. This choice is common in asteroseismic modeling pipelines (see, for example, the ASTFIT pipeline described in Silva Aguirre et al. 2015). Each mode can be treated as an independent observation by removing the factor of $1/N$. In synthetic tests, Cunha et al. (2021) find that this weighting recovers the correct stellar parameters only when the physics of the grid matches the physics of the synthetic star exactly. As we perform structure inversions in order to determine if the physics in our models accurately represents what we observe, we, therefore, opt to treat all frequencies as a single observation.

While scanning the grid, we interpolated along each track, but not between tracks. This is the same method as that of B24 with one change — in this work, we interpolated in age instead of central hydrogen abundance, as the central hydrogen abundance does not decrease monotonically in stars where a convective core emerges after the zero-age main sequence. From this procedure, we obtain the best-fit parameters, which are then used to calculate the reference model of the structure inversions. Our values of T_{eff} and $[\text{Fe}/\text{H}]$ come from Furlan et al. (2018); Mathur et al. (2017); Morel et al. (2021), with the specific source for each star given in Appendix C.1.2. We also provide, in Appendix C.1.2, the parameters of our best-fit model as well as a comparison to the parameters reported in Silva Aguirre et al. (2017).

Table 3.1: Grid Parameters

Parameter	Minimum Value	Maximum Value
M/M_{\odot}	1.1	1.7
Y_{initial}	0.24	0.4
Z_{initial}	0.0005	0.07
α_{mlt}	1.3	2.4
f_{ov}	0	0.08

3.3. Structure Inversions

With a suitable reference model for each star in our sample, we now turn to the process of an asteroseismic structure inversion. Structure inversions use the frequency differences between a star and its best-fit model to infer the underlying structure differences. We chose to express the structure differences in terms of the dimensionless squared isothermal sound speed (\hat{u}) and helium mass fraction (Y). In terms of the more common structure variables of pressure (P) and density (ρ),

$$\hat{u} = \frac{P}{\rho} \frac{R}{M} \quad (3.4)$$

where R and M are the stellar radius and mass, respectively. This choice of variables is well suited for asteroseismic targets (Basu, 2003; Bellinger et al., 2020a), as the oscillations are mostly insensitive to Y . This makes it easier to isolate the differences due to a change in \hat{u} .

Mathematically, the sensitivity of each mode frequency to a small change in the structure is expressed as:

$$\frac{\delta \hat{\nu}_i}{\hat{\nu}_i} = \int K_i^{(\hat{u}, Y)} \frac{\delta \hat{u}}{\hat{u}} dr + \int K_i^{(Y, \hat{u})} \delta Y dr + \text{higher order terms.} \quad (3.5)$$

Such an equation can be written for each mode i , where the index i of the mode again corresponds to a specific pair of n, ℓ . The relative frequency difference ($\delta \hat{\nu}_i / \hat{\nu}_i$) is related to the structure differences between the model and the observed star through the mode kernel functions K_i . These mode kernels are known functions of the reference model, found through a linear perturbation of the oscillation equations (for more details, see Gough and Thompson 1991, Kosovichev 1999, or Thompson and Christensen-Dalsgaard 2002). As we are inverting for dimensionless structure variables we need to use the difference in dimensionless frequency ($\hat{\nu}$). These differences are calculated by scaling the dimensional frequency differences by the large frequency separation, $\Delta\nu$:

$$\frac{\delta \hat{\nu}_i}{\hat{\nu}_i} \approx \frac{\Delta\nu_{\text{mod}}}{\Delta\nu_{\text{obs}}} \frac{\nu_{i,\text{obs}}}{\nu_{i,\text{mod}}} - 1. \quad (3.6)$$

This works because $\Delta\nu$ carries the same dependence on the stellar mass and radius as the frequencies. The full derivation of Equation 3.6 can be found in Appendix B2 of B24. We note that the model frequencies $\nu_{i,\text{mod}}$ in this expression have been corrected for surface effects using the two-term formulation of Ball and Gizon (2014). We also calculate $\Delta\nu_{\text{mod}}$ after applying the surface term correction.

We choose to correct for dimensional differences and surface effects when calculating the frequency differences. These effects, however, can be handled in different ways. Alternative approaches to handling dimensional differences include using a different correction

method (e.g., Roxburgh et al., 1998; Basu, 2003; Bellinger et al., 2021), including the mean density in the fitting procedure (e.g., Buldgen et al., 2022b), or adding a term to Equation 3.5 (e.g., Kosovichev and Kitiashvili, 2020). Following the arguments outlined in Appendix B2 of B24, we expect that the inversion procedure will suppress the effects of differences in mean density regardless of the correction method used. Bellinger et al. (2019a) shows this explicitly as inversions using models of different masses and radii return the same results. The surface term can also be accounted for during the inversion by adding a term to Equation 3.5 (e.g., Rabello-Soares et al., 1998; Bellinger et al., 2016; Buldgen et al., 2022b). We have tested this approach and found no difference in the final inversion results.

If the structure differences are known, then the right-hand side of Equation 3.5 can be used to calculate the corresponding frequency differences. When comparing an observed star to its best-fit model, however, we know the frequency differences and seek to infer the underlying structure differences. We accomplish this through the method of optimally localized averages (Backus and Gilbert, 1968, 1970). This constructs a linear combination of mode kernels that localizes the overall sensitivity around a single target radius, r_0 . Neglecting higher-order effects, Equation 3.5 becomes:

$$\sum_i^N c_i \frac{\delta \hat{\nu}_i}{\hat{\nu}_i} = \int \mathcal{K}_{r_0} \frac{\delta \hat{u}}{\hat{u}} dr + \int C_{r_0} \delta Y dr. \quad (3.7)$$

Here N is the total number of modes, c_i are known as the inversion coefficients, $\mathcal{K} = \sum_i^N c_i K_i^{(\hat{u}, Y)}$ is called the averaging kernel, and $C = \sum_i^N c_i K_i^{(Y, \hat{u})}$ is the cross-term kernel. When the inversion coefficients are chosen such that \mathcal{K} is localized around r_0 and normalized to 1, and the amplitude of C is small everywhere, then Equation 3.7 reduces to

$$\sum_i^N c_i \frac{\delta \hat{\nu}_i}{\hat{\nu}_i} \approx \int \mathcal{K}_{r_0} \frac{\delta \hat{u}}{\hat{u}} dr \approx \left\langle \frac{\delta \hat{u}}{\hat{u}} \right\rangle_{r_0}. \quad (3.8)$$

Thus once the inversion coefficients are known, the sum on the left-hand side provides a localized average of the difference in \hat{u} around r_0 .

To find the inversion coefficients, we used the method of multiplicative optimally localized averages (MOLA), which constructs the averaging kernel by penalizing any amplitude away from the target radius. For details on the implementation of MOLA, see Basu and Chaplin (2017, Chapter 10). In this process, we must choose two trade-off parameters: β , the cross-term suppression parameter, and μ , the error suppression parameter. We chose our parameter values using the same method as B24. Briefly, this method sets $\beta = 0$ as the choice of Y as the second variable naturally suppresses the amplitude of the cross-term kernel. We then chose a value of μ that correctly recovers the known values of $\delta \hat{u}/\hat{u}$ between our reference model and a small set of calibration models. These models came from our grid and have slightly larger values of χ_{fit}^2 than our reference model.

For each target star, we attempted to construct an averaging kernel for six target radii: $r_0/R = 0.05, 0.1, 0.15, 0.2, 0.25, 0.3$. In general, the presence of a convective core made it more difficult to localize sensitivity at target radii close to the boundary of the core, and so in most cases, the innermost target radius we report is $r_0/R = 0.15$. It is possible that frequencies derived from radial velocity measurements instead of photometric measurements could expand this range by providing more modes overall, which would help to suppress the sensitivity to the boundary of the convective core, and by providing more $l = 3$ modes which make it easier to localize averaging kernels at larger target radii. The uncertainties of our

inversion results are calculated using a Monty Carlo simulation to account for possible error correlations introduced by our corrections for the mean density and surface effect (for the specific details, see B24). We also report the FWHM of each averaging kernel as a measure of the resolution of each inversion.

For 11 stars, our models showed that the lowest-order quadrupole modes were mixed acoustic-buoyancy modes. We have found that current linear inversion techniques are not suitable for mixed modes (Buchele et al., in preparation) and hence, while we accounted for these mixed modes when fitting our models, we removed these modes from the mode set used for the structure inversions. Table 3.2 shows the stars with mixed modes present and how many quadrupole modes were excluded from our inversions.

3.4. Results

We divide our 43 stars into five categories based on their inversion results: (A) stars with no significant disagreement in the region probed by inversions, (H) stars for which all significant differences show that the model \hat{u} is too high, (L) stars for which all significant differences show the model \hat{u} is too low, (LH) stars where the model \hat{u} is too low in the center and too high in the outer points probed by the inversions, and (HL) stars where the model \hat{u} is too high in the center and too low in the outer points probed by the inversions. In Figure 3.2, we show an example of inversion results from one star in each category.

Around half (24) of the stars fall into category A. These models still show significant differences in the oscillation frequencies, even after correcting for the surface term, which suggests that the structure differences are either smaller than the observational uncertainties at the resolution given by the structure inversions or that the structure differences are at a location unable to be probed by the inversions. Of the stars showing significant disagreement, 11 are in category H, 6 are in category L, and 1 each is in category LH and HL. Using the χ_{inv}^2 parameter defined in B24, we search for correlations with a variety of model parameters and observations. In contrast to the earlier work, we find no significant correlations. One problem with the χ_{inv}^2 metric is that it only measures the significance of the inversion results, not whether the differences inferred are positive or negative. To account for this, we also look for correlations between the model parameters and $a\chi_{\text{inv}}^2$ where $a = -1(+1)$ for stars where the most significant inferred difference is negative (positive). We also find no significant correlations in this case.

For 13 stars, we find models with both convective and radiative cores in our calibration set. In general, the models of the stars that do have convective cores have small ones, implying the structure differences between the calibration models are relatively small. The distribution of the inversion results within this subsample is similar to that of the whole sample, suggesting that the differences we infer are not due to the ambiguity of whether the core is convective or radiative.

We discuss here only a few of our 43 stars, focusing on the stars that other works have also analyzed with structure inversions. The full inversion results of each star will be provided as supplementary material in the version published in the *Astrophysical Journal*.

3.4.1. KIC 6225718

The first star we discuss in detail is KIC 6225718. Our inversion results for this star are shown in Figure 3.2. We show in Figure 3.3 the frequency échelle diagram and frequency

Table 3.2: Stars with Mixed Modes Removed

KIC Number	Number of $l = 2$ modes removed
8228742	3
7940546	3
10068307	4
12317678	1
3632418	1
10162436	1
9353712	1
9414417	1
3456181	1
12069127	2
6679371	2

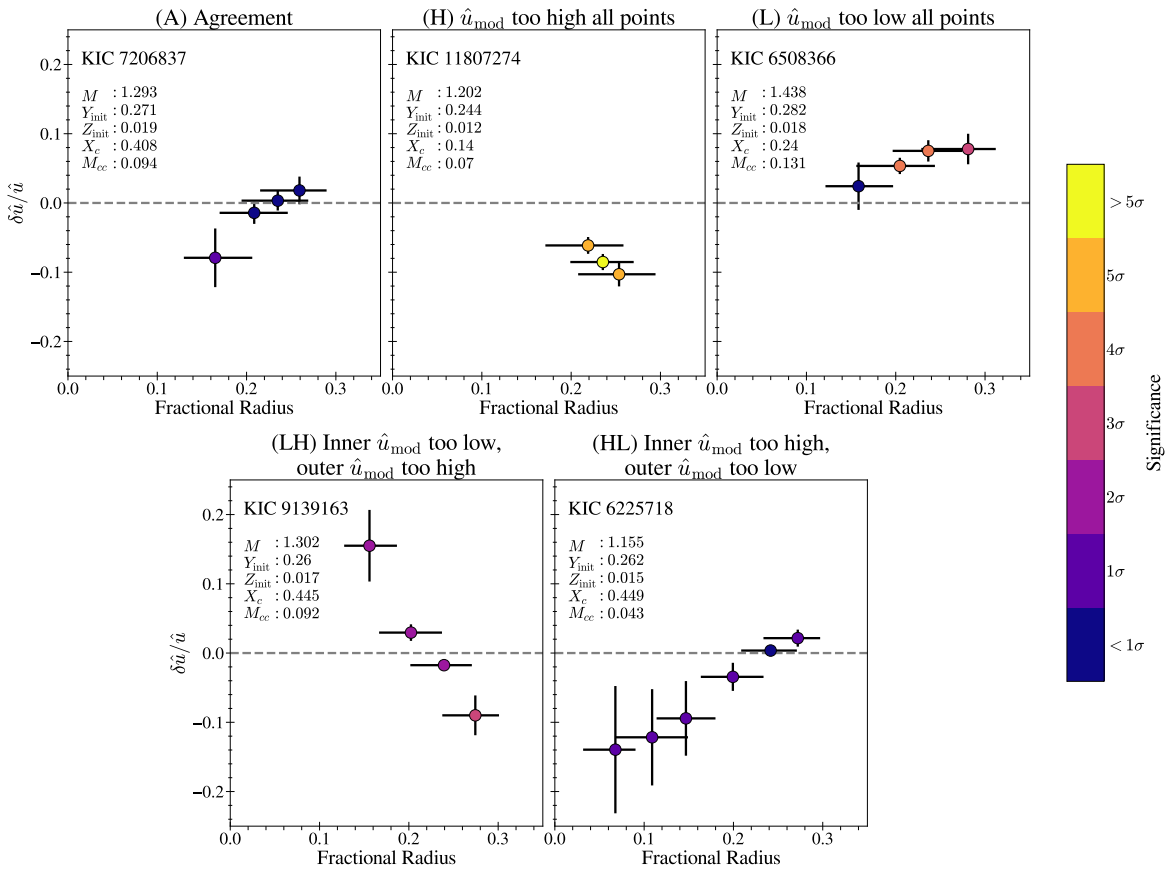


Figure 3.2: Inversion results for one star in each category. Each shows the relative differences in \hat{u} between observation and best-fit model inferred by the inversions, in the sense of $(\text{Star} - \text{Model})/\text{Model}$. The vertical error bars indicate the uncertainty of each inversion result from the propagation of the uncertainty of the observed frequencies. The horizontal error bars represent the FWHM of the averaging kernel. The dashed horizontal line indicates complete agreement between the model and observations; points above this line imply that \hat{u} of the star is larger than that of the model. The color bar indicates the statistical significance of the inferred difference, with lighter colors showing more significant results. We also provide the mass (M , in M_{\odot}), initial helium mass fraction (Y_{init}), initial metallicity (Z_{init}), central hydrogen mass fraction (X_c), and mass of the convective core (M_{cc} , in M_{\odot}) of each model.

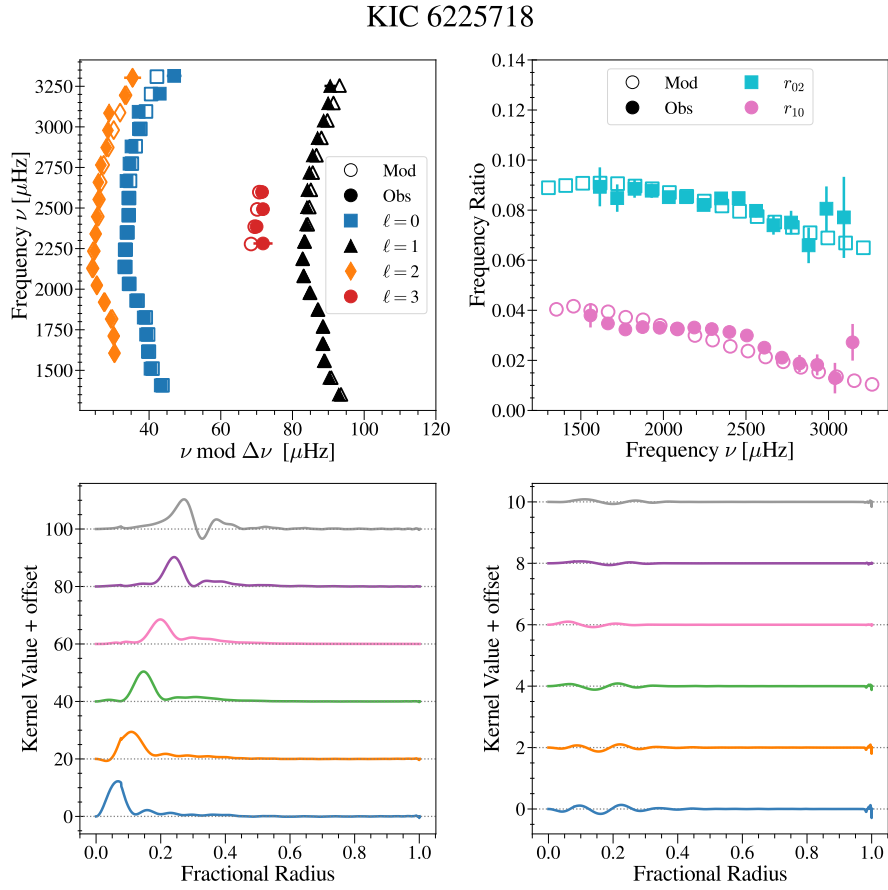


Figure 3.3: Information about the best-fit model of KIC 6225718. The top left plot shows the frequency échelle diagram comparing the frequencies of the reference model to the observations after correcting for surface effects. The top right plot shows the frequency separation ratios of the reference model and observations. The bottom left plot shows the averaging kernels and the bottom right the cross-term kernels. Note that the y -axis scale differs by an order of magnitude between the two plots on the bottom row.

separation ratios of our best-fit model, as well as, our averaging and cross-term kernels. This star has already been studied using structure inversions by Bellinger et al. (2019a) which allows us to compare our results. Structure inversions infer differences relative to a given reference model using a given set of averaging kernels. As such, any comparison of different inversion results must be considered in the context of the reference model and averaging kernels used. The averaging kernels we use are very similar to those used in Bellinger et al. (2019a). In comparing the structure of our reference model to the original model used by Bellinger et al. (2019a), we find that ours has a slightly larger convective core (with our convective boundary located at $r/R \approx 0.08$ instead of $r/R \approx 0.04$). We attribute this difference to our inclusion of core overshoot. Bellinger et al. (2019a) also constructed a model with core overshoot resulting in a convective core boundary closer to that of our reference model. However, they do not show the inversion results of this model explicitly, and instead note that the inversion results using the two different reference models are similar. Due to this, we will proceed to compare our inversion results to those reported in Bellinger et al. (2019a) for the model constructed without core overshooting.

Both works find that the model \hat{u} is too low in the outermost regions probed by inversions and too high in the innermost regions, with the crossover occurring around $r/R \approx 0.25$. Bellinger et al. (2019a) find a maximum difference at $r/R \approx 0.1$, while our maximum difference is found around $r/R \approx 0.05$. However, the higher uncertainties at these target radii mean that this difference in inversion results is not significant. Thus, despite slight differences in the fitting and inversion procedures, we find the same disagreement in internal structure.

3.4.2. KIC 10162436 and KIC 5773345

Kosovichev and Kitiashvili (2020) present inversion results for two stars that are also in our sample: KIC 10162436 and KIC 5773345. Our results for these stars are shown in Figure 3.4. Directly comparing our inversion results to theirs is slightly more difficult than with Bellinger et al. (2019a). For both stars, they find mixed modes with $l = 1$ and $l = 2$. Our model of KIC 10162436 has one mixed $l = 2$ mode, which we exclude from our inversions, and no $l = 1$ mixed mode. In the case of KIC 5773345, our model shows no mixed modes at all. In addition, the frequency differences, even of pure acoustic modes, between their models and the observations are significantly larger than ours. We attribute these differences to differences in the modeling procedure.

Kosovichev and Kitiashvili (2020) use the parameters from the YMCM modeling pipeline presented in Silva Aguirre et al. (2017), including the mixing length parameter and stellar age, to compute a model using MESA. However, the YMCM models were computed using YREC, a different stellar evolution code, and care must be taken when using best fit parameters, especially mixing length parameter and stellar age, across different codes to ensure that the implemented physics matches as closely as possible. In particular, the nuclear reaction rates and formulation of mixing length theory differ between YREC and the defaults used in MESA. It is unclear whether the authors of Kosovichev and Kitiashvili (2020) made the necessary changes to MESA to match the original YREC configuration. These differences likely explain the large frequency differences that Kosovichev and Kitiashvili (2020) find between the observed and modeled frequencies, despite the model parameters being the same. Taken together, these differences suggest that the structure of the reference models used in Kosovichev and Kitiashvili (2020) and this work are different. Additionally, while Kosovichev and Kitiashvili (2020) do not show their averaging kernels, the spread indicated

by their horizontal error bars is much wider than ours. Thus we cannot directly compare our inversion results to those given in Kosovichev and Kitiashvili (2020). Nevertheless, we note that we infer differences in \hat{u} of similar magnitude for both KIC 10162436 and KIC 5773345.

3.4.3. KIC 11807274

We now turn to the star with the most significant differences inferred by our inversions, KIC 11807274. We show in Figure 3.5 the frequency differences and frequency separation ratios for this star. Our reference model is in full agreement with the observed values of T_{eff} and $[\text{Fe}/\text{H}]$. The largest frequency differences are seen in the lower-order quadrupole frequencies, which exhibit a glitch structure not reproduced in any model. To understand how sensitive our results are to these discrepant frequencies, we repeat both our modeling and inversion procedure excluding the lowest three quadrupole modes. Our fitting procedure results in the same model as we found using the entire mode set. We show the averaging kernels and inversion results of the reduced mode set compared with the full mode set in Figure 3.5. Removing these modes results in slightly different averaging kernels, most notably for the highest target radius, where the point with maximum kernel amplitude is shifted towards the center of the star. The differences inferred with these new averaging kernels are smaller than with the full mode set, however significant differences remain.

3.4.4. Changes in Input Physics

The fact that we find significant differences in many stars suggests that the physics commonly used in stellar modeling codes may need to be modified. A full study seeking to prove the accuracy of one set of physical choices over another will require extensive modeling of all stars for which structure inversions can be used. This modeling effort should test as many changes as possible to the modeling physics and explore the effect of fitting to different observables, such as the frequency separation ratios. While we think that such work is important to continue improving stellar models, it is beyond the scope of this work. Instead, here we present a few simple tests as examples of the changes to modeling physics that could be studied with inversions. For this, we use the star where our inversions infer the most significant differences, KIC 11807274.

In Figure 3.6, we show the changes to the \hat{u} profile that result from three different changes to the physics. The first change we present is a change to core boundary mixing. Instead of calculating the overshoot using exponential overmixing, where only the composition of the overshooting region is changed, this model uses a step convective penetration (Zahn, 1991) scheme described in Appendix C.1.1, where both the composition and the temperature gradient are changed in the overshoot region. For this change, we find new model parameters from a new grid created with the changed overshooting scheme. This change results in a slightly larger convective core, which causes the spike in the relative difference around $r/R \approx 0.05$. Otherwise, the main difference in the \hat{u} profile is within the convective core, below the radius where our inversions probe. In the region where our inversions are sensitive, the change to \hat{u} is in the correct direction according to our inversion results, but it is far too small to resolve the differences. In fact, the change is smaller than the uncertainties of our inversions.

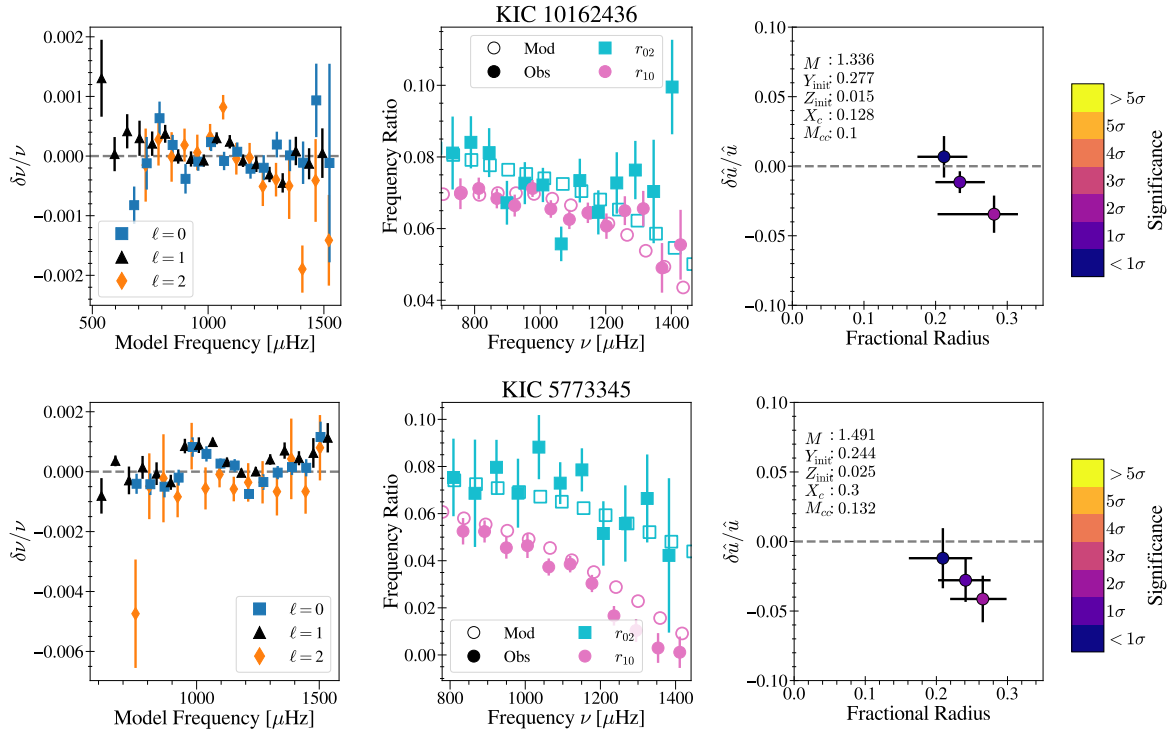


Figure 3.4: Frequency differences, frequency separation ratios, and inversion results for our models of the two stars shown in Kosovichev and Kitiashvili (2020). The top row shows the results for KIC 10162436. The figure on the left shows the relative frequency differences, after correcting for surface effects. The center panel shows the frequency separation ratios of the observed star and our reference model. The right panel shows the inversion results, where all symbols and colors have the same meaning as in Figure 3.2. The lower row shows the same information for KIC 5773345.

KIC11807274

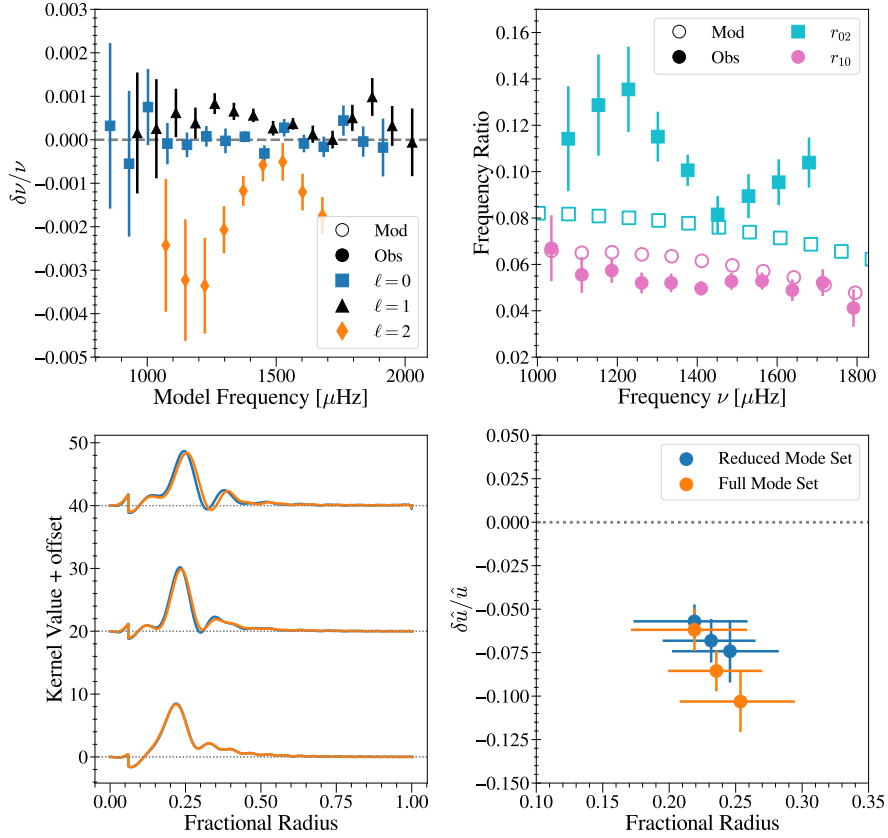


Figure 3.5: Results of the modeling and mode set testing of KIC 11807274. The first panel shows the relative frequency differences, after correcting for surface effects. The second panel shows the frequency separation ratios of the observed star and our reference model. The third panel shows the original averaging kernels and those constructed when excluding the three lowest frequencies $l = 2$ modes. The fourth panel shows the results of inversions using each mode set.

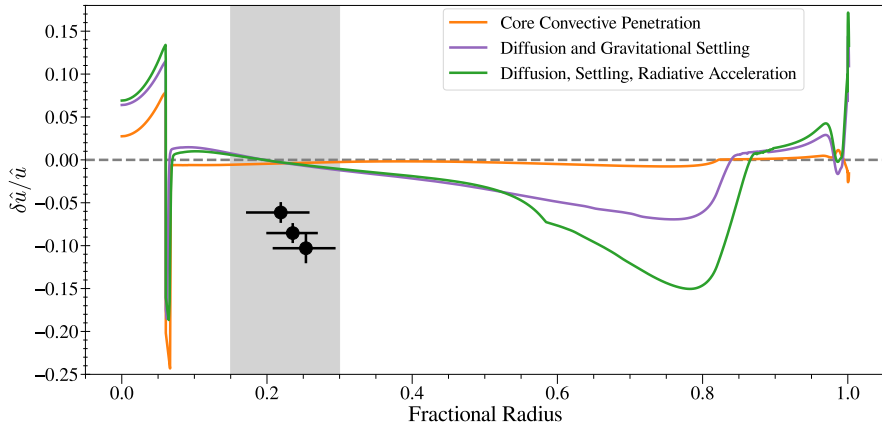


Figure 3.6: Results of varying the several mixing processes for models of KIC 11807274. Each line shows the relative difference in \hat{u} between our original reference model and a model with different physics. We indicate 0 with a dashed horizontal line and plot our inversion results for this star in black points. The vertical shading indicates the fractional radii where our inversions are sensitive. In all three cases, the spike around $r/R \approx 0.1$ is due to differences in the boundary of the convective core. The larger changes in the \hat{u} profiles around $r/R \approx 0.8$ are due to differences in the depth of the outer convection zone.

Several works (Lebreton and Goupil, 2012; Deal et al., 2023) have suggested that a large amount of convective penetration at the base of the outer convection zone may explain glitches observed in the frequency separation ratios of F-type stars. We have tested this prescription as well and found a change to the \hat{u} at the base of the convective envelope $r/R \sim 0.8$, but at the radius where our inversions are sensitive the structure is very similar to the model without this additional mixing. Hence, this change is unable to resolve the differences inferred by our inversions.

The other changes we examined deal with the transport of chemical elements. We tested the effects of including element diffusion and gravitational settling only as well as accounting for diffusion, settling, and radiative levitation. In contrast to our test of convective penetration, for both of these models we kept the same overshoot implementation and initial parameters (mass, composition, overshoot, and mixing length parameters) as our original reference model. The age of our new model is allowed to differ from the age of the original model. We choose the age along our new track which best fits the observations. In the model including only diffusion and settling we used the inlist parameters of the `diffusion_smoothness` test suite case in MESA. In the model including diffusion, settling, and radiative levitation we adopt the MESA settings of the A0 model in Campilho et al. (2022).

In both of the new models, we find the largest differences around the base of the convection zone where the transport processes have made the convection zone deeper. In the regions probed by our inversions, however, the changes are small enough to be within the uncertainties of our inversion results. Our choice to keep the initial parameters of the models constant between the different chemical mixing prescriptions represents the simplest possible test. In a full work seeking to fully resolve the inferred differences, these parameters should be inferred from a full grid as this change of physics is known to change the inferred mass, radius, and age of the star (e.g., Deal et al., 2020; Moedas et al., 2022, 2024), although how these changes affect the internal structure is not discussed in these works. For our purposes here, we seek only to provide some examples of the types of physical changes that can potentially be tested with structure inversions.

3.5. Conclusions

In this work, we have extended the analysis from Buchele et al. (2024b) (B24) to stars with convective cores. We found best-fit models from a grid of tracks computed with MESA by fitting the observed frequencies, effective temperatures, and metallicities. Using each of these best-fit models, we performed structure inversions to compare the internal structure of the model to that of the star. These results, combined with the results of B24, show that our models reproduce the internal structure of around half of the stars examined. In cases where we find significant differences, we see an even split between models with dimensionless squared isothermal sound speed that is higher than the star and cases where it is too low. In contrast to the results of the stars with radiative cores, we did not find any significant correlations with the properties of our reference models. We presented three models constructed with varying model physics as an example of the kinds of changes that could be tested in detail in future work using structure inversions. However, in our simple tests, we found that the resulting changes to the model structure are much smaller than necessary to reproduce the structure inferred by our inversions.

In both B24 and this work, the structure differences inferred by inversions remain unexplained. Particularly in light of the upcoming PLATO mission (Rauer et al., 2014, 2024), it is important to continue improving our stellar models of these types of stars. We believe that structure inversions are a key part of ensuring that future models reproduce not only the global properties of the stars but also their internal structure. To that end, in future work we plan to test potential modifications to the physical ingredients in our stellar modeling using structure inversions. With these changes, we aim to consistently improve our models of the stars with significant differences without introducing discrepancies for the stars we currently model well.

Acknowledgments The research leading to the presented results has received funding from the ERC Consolidator Grant DipolarSound (grant agreement #101000296). SB acknowledges NSF grant AST-2205026. This paper includes data collected by the Kepler mission. Funding for the Kepler mission is provided by the NASA Science Mission Directorate. In addition, this work has made use of data from the European Space Agency (ESA) mission *Gaia* (<https://www.cosmos.esa.int/gaia>), processed by the *Gaia* Data Processing and Analysis Consortium (DPAC, <https://www.cosmos.esa.int/web/gaia/dpac/consortium>). Funding for the DPAC has been provided by national institutions, in particular, the institutions participating in the *Gaia* Multilateral Agreement. We have also used the *gaia-kepler.fun* crossmatch database created by Megan Bedell.

Linearity of Structure Kernels in Main-sequence and Subgiant Solar-like Oscillators

AUTHORS Lynn Buchele, Earl P. Bellinger, Saskia Hekker, and Sarbani Basu

CHAPTER INFO This chapter is based on a paper that will be submitted in the near future. The submitted version of this paper will also include some of the introductory text of Sections 1.4. It focuses on the question of whether current structure inversion techniques can be reliably applied to stars on the subgiant branch exhibiting mixed modes. As the first author of this work, I generated the model grids and carried out the analysis myself. I was also responsible for writing the text of the paper. All co-authors provided guidance during the work and contributed comments to the manuscript.

ABSTRACT Seismic structure inversions have been used to study the solar interior for decades. With the high-precision frequencies obtained using data from the *Kepler* mission, it has now become possible to study other solar-like oscillators using structure inversions, including both main-sequence and subgiant stars. Subgiant stars are particularly interesting because they exhibit modes of mixed acoustic-buoyancy nature, which provide the opportunity to probe the deeper region of stellar cores. This work examines whether the structure inversion techniques developed for the pure acoustic modes of the Sun and other main-sequence stars are still valid for mixed modes observed in subgiant stars. We construct two grids of models: one of main-sequence stars and one of early subgiant stars. Using these grids, we examine two different parts of the inversion procedure. First, we examine what we call the “kernel errors”, which measure how well the mode sensitivity functions can recover known frequency differences between two models. Second, we test how these kernel errors affect the ability of an inversion to infer known structure differences. On the main sequence, we find that reliable structure inversion results can be obtained across the entire parameter space we consider. On the subgiant branch, however, the rapid evolution of mixed modes leads to large kernel errors and hence difficulty recovering known structure differences. Our tests show that using mixed modes to infer the structure of subgiant stars reliably will require improvements to current fitting approaches and modifications to the structure inversion techniques.

4.1. Introduction

The field of asteroseismology, i.e., the study of stars through their global oscillations, has provided unprecedented insight into stellar interiors (e.g., Aerts, 2021; Bowman and Bugnet, 2024). One of the most powerful techniques in asteroseismology is that of structure inversions. Seismic structure inversions have been used to study the solar interior for decades. Using data from *Kepler*, initial targets of asteroseismic inversions included the solar analogs 16 Cyg A and B (Bellinger et al., 2017; Buldgen et al., 2022b), a star with a small convective core (Bellinger et al., 2019a), and several more evolved stars exhibiting mixed modes (Kosovichev and Kitiashvili, 2020; Bellinger et al., 2021). The work presented in Chapters 2 and 3 increased the number of main-sequence stars (other than the Sun) studied with inversions to 55.

While this is a large improvement over the previous sample of 1 star, the Sun, this small sample size makes it difficult to draw conclusions on potential improvements to stellar modeling. Unfortunately, the requirement for the highest quality observations means that the number of stars that can be studied with these techniques will remain low until the next generation of asteroseismic missions, such as the PLATO mission (Rauer et al., 2014, 2024). Another limitation of the existing set of stars that have been studied with structure inversions is that they are restricted to a narrow range of masses and are still primarily on the main sequence. Thus, in order to truly probe stellar evolution theory, it is important to expand the types of stars that can be studied in this manner. However, care must be taken to ensure that the assumptions made in the process of such inversions hold true for stars with different structure and oscillation properties.

Here we are specifically interested in the reliability of structure inversions for subgiant branch stars. As stars run out of hydrogen and leave the main sequence, they enter a short-lived evolutionary stage known as the subgiant branch. During this phase of evolution, the core of the star contracts. This raises the buoyancy frequency in the core. At the same time, the envelope of the star expands, decreasing the frequencies of modes excited by solar-like oscillations. These two effects result in the excitation of modes with two oscillation cavities: an outer cavity where modes propagate as pressure modes (p-modes) and an inner cavity where modes propagate as buoyancy modes (g-modes). In subgiant and red giant branch stars, the region between these two cavities is small and therefore non-radial modes are able to propagate in both cavities. These modes have a mixed acoustic-buoyancy character and hence are known as mixed modes (Osaki, 1975; Deheuvels and Michel, 2011).

The degree to which any given mixed mode is predominantly acoustic or buoyant in nature changes as the star evolves. Mixed modes undergo a series of avoided crossings where the mode character is exchanged with a neighboring mode (Aizenman et al., 1977). Thus, over the course of the subgiant branch, any given mode will be alternatively p-dominated (mostly acoustic mode character) and g-dominated (mostly buoyant mode character). All mixed modes are sensitive to the structure of the core in a way that differs from the pure acoustic modes observed in main-sequence solar-like oscillators. This sensitivity makes subgiant stars an appealing target for structure inversions as mixed modes mean that structure inversions can probe deep in the core.

This increased sensitivity has been used in a few works that apply structure inversions to stars that exhibit mixed modes in their oscillation spectra. First, Kosovichev and Kitiashvili (2020) presented results for two stars which they claimed exhibited mixed modes, although this mode identification has been questioned by Buchele et al. (2024a). Then, Bellinger

et al. (2021) presented structure inversion results for HR 7322, one of the best-characterized subgiant stars observed by the *Kepler* mission (Stokholm et al., 2019; Hon et al., 2020). However, neither of these works examined in detail the reliability of structure inversions for stars exhibiting mixed modes. Due to the rapid evolution of mixed modes both in frequency and in character, it is reasonable to question the validity of the assumptions made in structure inversions in the subgiant regime. This work seeks to explore these questions by comparing the reliability of structure inversions of main-sequence solar-like oscillators with solar-like oscillators on the subgiant branch. We begin in Section 4.2 with a more detailed review of the process and assumptions of a structure inversion. Then in Section 4.3 we review the reliability of inversions while on the main sequence, before stars begin to exhibit mixed modes. Section 4.4 extends this analysis to the subgiant branch, with a particular focus on mixed dipole modes. Finally, we summarize the work and present our conclusions in Section 4.5.

4.2. Kernels and Inversions

As described in Section 1.4, the sensitivity of an oscillation mode to a linear perturbation of the structure is described by the kernel equation

$$\frac{\delta\hat{\nu}_i}{\hat{\nu}_i} = \int K_i^{(\hat{u}, Y)} \frac{\delta\hat{u}}{\hat{u}} dx + \int K_i^{(\hat{u}, Y)} \delta Y ds. \quad (4.1)$$

As the tests in this work are done by comparing two models, we calculate $\delta\hat{\nu}/\hat{\nu}$ using the known values of M and R , rather than any of the other approaches discussed in Section 1.4.

In order to extract localized information about the structure of a star, it is necessary to combine the information from all observed modes, using an optimally localized averages (OLA) method (Backus and Gilbert, 1968, 1970; Pijpers and Thompson, 1992, 1994).

A key assumption of a structure inversion is that the mode kernels, calculated using a reference model, accurately represent the sensitivity of the observed modes. This work focuses on the errors introduced by this assumption. Although we call these errors “kernel errors”, it should be noted that these are not errors in the calculation of the mode kernels, rather they are errors that result from using a mode kernel that does not accurately represent the sensitivity of an observed mode to the underlying structure. Using Equation 4.1, we define the kernel error of a mode as

$$\text{Kernel Error}_i \equiv \frac{\delta\hat{\nu}_i}{\hat{\nu}_i} - \left[\int K_i^{(\hat{u}, Y)} \frac{\delta\hat{u}}{\hat{u}} dx + \int K_i^{(Y, \hat{u})} \delta Y dx \right]. \quad (4.2)$$

Clearly, such a quantity cannot be computed for differences between an observed star and a model, and so our tests rely on comparisons between different stellar models. In each evolutionary stage we examine, we keep one model the same for all tests. We refer to this model as the reference model and denote any properties of it with the subscript ‘ref’. The second model we use we refer to as a test model, denoted with the subscript ‘test’. When computing kernel errors using Equation 4.2 written in terms of our chosen variables \hat{u} , Y , the mode kernels are those calculated using the reference model and the relative differences are defined as

$$\frac{\delta\hat{\nu}}{\hat{\nu}} = \frac{\hat{\nu}_{\text{test}} - \hat{\nu}_{\text{ref}}}{\hat{\nu}_{\text{ref}}} \quad \text{and} \quad \frac{\delta\hat{u}}{\hat{u}} = \frac{\hat{u}_{\text{test}} - \hat{u}_{\text{ref}}}{\hat{u}_{\text{ref}}} \quad \text{and} \quad \delta Y = Y_{\text{test}} - Y_{\text{ref}}. \quad (4.3)$$

In addition to examining how the kernel errors of different modes change across a grid of stellar models, we also explore how these kernel errors propagate through a full structure inversion. For this, we treat the test model as an observed star and use the reference model to perform structure inversions at several target radii. The result of these inversions can then be compared to the known structure differences between the two models. In this process, it can be helpful to also compare the inversion results to the true localized average difference,

$$\text{Localized Average Difference} \equiv \int \mathcal{K} \frac{\delta \hat{u}}{\hat{u}} dx, \quad (4.4)$$

where \mathcal{K} is the averaging kernel for a given target radius. This allows us to separate errors due to a poor averaging kernel or a large cross-term from those due to the underlying kernel errors. As structure inversions depend on the set of modes observed and their uncertainties, for each reference model we adopt a set of modes from an observed star with similar properties.

4.3. Main-Sequence Stars

Before examining the behavior of structure kernels on the subgiant branch, we first explore the kernel behavior for a star on the main sequence. For this, we constructed a grid of models using the stellar evolution code MESA (Paxton et al., 2011b, 2013b, 2015b, 2019b; Jermyn et al., 2023b). We varied only the mass and age of the models, keeping everything else (composition, mixing length, other input physics) constant. The masses we consider range from 1.05 to 1.15 M_{\odot} . For each evolutionary track, we saved models every 5×10^5 yr while the frequency of maximum power (ν_{\max} , calculated using scaling relations) was between 2520 and 2250 μHz . We then used the GYRE oscillation code (Townsend and Teitler, 2013) to calculate the adiabatic eigenfrequencies and eigenfunctions. These were in turn then used to calculate the \hat{u}, Y structure kernels.

4.3.1. Kernel Errors

In order to understand how the kernel errors vary across our grid, we take the model at the center of our grid ($M = 1.1 M_{\odot}$, $\nu_{\max} = 2205 \mu\text{Hz}$) as our reference model. For the 13 radial orders with frequencies closest to ν_{\max} , we calculate the kernel error between our reference model and every model in the grid using Equation 4.2. Figure 4.1 shows our results for the central radial order as a function of the large frequency separation $\Delta\nu$, which is a proxy for the stellar age. In this figure, the color shows the kernel error divided by $\sigma = 10^{-4}$, which corresponds to the typical uncertainty of the relative frequency differences (Davies et al., 2016; Lund et al., 2017). Here we see that a large part of the parameter space has kernel errors that are below the observational uncertainties. The largest differences occur with models that are lower in mass and lower in $\Delta\nu$ (and therefore older) than our reference model. While Figure 4.1 shows only one radial order, we obtain similar results for all 13 radial orders we explored. This is due to the pure acoustic nature of all the modes and the fact that the eigenfunctions of acoustic modes remain fairly constant across evolution and different masses.

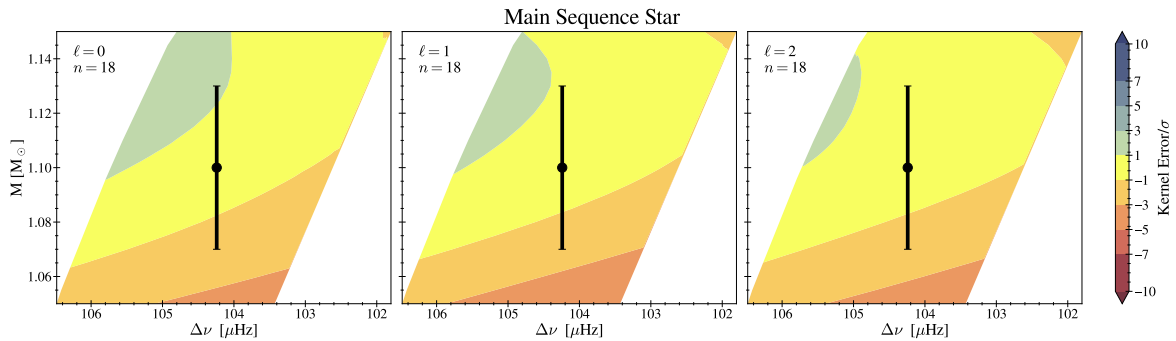


Figure 4.1: Contour plots of the kernel errors, scaled by a representative uncertainty ($\sigma = 10^{-4}$), of a main sequence star for the modes with frequencies nearest ν_{\max} . The x -axis, which shows $\Delta\nu$ as a proxy for stellar age, is reversed so that a model of a given mass evolves horizontally from left to right through the plot. The point in the center of the plot shows the location of the reference model used and the error bars represent the typical uncertainties in mass and $\Delta\nu$, taken from Lund et al. (2017). The uncertainty of $\Delta\nu$ is smaller than the point size.

4.3.2. OLA Inversions

Individual mode kernels are necessary for structure inversions, however, the final result is obtained through a linear combination of frequency differences. Thus, it is important to understand how these kernel errors propagate through an inversion. For this, we perform a set of model-model inversions using four different test models. Two test models are taken from the grid used to calculate the kernel errors, the model with the largest average kernel error (5.4σ) and one with a small average kernel error (1.3σ). For the third test model, we keep the same mass and $\Delta\nu$ but vary the initial composition such that the surface value of $[\text{Fe}/\text{H}]$ is 0.1 dex higher, which is the typical uncertainty of spectroscopic $[\text{Fe}/\text{H}]$ determinations of this type of star (e.g., Mathur et al., 2017; Furlan et al., 2018). The final test model was constructed with the same metallicity as the reference model but with the individual metal fractions scaled to the Asplund et al. (2009) abundance measurements instead of the Grevesse and Sauval (1998) scaling used in the reference model. This model also uses high-temperature opacity tables from OP (Seaton, 2005) instead of OPAL (Iglesias and Rogers, 1993, 1996). The properties of all models used in our test inversions are given in Table 4.1.

For our inversions, we adopt the observed mode set and uncertainties of 16 Cyg A from Roxburgh (2017). We use this mode set because 16 Cyg A has a similar mass and ν_{\max} as our reference model. This mode set also represents a best-case scenario due to the large number of modes observed, including $\ell = 3$ modes, and the low uncertainties of the measured frequencies. In Figure 4.2 we show the results of these test inversions as well as the frequency differences and kernel errors between our reference and test models.

In all cases, we find that our inversions perform well, with the inversion results closely matching both the true structure differences and the localized average difference. This is in line with previous work on solar inversions (Basu et al., 2000). Somewhat surprisingly, even the inversions using a test model with very high average kernel errors recover the correct differences. We attribute this to the fact that the kernel errors are roughly constant across different modes, and thus the linear combination formed during the inversion procedure acts to suppress the total error. We discuss this in more detail in Appendix D.1.

From these tests, we conclude that the range of linearity for structure inversions on the main sequence is quite broad. This is due to two factors. First, the stability of p-mode

Table 4.1: Properties of models used for main-sequence test inversions

Model	M/M_{\odot}	$\Delta\nu/\mu\text{Hz}$	[Fe/H]	X_c	Change
Reference Model	1.1	104.42	0.1	0.107	...
High Kernel Error	1.05	103.5	0.1	0.015	Different M and $\Delta\nu$
Low Kernel Error	1.093	103.23	0.1	0.065	Different M and $\Delta\nu$
Different Z	1.1	105.02	0.2	0.041	Composition
A09 Composition	1.1	104.36	0.1	0.079	Metallicity fraction and opacity table source

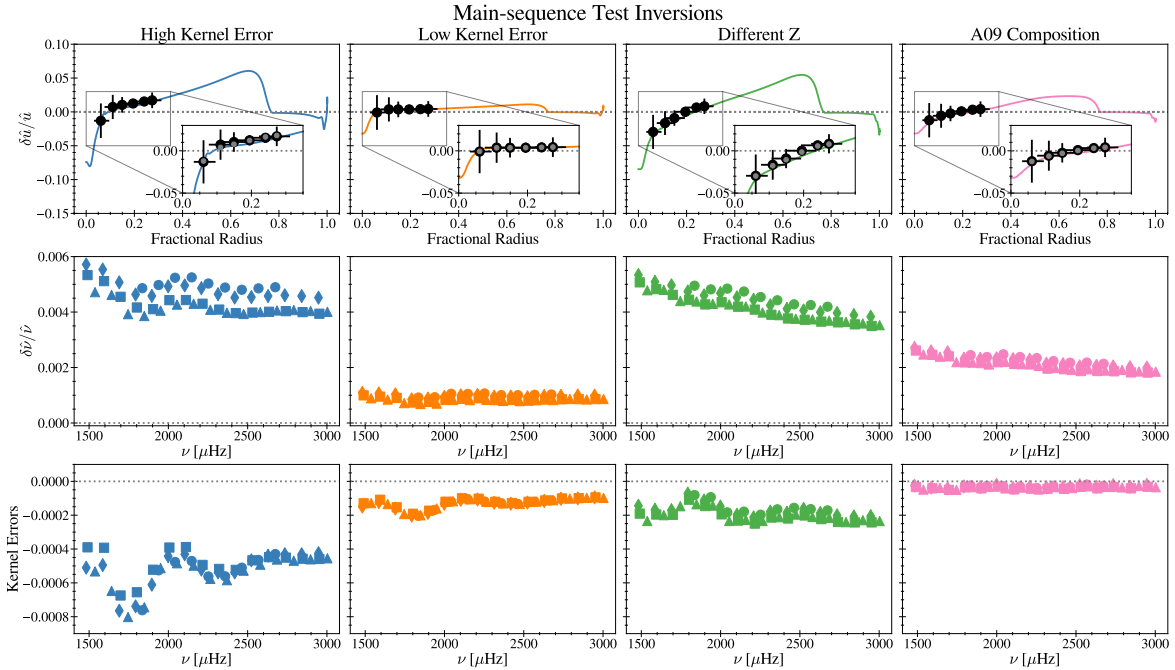


Figure 4.2: Results of several model-model test inversions. In all cases, the same reference model and inversion parameters were used, and only the test model was varied. The properties of each test model are given in Table 4.1. The first row shows the inversion results, the colored line represents the true difference in \hat{u} and the black points are the inversion results. The vertical error bars show the uncertainty calculated using Equation 1.63. The horizontal error bars represent the FWHM of the averaging kernel. The insets zoom into the region where inversions are sensitive. The insets also show the localized average difference as defined in Equation 4.4 as gray points. The second row shows the relative dimensionless frequency differences between the two models. The last row shows the kernel error of each mode. In the bottom two rows, the symbol used indicates the spherical degree of the mode with squares (triangles, diamonds, circles) representing $\ell = 0$ (1,2,3). In all cases, the inversions yield accurate inferences of the internal stellar structure, even in the case of high kernel error.

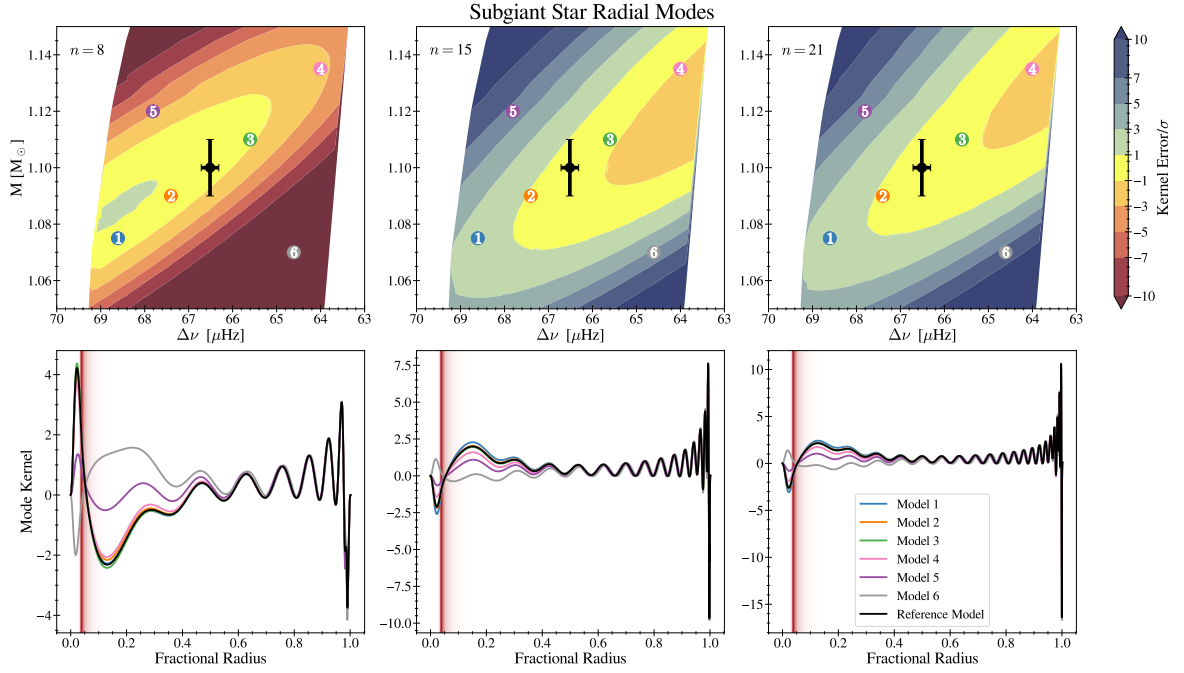


Figure 4.3: Contour plots of kernel errors for several radial modes of our subgiant grid. The reference model is indicated with a black point and the error bars correspond to the uncertainty of mass and $\Delta\nu$ of μHer given in Grundahl et al. (2017). We also show, in the bottom row, the mode kernels of our reference model and several other models, indicated in the top row with colored points and numbers. The red vertical shading indicates the strength of nuclear burning in the hydrogen-burning shell of the reference model.

kernels across varying masses, ages, and compositions means that there is a large range of the parameter space with intrinsically low kernel errors. Secondly, the kernel errors across different modes behave similarly, meaning that the overall effect of these errors is suppressed by the structure inversion procedure.

4.4. Subgiant Stars

Having established the reliability of structure inversions of main-sequence solar-like oscillators, we now turn to stars on the subgiant branch. For this we keep the same mass values as our main-sequence grid, however now we examine more evolved models with ν_{max} in the range 1282 and 1150 μHz . Again we use the model at the center of our grid (1.1 M_{\odot} , $\nu_{\text{max}} = 1216 \mu\text{Hz}$) as our reference model.

4.4.1. Kernel Errors

We repeat the same procedure to calculate the kernel errors of $\ell = 0, 1, 2, 3$ modes for 14 radial orders, centered around $\nu_{\text{max,ref}}$. In Figure 4.3, we show the results of several radial modes across different radial orders. For these modes, the regime where the kernel errors are less than our uncertainty is smaller than in the case of the main-sequence models. However, it is still large enough that fitting the mass and $\Delta\nu$ within 1σ returns a model with low kernel errors. This is unsurprising, as the radial modes are purely acoustic and so benefit from the same stability in the eigenfunctions as was seen in our main-sequence models. We do

however find slightly larger differences at the edges of our grid, particularly in the lower order modes. To better understand where these errors arise from, we also plot the mode kernels of several different models from our grid in the lower panels of Figure 4.3.

Kernel errors arise when the mode kernel of the reference model no longer approximates the mode kernel of the test model. Thus we would expect, and indeed find, that the test models with the highest kernel errors (models 5 and 6) show the greatest difference between the mode kernels of the test and reference models. There is some variation in the kernel error contours across different radial orders. Most notably, the lower-order mode shows negative kernel errors on the outer portions of the grid in contrast to the two higher-order modes. This is explained by looking at the mode kernels. The mode kernel of the lower order mode is positive below the hydrogen-burning shell and negative above it. The higher-order modes show the opposite behavior. Across all radial orders, models that are within the observational uncertainties of mass and $\Delta\nu$ show small kernel errors for the radial modes.

The situation changes dramatically for the dipole modes, shown in Figure 4.4. When discussing the behavior of mixed modes, it is useful to know the mode character, or how p- or g-dominated the mixed mode is. To visualize this, Figure 4.4 also shows the acoustic mode inertia. This quantity is defined as

$$\frac{E_p}{E} = \frac{\int_{\text{p-cavity}} [\xi^2 + \ell(\ell + 1)\eta^2] \rho r^2 dr}{\int_0^R [\xi^2 + \ell(\ell + 1)\eta^2] \rho r^2 dr}, \quad (4.5)$$

where ξ and η are the radial and horizontal components of the eigenfunction, respectively, and the integral in the numerator is evaluated only over the acoustic cavity¹. A value of E_p/E close to 1 corresponds to a mixed mode that is strongly p-dominated and, conversely, a value of E_p/E close to 0 corresponds to a mode that is strongly g-dominated. We also show, in Figure 4.4, the mode kernels of several models within the grid.

For these dipole modes, we see several different ways that the kernel errors change over the parameter space. The easiest of these to explain are the highest-order modes, which behave in a manner that is similar to the radial modes. This is expected as these modes have not yet experienced an avoided crossing at any point in the parameter space and so fully retain their acoustic character.

For the mixed dipole modes, the most important feature of the kernels is the amplitude of the two peaks in the near-core region. As a mode evolves through an avoided crossing the amplitudes of these two peaks increase as the mode becomes more g-dominated, and hence more sensitive to the core. This is why the regions of linearity lie along lines of constant acoustic inertia. At the beginning and end of the avoided crossing the mode character changes slower than in the middle, which results in narrower regions of linearity for modes that are strongly g-dominated in the reference model, i.e., $n = 10$. The sign of the kernel error depends on both the kernel amplitude and the structure differences. The kernel errors of higher degree modes ($\ell = 2, 3$) show similar behavior to the dipole modes, we discuss them in more detail in Appendix D.2. We also discuss in this appendix the singularity in the equations used to obtain the u, Y kernels noted in Bellinger et al. (2021, Appendix A).

Table 4.2: Properties of models used for subgiant test inversions

Model	M/M_{\odot}	$\Delta\nu/\mu\text{Hz}$	[Fe/H]	$\rho_c/\text{g}\cdot\text{cm}^{-3}$	Change
Reference Model	1.1	66.45	0.1	1467	...
Match Less Mixed Modes	1.091	66.47	0.1	1580	Different M and $\Delta\nu$
Match g-dominated Dipole Modes	1.101	66.55	0.1	1446	Different $\Delta\nu$
Different Z	1.1	66.37	0.12	1571	Composition

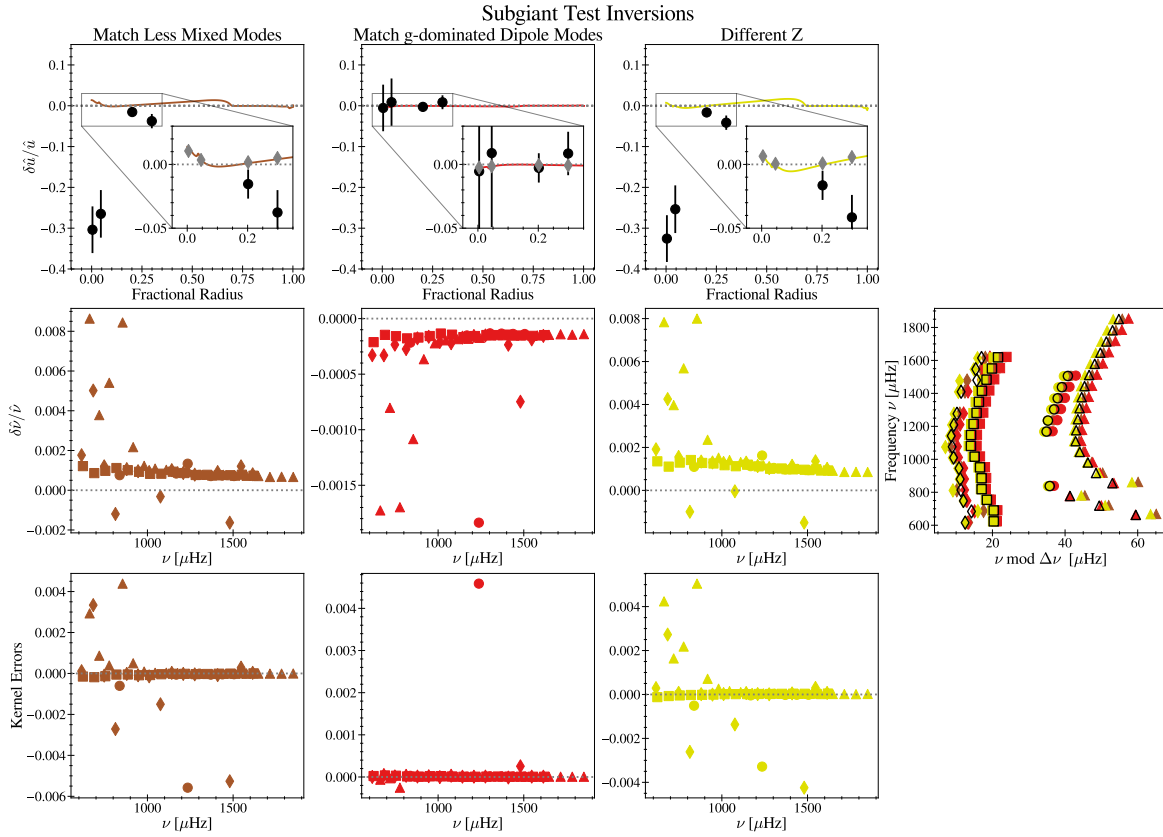


Figure 4.5: Results of several model-model test inversions for the subgiant case. In all cases, the same reference model and inversion parameters were used, and only the test model was varied. The properties of each test model are given in Table 4.2. The first row shows the inversion results, the colored line represents the true difference in \hat{u} and the black points are the inversion results. The insets zoom into the region where inversions are sensitive and also show the localized average difference as gray diamonds. The second row shows the relative dimensionless frequency differences between the two models. The last row shows the kernel error of each mode. The symbols indicate the spherical degree of the mode in the last two rows as in Figure 4.2. In the fourth column, we also show the frequency échelle diagram of all models. The reference model is plotted in open black points and the test models are shown with filled symbols according to the color used in the other columns.

4.4.2. OLA Inversions

Clearly, the magnitude and morphology of kernel errors on the subgiant branch differ significantly from that of the main-sequence cases. We now seek to explore how these errors propagate through a set of inversions. Again, we select a set of test models, whose parameters are given in Table 4.2. We show the frequency échelle diagram of all models and the results of our test inversions in Figure 4.5.

For these test models, we searched for cases where the agreement in the frequencies between our test and reference models are qualitatively similar to other best-fit subgiant models found in the literature (Noll et al., 2021; Bellinger et al., 2021; Lindsay et al., 2024). Note that the models selected as test models are not those used to show the variation of mode kernels in Figures 4.3 and 4.4.

We take two of our three test models from the grid used to calculate kernel errors. The first was chosen to resemble the quality of the fit shown in Noll et al. (2021) and Lindsay et al. (2024). This test model closely matches the radial mode frequencies, as well as many of the quadrupole and octopole modes, but has quite large differences in the mixed dipole modes. The second test model was chosen to resemble the quality of fit shown in Bellinger et al. (2021), where the frequencies of the most mixed dipole modes are matched much better than the less mixed dipole modes. The third test model was constructed with the same mass as the reference model but with a different composition. No other physics was changed and the $\Delta\nu$ value is similar to the reference model. In all cases, our test models are very close in mass ($\pm 0.01M_{\odot}$), well within the typical uncertainties of subgiant mass determinations.

For these inversions, we adopt the observed mode set and uncertainties of μ Her obtained using a recent release of SONG data (Kjelsen et al., in prep). The long observation baseline of the SONG project (Grundahl et al., 2007) results in a very large number of modes identified with very small uncertainties. Thus, as with the mode set used in our main-sequence tests, this represents the best-case scenario for structure inversions given current observations.

In one case (Match g-dominated Dipole Modes), we are able to recover the known differences within the uncertainties of the inversion. However, this represents an extremely optimistic quality of fit between the reference model and the test model. In the remaining two cases, our test inversions are unable to recover the true differences between models. This is not due to the quality of the averaging kernels as our localized averaged differences are in agreement with the known differences. In contrast to the main-sequence cases, the high kernel errors are not suppressed by the inversion. This is because the kernel errors can vary significantly between different modes, see Appendix D.1 for more details.

4.5. Conclusions

In this work, we have explored the reliability of linear structure inversions for solar-like oscillators on the main sequence and subgiant branch. Using a grid of stellar models for each evolutionary stage, we calculated the kernel errors between a reference model and each model within our grid. To understand how these kernel errors propagate through an inversion we also performed inversions between our reference model and several test models. For our main sequence models, we found that the kernel errors were low across much of the

¹This is the region of the star where $S_{\ell}^2 > \omega^2$. Where $S_{\ell} = \ell(\ell+1)c^2/r^2$ is the Lamb frequency and $\omega = 2\pi\nu$ is the angular frequency.

parameter space. Our main sequence test inversions showed that even in cases with larger kernel errors, the inversions return reliable results.

On the subgiant branch, where non-radial modes can exhibit a mixed acoustic-buoyancy nature, the picture is quite different. Here we found that the part of the parameter space where kernel errors are lower than observational uncertainties is much smaller, particularly for g-dominated mixed modes. This causes our test inversions to return erroneous values, even in cases where the global parameters (mass, $\Delta\nu$, [Fe/H]) of the test model are well within the observational uncertainties of the reference model.

As the errors in the subgiant structure inversions are primarily due to large kernel errors in a few modes (see Appendix D.1), it may be possible to perform inversions with these modes removed from the mode set and recover the correct result. However, it remains unclear how to determine the modes that should be removed based only on observations. One could consider removing modes based on the frequency difference between the model and observations, but this approach has several problems. First, the correlation between the frequency difference and the kernel error is, at best, only moderate. As an example, the Spearman correlation coefficient between the non-radial frequency differences and kernel errors of the models used in our inversion tests ranges from 0.03 to 0.5, which corresponds to a negligible to moderate correlation. The second problem is that removing modes from the mode set also removes information from the inversion, and thereby reduces the quality of the averaging kernel which can be constructed.

Future work on probing the interior structure of subgiant stars will likely require improvements to the forward modeling procedure and modifications to existing inversion techniques. On the modeling side, future model efforts should focus on developing fitting methods that prioritize matching the most g-dominated modes, as this test model provided the most reliable inversion results. Additionally, focusing on these modes specifically should lead to a better understanding of the conditions around the hydrogen-burning shell, regardless of whether these models are used for structure inversions.

At the same time, it is clearly necessary to expand asteroseismic inversion techniques beyond those originally developed to study the Sun. This need has already been noted by Vanlaer et al. (2023) who explored the application of structure inversions to stars that oscillate in pure g-modes. Several works (Giammichele et al., 2018; Farrell et al., 2024) have proposed non-linear inversions, which iteratively perturb a static model and solve the full oscillation equations, thereby including non-linear effects not accounted for in the linear variational approach explored in this work. Alternatively, the variational approach could be expanded to account for higher-order terms.

Acknowledgments The research leading to the presented results has received funding from the ERC Consolidator Grant DipolarSound (grant agreement #101000296). We thank J. Christensen-Dalsgaard for comments on the early stages of this work and for sharing a manuscript, written in collaboration with Mike Thompson, describing similar work. Additionally, we thank F. Ahlborn, V. Vanlaer, and J. Ong for productive discussions.

Conclusions and Outlook

In this section, I discuss what I have achieved with the work presented in this thesis and the next steps, particularly in the context of the upcoming PLATO mission (Rauer et al., 2014). This mission is expected to launch at the end of 2026 and will obtain light curves for more than 100,000 dwarf and subgiant stars (Rauer et al., 2024). Even if only 1% of these stars have data quality high enough to be studied with structure inversions, this is still a substantial increase of inversion targets.

5.1. Main-sequence Solar-like Oscillators

In Chapters 2 and 3, I presented structure inversion results for 55 main-sequence solar-like oscillators. These inversions represent an 11-fold increase in the number of main-sequence stars studied with structure inversions. Together, the results of these two works reveal that around half of the stars where inversions were possible showed significant structure differences between the observed star and its best-fit model. In terms of potential improvements to stellar modeling, the work presented here should be considered to be a proof-of-concept, rather than proposing any definitive conclusions. The stars studied in Chapter 2 showed a correlation between the significance of the inferred structure differences and the amount of energy generated by the CNO cycle. However, the larger sample explored in Chapter 3 showed no strong correlations between the significance of inversion results and various stellar properties. Both chapters explored several changes to the physics of the models. Unfortunately, no change that I tested resulted in structure differences that were larger than the uncertainty of the inversion results.

Drawing clearer conclusions on improving stellar models will require increasing the number of stars studied and the breadth of physical changes explored. Potential changes to the physics used in stellar modeling that could be studied with inversions include but are not limited to, improved nuclear reaction rates, updated radiative opacity values, using actual metal abundances rather than scaling the solar values, better treatment of star formation, improved descriptions of convection and convective boundaries, and including additional mixing processes such as radiative levitation or rotational mixing. Even with tests of more sophisticated physical changes, it will be difficult to draw firm conclusions based only on the 55 stars studied here. While it may be possible to increase the sample of inversion

candidates slightly using *Kepler* targets not included in Davies et al. (2016) and Lund et al. (2017), a significant increase in the number of target stars for structure inversions will need to wait for data from PLATO.

In the meantime, it is important to develop pipelines to automate the modeling and inversion procedures. For the modeling procedure, this process is already underway (Cunha et al., 2021; Gent et al., 2022). A challenge around automating structure inversions is choosing suitable inversion parameters. The parameters that form suitable averaging kernels will vary as each star has a different set of observed modes with different uncertainties, which has a significant impact on the quality of an averaging kernel given a fixed value of inversion parameters.

The method I developed to obtain inversion parameters, described in Chapter 2, is a step towards automating this procedure. However, this process still requires manual inspection of the resulting averaging kernels. This was not a problem for the approximately 100 stars I examined. As the number increases into the thousands, however, manual inspection becomes more of a problem. For inversions of global properties, there is already some work on developing automated tests of inversion quality (B  trisey et al., 2024). This work should be extended to the localized structure inversions, like those presented in this thesis.

In addition to automating the process of obtaining a stellar model and performing a structure inversion. It is also important to develop the tools necessary to interpret inversion results across a larger set of stars. Chapters 2 and 3 show a variety of shapes in the structure differences inferred by inversions. It seems inevitable that changes to the modeling physics will improve the inversion results of some stars while worsening the inversion results of other stars. Thus, care should be taken to ensure that any proposed changes consistently improve the entire sample. Additionally, when possible, these changes should be tested with other methods and for other types of stars. Due to the large number of models that must be calculated for such work, as well as the computational cost of finding a best-fit model across such a large grid, this may be a good application for machine learning techniques.

5.2. Evolved Solar-like Oscillators

The presence of mixed modes in the oscillation spectra of more evolved subgiant and red giant stars makes them an appealing target for structure inversions. Data from *Kepler* has yielded dozens of subgiant stars (Li et al., 2020) where individual mode frequencies can be identified. These mixed modes have the potential to probe deeper into the stellar core than is possible for main-sequence stars. However, it is important to verify that the assumptions made by the process of a structure inversion are still valid in this new regime. The work presented in Chapter 4 represents the first step in this process. I found that the sensitivity of the mixed modes evolves so quickly that it is difficult to trust that the mode kernels of a given model accurately represent the sensitivity of the observed modes.

Efforts should be made to develop fitting techniques that ensure that reference models match the character of the observed modes, similar to the approach presented in Ahlborn et al. (2025). At the same time, it is important to develop new inversion techniques that do not require such a close match between the star and the model. In this, there is potential synergy with ongoing work attempting to find inversion techniques suitable for g-mode pulsators, as the challenges in this field (see Vanlaer et al., 2023) resemble the challenges presented in Chapter 4.

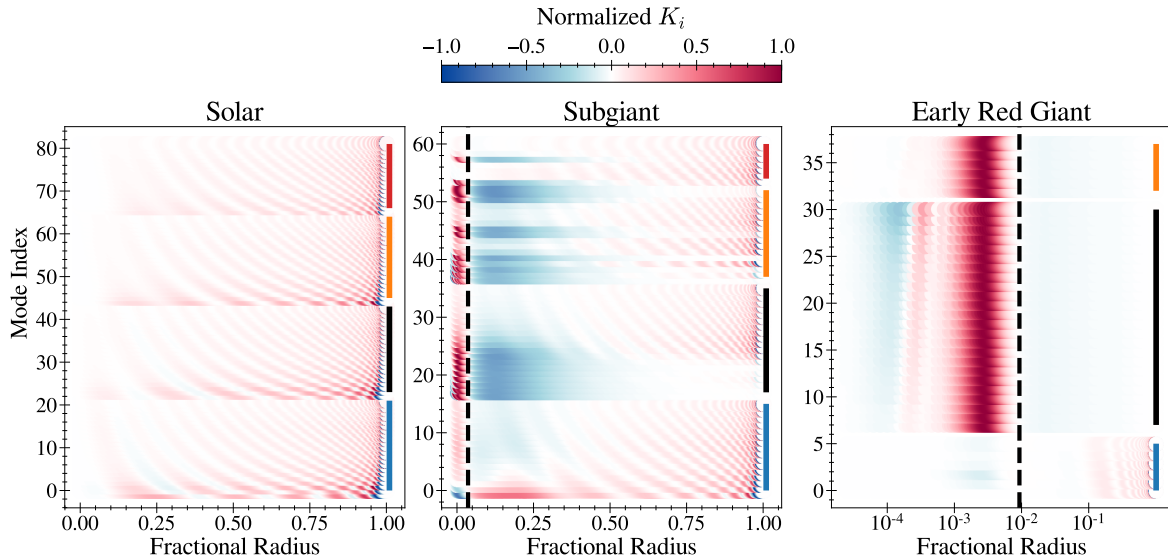


Figure 5.1: Comparison of mode kernels across different evolutionary stages. Each mode kernel is plotted along a horizontal line with the color indicating the kernel amplitude normalized by its maximum value. The colored vertical lines on the right of each panel indicate modes of spherical degree with blue (black, orange, red) indicating $\ell = 0$ (1, 2, 3), respectively. Note that the right panel is plotted with the fractional radius on a logarithmic scale to better visualize the kernel structure in the deep core. The dashed lines in the subgiant and early red giant panels indicate the point of maximum energy generation in the hydrogen-burning shell.

On the red giant branch, additional complications arise due to the many mixed modes that are expected per acoustic radial order. This increases the difficulty as one needs to ensure that the observed modes are being properly matched to the model modes and that the surface effect is being treated properly. These challenges are already present at the forward modeling stage. For structure inversions of red giants, it may also be difficult to construct well-localized averaging kernels due to the sensitivity of the observed modes. Figure 5.1 summarizes the sensitivity of expected mode sets for three different evolutionary stages. The modes from the main-sequence and subgiant models are sensitive to a variety of locations within the star. In contrast, the non-radial modes of the early red giant model are all strongly sensitive to the same fractional radius. While the radial modes are sensitive to different locations, this sensitivity is likely to be completely overwhelmed by the non-radial modes. Thus, structure inversions of red giant branch stars may require not only non-linear techniques but also a different approach to the localization of inversions.

Overall, asteroseismic structure inversions, for stars where current methods are valid, remain one of the most powerful methods of testing stellar evolution theory. This is due to the ability of structure inversions to localize and quantify disagreements between the internal structure of stars and models. Currently, the applicability of these techniques is limited to main-sequence solar-like oscillators where many individual modes were identified by the *Kepler* mission, although this sample will expand due to upcoming missions like PLATO. In terms of more evolved solar-like oscillators, the mixed modes present in their oscillation spectra present the opportunity to probe the deep core. However, fully utilizing the information from these more evolved stars will require inversion techniques that evolve beyond those used to study the Sun.



Appendix for Chapter 1: Context and Background

A.1. Derivation of Kernels

Here I provide a detailed derivation of structure kernels for three variable pairs: (c^2, ρ) , (Γ_1, ρ) , and (u, Y) . Using the time dependence of the oscillations, the perturbed equation of motion, Equation 1.22 is

$$\omega^2 \rho \xi = \nabla P' + \rho \nabla \Phi' + \rho' \nabla \Phi. \quad (\text{A.1})$$

This equation can be written in a Hilbert space as

$$\omega^2 |\xi\rangle = \mathcal{L} |\xi\rangle, \quad (\text{A.2})$$

with \mathcal{L} defined as

$$\mathcal{L} = \frac{1}{\rho} (\nabla P' + \rho \nabla \Phi' + \rho' \nabla \Phi). \quad (\text{A.3})$$

The inner product of this Hilbert space is defined as

$$\langle \eta | \xi \rangle = \int_V \rho \eta^* \cdot \xi \, d^3 \mathbf{r}. \quad (\text{A.4})$$

If the boundary conditions at the surface are $P(R) = \rho(R) = 0$, then \mathcal{L} is a Hermitian operator (Chandrasekhar, 1964) and therefore, the frequency is

$$\omega^2 \langle \xi | \xi \rangle = \langle \xi | \mathcal{L} | \xi \rangle. \quad (\text{A.5})$$

This is the oscillation equation that will be perturbed to derive the structure kernels. The structure kernels describe the response of a mode frequency to a linear perturbation in the structure, represented with δ . The perturbed form of Equation A.5 is

$$(\omega + \delta\omega)^2 (\langle \xi | \xi \rangle + \delta \langle \xi | \xi \rangle) = \langle \xi | \mathcal{L} | \xi \rangle + \langle \xi | \delta \mathcal{L} | \xi \rangle, \quad (\text{A.6})$$

where the $\delta \langle \xi | \xi \rangle$ refers to the value that results from substituting in perturbations of the form $\rho \rightarrow \rho + \delta\rho$ to all relevant structure variables: ρ, c^2, g, P, Φ' . The term $\langle \xi | \delta \mathcal{L} | \xi \rangle$ is found in the same way.

Expanding Equation A.6 and keeping only terms that are linear in the perturbation yields

$$\omega^2 \delta \langle \xi | \xi \rangle = 2\omega \delta \omega \mathcal{S} = \langle \xi | \delta \mathcal{L} | \xi \rangle, \quad (\text{A.7})$$

where

$$\mathcal{S} = \langle \xi | \xi \rangle = \int_0^R \left[\xi^2 + \ell(\ell + 1)\eta^2 \right] \rho r^2 dr. \quad (\text{A.8})$$

The end goal of this derivation is to write Equation A.6 in the following form

$$\frac{\delta \omega}{\omega} = \int K^{(f_1, f_2)} \frac{\delta f_1}{f_1} dr + \int K^{(f_2, f_1)} \frac{\delta f_2}{f_2} dr, \quad (\text{A.9})$$

where f_1 and f_2 are two variables of stellar structure and K are the kernel functions. I begin by deriving the c^2, ρ kernels.

c^2, ρ Kernels

Left-hand side

Starting with the left-hand side of Equation A.7, the first term to calculate is $\delta \langle \xi | \xi \rangle$. Using Equation A.4 and substituting in the structure perturbations yields

$$\delta \langle \xi | \xi \rangle = \int_V (\rho + \delta \rho) \xi^{*} \cdot \xi d^3 \mathbf{r} = \int_V (\rho + \delta \rho) \left[|\xi|^2 Y_{\ell m}^* Y_{\ell m} + |\eta|^2 \nabla_{\perp} Y_{\ell m}^* \nabla_{\perp} Y_{\ell m} \right] d^3 \mathbf{r}. \quad (\text{A.10})$$

Green's first identity can be used to simplify the terms involving the angular part of the gradient, ∇_{\perp} . Noting that the surface term is 0, the second term becomes

$$\int_0^R (\rho + \delta \rho) |\eta|^2 r^2 dr \int_S \nabla_{\perp} Y_{\ell m}^* \nabla_{\perp} Y_{\ell m} d\Omega = \int_0^R (\rho + \delta \rho) |\eta|^2 r^2 dr \left[- \int_S Y_{\ell m}^* \nabla^2 Y_{\ell m} d\Omega \right]. \quad (\text{A.11})$$

Since the spherical harmonics are eigenfunctions of the spherical Laplace operator this reduces to

$$\int_0^R (\rho + \delta \rho) |\eta|^2 r^2 dr \int_{\Omega} \ell(\ell + 1) |Y_{\ell m}|^2 d\Omega. \quad (\text{A.12})$$

All of the angular integration contained in the perturbed oscillation equation will reduce to $\int_{\Omega} |Y_{\ell m}|^2 d\Omega$. This reduces to the normalization constant which depends on the spherical harmonics convention being used. Here, I use the following convention $\int_{\Omega} |Y_{\ell m}|^2 d\Omega = 1$ so that Equation A.10 becomes

$$\delta \langle \xi | \xi \rangle = \int_0^R \rho (|\xi|^2 + \ell(\ell + 1)|\eta|^2) r^2 dr + \int_0^R \delta \rho (|\xi|^2 + \ell(\ell + 1)|\eta|^2) r^2 dr \quad (\text{A.13})$$

With this, the left-hand side of Equation A.7 is

$$2\omega \delta \omega \mathcal{S} + \omega^2 \underbrace{\int_0^R \delta \rho (|\xi|^2 + \ell(\ell + 1)|\eta|^2) r^2 dr}_2. \quad (\text{A.14})$$

To better track how each of these terms carries forward to the final equation for the $K^{(\rho, c^2)}$ kernel, I have numbered them based on the order they appear in the final equation.

Right-hand side

Before perturbing $\langle \xi | \mathcal{L} | \xi \rangle$ it is useful to write it in a slightly different form. Beginning first with the form derived above:

$$\langle \xi | \mathcal{L} | \xi \rangle = \int_V \xi^* \cdot (\nabla P' + \rho \nabla \Phi' + \rho' \nabla \Phi) dV. \quad (\text{A.15})$$

Using integration by parts on the first term and dropping the surface term under the assumption that $\rho(R) = 0$ gives

$$\int_V [-P' \nabla \cdot \xi^* + \xi^* \cdot \rho \nabla \Phi' + \xi^* \cdot \rho' \nabla \Phi] dV. \quad (\text{A.16})$$

Substituting in $-P' = c^2 \rho \nabla \cdot \xi + \xi \cdot \nabla P$ and using the equilibrium equation of motion, $\nabla \Phi = -\nabla P / \rho$, leads to

$$\int_V \left[c^2 \rho |\nabla \cdot \xi|^2 + (\xi \cdot \nabla P)(\nabla \cdot \xi^*) - \xi^* \cdot \frac{\rho'}{\rho} \nabla P + \xi^* \cdot \rho \nabla \Phi' \right] dV. \quad (\text{A.17})$$

The next substitution is to use $-\rho' = \nabla \cdot (\rho \xi) = \rho \nabla \cdot \xi + \xi \cdot \nabla \rho$ which gives

$$\int_V \left[c^2 \rho |\nabla \cdot \xi|^2 + (\xi \cdot \nabla P)(\nabla \cdot \xi^*) + (\nabla \cdot \xi)(\xi^* \cdot \nabla P) + \frac{1}{\rho} (\xi \cdot \nabla \rho)(\xi^* \cdot \nabla P) + \xi^* \cdot \rho \nabla \Phi' \right] dV. \quad (\text{A.18})$$

The second and third terms are complex conjugates of each other and so this expression reduces to

$$\int_V \left[\overbrace{c^2 \rho |\nabla \cdot \xi|^2}^I + \overbrace{2 \operatorname{Re}((\xi^* \cdot \nabla P)(\nabla \cdot \xi))}^{II} + \overbrace{\rho^{-1} (\xi \cdot \nabla \rho)(\xi^* \cdot \nabla P)}^{III} + \overbrace{\xi^* \cdot \rho \nabla \Phi'}^{IV} \right] dV. \quad (\text{A.19})$$

To find the perturbed form of this expression, I will discuss the perturbations of the individual terms marked by the Roman numerals separately.

Term 0 Before proceeding it is useful to evaluate one quantity that will come up repeatedly in the following discussion, the divergence $\nabla \cdot \xi$. Taking the divergence in spherical coordinates results in

$$\nabla \cdot \xi = \frac{1}{r^2} \frac{\partial}{\partial r} (r^2 \xi Y_{\ell m}) + \frac{1}{r \sin \theta} \frac{\partial}{\partial \theta} \left(\sin \theta \eta \frac{\partial}{\partial \theta} Y_{\ell m} \right) + \frac{1}{r \sin \theta} \frac{\partial}{\partial \phi} \left(\frac{\eta}{\sin \theta} \frac{\partial}{\partial \phi} Y_{\ell m} \right). \quad (\text{A.20})$$

The angular terms in the above expression can be reduced to the Laplacian of the spherical harmonics, resulting in

$$\nabla \cdot \xi = Y_{\ell m} \left[\frac{2}{r} \xi + \frac{\partial \xi}{\partial r} - \frac{\ell(\ell+1)\eta}{r} \right] = \chi Y_{\ell m}, \quad (\text{A.21})$$

where

$$\chi = \frac{2}{r} \xi + \frac{\partial \xi}{\partial r} - \frac{\ell(\ell+1)\eta}{r}. \quad (\text{A.22})$$

Term I Term I in Equation A.19 is the most straightforward to perturb,

$$\int_V c^2 \rho |\nabla \cdot \xi|^2 dV \rightarrow \int_V (\rho + \delta\rho)(c^2 + \delta c^2) |\nabla \cdot \xi|^2 dV. \quad (\text{A.23})$$

Keeping only the terms that are linear in the perturbed quantities, and integrating over the angular components yields

$$\int_0^R [\underbrace{\delta\rho c^2 \chi^2 r^2}_1 + \underbrace{\rho \delta c^2 \chi^2 r^2}_{K^{c^2, \rho}}] dr. \quad (\text{A.24})$$

The second term in this expression is the only term that will depend on δc^2 and so is the only term in the $K^{c^2, \rho}$ kernel.

Term II Turning to term II in Equation A.19,

$$\int_V 2\text{Re}((\xi^* \cdot \nabla P)(\chi Y_{\ell m})) dV. \quad (\text{A.25})$$

Evaluating the dot product, integrating over the angular components, perturbing, and keeping only linear perturbation terms results in

$$2 \int_0^R \xi \chi \frac{\partial \delta P}{\partial r} r^2 dr. \quad (\text{A.26})$$

The partial derivative in this equation can be evaluated using the by perturbing the equilibrium equation of motion:

$$\frac{\partial P}{\partial r} = -\rho g \rightarrow \frac{\partial \delta P}{\partial r} = -g \delta \rho - \rho \delta g. \quad (\text{A.27})$$

Similarly, the definition of g can be used to determine δg :

$$g = \frac{4\pi G}{r^2} \int_0^r \rho(s) s^2 ds \rightarrow \delta g = \frac{4\pi G}{r^2} \int_0^r \delta \rho(s) s^2 ds. \quad (\text{A.28})$$

Using both of these substitutions gives

$$-2 \int_0^R \xi \chi g \delta \rho r^2 dr - 8\pi G \int_{r=0}^{r=R} \left[\xi(r) \chi(r) \rho(r) \int_{s=0}^{s=r} \delta \rho(s) s^2 ds \right] dr, \quad (\text{A.29})$$

where the variable that each value is integrated as a function of, either r or s , is written out explicitly. To match the form of Equation A.9, the perturbation ($\delta\rho$) needs to be integrated over the whole star. To get this form first, the limits and order of the two integrals must be swapped. Originally they are $0 < s < r$ and $0 < r < R$ but this range is the same as $0 < s < R$ and $s < r < R$ and so the term can be rewritten as

$$\int_{s=0}^R \int_{r=s}^R \xi(r) \chi(r) \rho(r) s^2 \delta \rho(s) dr ds. \quad (\text{A.30})$$

To match the notation of the other terms in the kernel the variables of integration can be swapped so that r is the variable integrated over the whole star. This term then becomes

$$-8\pi G \int_0^R r^2 \delta \rho(r) \int_r^R \xi(s) \rho(s) \chi(s) ds dr, \quad (\text{A.31})$$

which matches the desired form of the kernel. Term II is then

$$\int_0^R \underbrace{-2\xi \chi g \delta \rho r^2 dr}_3 - \underbrace{2(4\pi G) \int_0^R \left[r^2 \delta \rho(r) \int_r^R \xi(s) \rho(s) \chi(s) ds \right] dr}_{4a}. \quad (\text{A.32})$$

Term III Using the spherical symmetry of the problem, term III of Equation A.19 becomes

$$\int_V \rho^{-1} (\xi \cdot \nabla \rho) (\xi^* \cdot \nabla P) dV = \int_V \rho^{-1} \left(\xi Y_{lm}^* \frac{\partial P}{\partial r} \right) \left(\xi Y_{lm} \frac{\partial \rho}{\partial r} \right) dV. \quad (\text{A.33})$$

Evaluating the angular integral leaves

$$\int_0^R \rho^{-1} \xi^2 \frac{\partial P}{\partial r} \frac{\partial \rho}{\partial r} r^2 dr. \quad (\text{A.34})$$

To find the perturbed form of this equation note that

$$\frac{1}{\rho + \delta\rho} \approx \frac{1}{\rho} - \frac{\delta\rho}{\rho^2}. \quad (\text{A.35})$$

Using this, the perturbed form of this equation is

$$\int_0^R \xi^2 r^2 \left(\frac{1}{\rho} \frac{\partial \delta P}{\partial r} \frac{\partial \rho}{\partial r} + \frac{1}{\rho} \frac{\partial P}{\partial r} \frac{\partial \delta \rho}{\partial r} - \frac{\delta \rho}{\rho^2} \frac{\partial P}{\partial r} \frac{\partial \rho}{\partial r} \right) dr. \quad (\text{A.36})$$

The second and third terms, together, are equivalent to $\frac{\partial P}{\partial r} \frac{\partial}{\partial r} \left(\frac{\delta \rho}{\rho} \right)$. Substituting in $\frac{\partial P}{\partial r}$ and $\frac{\partial \delta P}{\partial r}$ from Equation A.27 results in

$$\int_0^R \xi^2 r^2 \left(-\frac{\partial \rho}{\partial r} \left(g \frac{\delta \rho}{\rho} + \delta g \right) - g \rho \frac{\partial}{\partial r} \left(\frac{\delta \rho}{\rho} \right) \right) dr. \quad (\text{A.37})$$

The δg term can be treated as in Equations A.28–A.31. The two remaining terms of Equation A.37 are

$$\int_0^R \left[-\xi^2 r^2 g \frac{\delta \rho}{\rho} \frac{\partial \rho}{\partial r} - \xi^2 g \rho r^2 \frac{\partial}{\partial r} \left(\frac{\delta \rho}{\rho} \right) \right] dr. \quad (\text{A.38})$$

Using integration by parts (and again dropping the surface term) on the first term of Equation A.38 results in

$$\int_0^R \left[\rho \left(2\xi g r^2 \frac{\delta \rho}{\rho} \frac{\partial \xi}{\partial r} + 2\xi^2 r g \frac{\delta \rho}{\rho} + \xi^2 r^2 \frac{\delta \rho}{\rho} \frac{\partial g}{\partial r} + \xi^2 r^2 g \frac{\partial}{\partial r} \left(\frac{\delta \rho}{\rho} \right) \right) - \xi^2 r^2 g \rho \frac{\partial}{\partial r} \left(\frac{\delta \rho}{\rho} \right) \right] dr. \quad (\text{A.39})$$

The final two terms cancel out, leaving

$$\int_0^R \left[2\xi g \delta \rho r^2 \frac{\partial \xi}{\partial r} + \xi^2 \delta \rho \left(2r g + r^2 \frac{\partial g}{\partial r} \right) \right] dr. \quad (\text{A.40})$$

Using the definition of gravitational potential, the term in parenthesis in Equation A.40 is

$$\frac{\partial}{\partial r} (r^2 g) = \frac{\partial}{\partial r} \left(r^2 \frac{\partial}{\partial r} \Phi \right) = r^2 \nabla^2 \Phi = 4\pi r^2 G \rho. \quad (\text{A.41})$$

Putting everything together, term III of Equation A.19 is

$$\underbrace{\int_0^R 2\xi g \delta \rho r^2 \frac{\partial \xi}{\partial r} dr}_5 + \underbrace{\int_0^R \xi^2 \delta \rho 4\pi G \rho r^2 dr}_6 - \underbrace{4\pi G \int_0^R \left[\delta \rho r^2 \int_r^R \frac{\partial \rho}{\partial s} \xi^2 ds \right] dr}_{4b}. \quad (\text{A.42})$$

Term IV Beginning with term IV of Equation A.19 and integrating by parts yields,

$$\int_V \rho \xi^* \cdot \nabla \Phi' dV = - \int_V \Phi' \nabla \cdot (\rho \xi^*), \quad (\text{A.43})$$

where again the surface term is zero. The structure perturbation must be applied to both ρ and Φ' . Keeping only the linear terms results in

$$- \int_V [\delta \Phi' \nabla \cdot (\rho \xi^*) + \Phi' \nabla \cdot (\delta \rho \xi^*)] dV. \quad (\text{A.44})$$

Focusing initially on the first term of Equation A.44 and substituting in $\delta \Phi'$ found from Poisson's equation gives

$$G \int_V \int_V \frac{\nabla' \cdot (\delta \rho \xi) \nabla \cdot (\rho \xi^*)}{|\mathbf{r}' - \mathbf{x}'|} dV' dV, \quad (\text{A.45})$$

where the primed divergence and variable of integration refers to the integral necessary to find Φ' . The primed and unprimed coordinates can be swapped to give

$$G \int_V \int_V \frac{\nabla \cdot (\delta \rho \xi) \nabla' \cdot (\rho \xi^*)}{|\mathbf{r}' - \mathbf{x}|} dV dV' \quad (\text{A.46})$$

Now the integral over the primed coordinates equals Φ'^* and so the whole of Equation A.44 can be written as

$$- \int_V [\Phi'^* \nabla \cdot (\delta \rho \xi) + \Phi' \nabla \cdot (\delta \rho \xi^*)] dV. \quad (\text{A.47})$$

Because the two terms are complex conjugates of each other this term can be rewritten as

$$-2\text{Re} \left[\int_V \Phi' \nabla \cdot (\delta \rho \xi^*) dV \right]. \quad (\text{A.48})$$

Using the spherical symmetry of the problem $\Phi' = \psi' Y_{\ell m}$ where ψ' can be found using Green's functions. This term then becomes

$$-2\text{Re} \left[\int_V \psi' Y_{\ell m} \left(\delta \rho \chi Y_{\ell m}^* + \xi Y_{\ell m}^* \frac{\partial \delta \rho}{\partial r} \right) dV \right]. \quad (\text{A.49})$$

Integrating over the angular coordinates results in

$$-2 \int_0^R \psi' \left(\delta \rho \chi + \xi \frac{\partial \delta \rho}{\partial r} \right) r^2 dr. \quad (\text{A.50})$$

Integrating by parts over the second term and inserting the definition of χ yields

$$\underbrace{2 \int_0^R \delta \rho \left[\frac{\ell(\ell+1)\eta}{r} + \frac{\partial \psi'}{\partial r} \xi \right]}_7 r^2 dr. \quad (\text{A.51})$$

Complete kernel expressions

With all of the terms expressed in the correct form, Equation A.7 becomes

$$\begin{aligned}
2\omega\delta\omega\mathcal{S} + \omega^2 \int_0^R \underbrace{\delta\rho(|\xi|^2 + \ell(\ell+1)|\eta|^2)r^2}_{2} dr &= \int_0^R \underbrace{\delta\rho c^2 \chi^2 r^2}_1 + \underbrace{\rho\delta c^2 \chi^2 r^2}_{K^{c^2,\rho}} dr \\
+ \int_0^R \underbrace{-2\xi\chi g\delta\rho r^2}_{3} dr - 8\pi G \int_0^R \underbrace{\left[r^2\delta\rho(r) \int_r^R \xi(s)\rho(s)\chi(s) ds \right]}_{4a} dr \\
+ \int_0^R \left[\underbrace{2\xi g\delta\rho r^2 \frac{\partial\xi}{\partial r}}_5 + \underbrace{\xi^2\delta\rho 4\pi G\rho}_6 \right] dr & \tag{A.52} \\
- 4\pi G \int_0^R \underbrace{\left[\delta\rho r^2 \int_r^R \frac{\partial\rho}{\partial s} \xi^2 ds \right]}_{4b} dr + 2 \int_0^R \underbrace{\delta\rho \left[\frac{\ell(\ell+1)\eta}{r} + \frac{\partial\psi'}{\partial r} \xi \right] r^2}_{7} dr.
\end{aligned}$$

Combining everything into the desired form results in

$$\frac{\delta\omega}{\omega} = \int_0^R K^{c^2,\rho} \frac{\delta c^2}{c^2} + K^{\rho,c^2} \frac{\delta\rho}{\rho} dr, \tag{A.53}$$

where

$$K^{(c^2,\rho)} = \frac{1}{2\omega^2\mathcal{S}} (\rho c^2 \chi^2 r^2), \tag{A.54}$$

and

$$\begin{aligned}
K^{\rho,c^2} &= \frac{1}{2\omega^2\mathcal{S}} \left\{ \rho c^2 \chi^2 r^2 - \omega^2 \rho (|\xi|^2 + \ell(\ell+1)|\eta|^2) r^2 \right. \\
&\quad - 2\xi\chi g\rho r^2 - 4\pi G r^2 \rho \int_r^R \left(2\xi\rho\chi + \frac{\partial\rho}{\partial s} \xi^2 \right) ds \\
&\quad \left. + 2\xi g\rho r^2 \frac{\partial\xi}{\partial r} + \xi^2 4\pi G\rho^2 + 2\rho r^2 \left[\frac{\ell(\ell+1)\eta\psi'}{r} + \frac{\partial\psi'}{\partial r} \xi \right] \right\}. \tag{A.55}
\end{aligned}$$

A.1.1. Γ_1, ρ Kernels

The structure kernels of one pair of variables can be used to find kernels for other structure variable pairs. Since the frequency differences are the same regardless of the structure kernels used to find them,

$$\frac{\delta\omega}{\omega} = \int K^{(f_1, f_2)} \frac{\delta f_1}{f_1} + K^{(f_2, f_1)} \frac{\delta f_2}{f_2} dr = \int K^{(f_3, f_4)} \frac{\delta f_3}{f_3} + K^{(f_4, f_3)} \frac{\delta f_4}{f_4} dr. \quad (\text{A.56})$$

As an example, the c^2, ρ kernels derived in the previous section can be used to find the kernels for the Γ_1, ρ variable pair. Expressing c^2 in terms of the other variables

$$c^2 = \frac{\Gamma_1 P}{\rho} \rightarrow c^2 + \delta c^2 = \frac{(\Gamma_1 + \delta\Gamma_1)(P + \delta P)}{\rho + \delta\rho}. \quad (\text{A.57})$$

Using Equation A.35 and keeping only terms linear in the perturbation results in

$$\frac{\delta c^2}{c^2} = \frac{\delta\Gamma_1}{\Gamma_1} + \frac{\delta P}{P} - \frac{\delta\rho}{\rho}. \quad (\text{A.58})$$

This expression can be used to find the Γ_1, ρ kernels in terms of the c^2, ρ kernels. Equation A.56 then becomes

$$\int K^{(\Gamma_1, \rho)} \frac{\delta\Gamma_1}{\Gamma_1} + K^{(\rho, \Gamma_1)} \frac{\delta\rho}{\rho} dr = \int K^{(c^2, \rho)} \frac{\delta c^2}{c^2} + K^{(\rho, c^2)} \frac{\delta\rho}{\rho} dr. \quad (\text{A.59})$$

Using the expression found above for $\frac{\delta c^2}{c^2}$ this becomes

$$\int K^{(c^2, \rho)} \left[\frac{\delta\Gamma_1}{\Gamma_1} + \frac{\delta P}{P} - \frac{\delta\rho}{\rho} \right] + K^{(\rho, c^2)} \frac{\delta\rho}{\rho} dr = \int K^{(\Gamma_1, \rho)} \frac{\delta\Gamma_1}{\Gamma_1} + K^{(\rho, \Gamma_1)} \frac{\delta\rho}{\rho} dr. \quad (\text{A.60})$$

A relationship between $\frac{\delta P}{P}$ and $\frac{\delta\rho}{\rho}$ can be found by integrating the equation of hydrostatic support. The perturbed form of this results in

$$\frac{\delta P}{P} = \frac{1}{P} \int_r^R g\delta\rho + \rho\delta g ds = \int_{s=r}^R \frac{1}{P} \left[g\delta\rho + \frac{4\pi G\rho}{s^2} \int_{t=0}^s \delta\rho t^2 dt \right] ds, \quad (\text{A.61})$$

where the δg term is expressed in terms of $\delta\rho$ as in Equations A.28–A.31. Using this and swapping the order of integration as before, Equation A.60 becomes

$$\begin{aligned} & \int K^{(\Gamma_1, \rho)} \frac{\delta\Gamma_1}{\Gamma_1} + K^{(\rho, \Gamma_1)} \frac{\delta\rho}{\rho} dr = \\ & \int_{r=0}^R \left[K^{(\rho, c^2)} \frac{\delta\rho}{\rho} - K^{(c^2, \rho)} \frac{\delta\rho}{\rho} + g\delta\rho \int_{s=r}^R \frac{K^{(c^2, \rho)}}{P} ds + r^2\delta\rho \int_{s=r}^R \frac{4\pi G\rho}{s^2} \left(\int_{t=0}^s \frac{K^{(c^2, \rho)}}{P} dt \right) ds \right] dr. \end{aligned} \quad (\text{A.62})$$

The new kernels are then

$$K^{(\Gamma_1, \rho)} = K^{(c^2, \rho)} \quad (\text{A.63})$$

and

$$K^{(\rho, \Gamma_1)} = K^{(\rho, c^2)} - K^{(c^2, \rho)} + g\rho \int_{s=r}^R \frac{K^{(c^2, \rho)}}{P} ds + r^2\rho \int_{s=r}^R \frac{4\pi G\rho}{s^2} \left(\int_{t=0}^s \frac{K^{(c^2, \rho)}}{P} dt \right) ds. \quad (\text{A.64})$$

A.1.2. u, Y Kernels

The u, Y kernels, used throughout this thesis are derived in this section. The derivation of the u, Y kernels from the Γ_1, ρ kernels begins by noting that

$$\int K^{(\Gamma_1, \rho)} \frac{\delta \Gamma_1}{\Gamma_1} + K^{(\rho, \Gamma_1)} \frac{\delta \rho}{\rho} dr = \int K^{(u, Y)} \frac{\delta u}{u} + K^{(Y, u)} \delta Y dr. \quad (\text{A.65})$$

The helium abundance Y is related to the other structure variables through the equation of state. As Γ_1 can be expressed as a function of P, ρ, Y through the equation of state, a small change in Γ_1 can be expressed as

$$\frac{\delta \Gamma_1}{\Gamma_1} = \Gamma_{1, \rho} \frac{\delta \rho}{\rho} + \Gamma_{1, P} \frac{\delta P}{P} + \Gamma_{1, Y} \delta Y, \quad (\text{A.66})$$

where

$$\Gamma_{1, \rho} = \left(\frac{\partial \ln \Gamma_1}{\partial \ln \rho} \right)_{P, Y}, \quad \Gamma_{1, P} = \left(\frac{\partial \ln \Gamma_1}{\partial \ln P} \right)_{\rho, Y}, \quad \Gamma_{1, Y} = \left(\frac{\partial \ln \Gamma_1}{\partial Y} \right)_{\rho, P}. \quad (\text{A.67})$$

Substituting this into Equation A.65 results in

$$\int K^{(\Gamma_1, \rho)} \left(\Gamma_{1, \rho} \frac{\delta \rho}{\rho} + \Gamma_{1, P} \frac{\delta P}{P} + \Gamma_{1, Y} \delta Y \right) + K^{(\rho, \Gamma_1)} \frac{\delta \rho}{\rho} dr = \int K^{(u, Y)} \frac{\delta u}{u} + K^{(Y, u)} \delta Y dr. \quad (\text{A.68})$$

As only two terms in this equation depend on δY it is clear that

$$K^{(Y, u)} = \Gamma_{1, Y} K^{(\Gamma_1, \rho)}. \quad (\text{A.69})$$

The definition of u can be used to find an expression for $\delta P/P$,

$$u = \frac{P}{\rho} \rightarrow \frac{\delta u}{u} = \frac{\delta P}{P} - \frac{\delta \rho}{\rho} \rightarrow \frac{\delta P}{P} = \frac{\delta u}{u} + \frac{\delta \rho}{\rho}. \quad (\text{A.70})$$

From this the (and neglecting the δY term), the left hand side of Equation A.68 is

$$\int \frac{\delta \rho}{\rho} \left(\Gamma_{1, \rho} K^{(\Gamma_1, \rho)} + \Gamma_{1, P} K^{(\Gamma_1, \rho)} + K^{(\rho, \Gamma_1)} \right) + \Gamma_{1, P} K^{(\Gamma_1, \rho)} \frac{\delta u}{u} dr. \quad (\text{A.71})$$

Following the discussion in the appendix of Thompson and Christensen-Dalsgaard (2002),

$$K^{(u, Y)} = \Gamma_{1, P} K^{(\Gamma_1, \rho)} - P \frac{d}{dr} \left(\frac{\varphi}{P} \right), \quad (\text{A.72})$$

where φ is a solution of the differential equations

$$\frac{\rho}{r^2 P} \varphi = \frac{1}{4\pi G} \frac{d}{dr} \left(\frac{F}{r^2 \rho} - \frac{1}{r^2 \rho} \frac{d\varphi}{dr} \right), \quad (\text{A.73})$$

$$F = \left(\Gamma_{1, \rho} + \Gamma_{1, P} \right) K^{(\Gamma_1, \rho)} + K^{(\rho, \Gamma_1)}, \quad (\text{A.74})$$

with boundary conditions

$$\varphi(r=0) = \varphi(r=R) = 0. \quad (\text{A.75})$$

Appendices for Chapter 2: Asteroseismic Inversions for Internal Sound Speed Profiles of Main-sequence Stars with Radiative Cores

B.1. Reference Model Parameters

Table B.1 provides the non-seismic constraints that were used to find the reference models of the 12 main sequence stars with radiative cores discussed in Chapter 2. Table B.2 provides the model parameters for each reference model.

B.2. Inversion Details

Here we provide details on how we chose our inversion parameters and how we calculate the non-dimensional frequency differences used in our inversions. Additionally, we present the results of applying our modeling and inversion methods to degraded solar data.

B.2.1. Inversion Parameter Selection

For each target radius we find the value of μ that minimizes:

$$\mathcal{M} = \left\langle \left[\left(\frac{\delta \hat{u}}{\hat{u}} \right)_{\text{inv}} - \left(\frac{\delta \hat{u}}{\hat{u}} \right)_{\text{True}} \right] + \sigma_{\text{inv}} \right\rangle_{\text{set}} \quad (\text{B.1})$$

where the angle brackets denote a mean across the set of calibration models, $(\delta \hat{u}/\hat{u})_{\text{inv}}$ is the sound speed difference inferred by the inversion, $(\delta \hat{u}/\hat{u})_{\text{True}}$ is the true sound speed difference, and the uncertainty of the inversion result is $\sigma_{\text{inv}}^2 = \sum_i c_i^2 \sigma_i^2$, where σ_i is the relative uncertainty of the i th mode. This is not the uncertainty reported in our final results, as it does not account for the uncertainty correlation introduced by our surface term and mean density corrections (see Section 2.3.3). In general, the term in the square brackets dominates, as

Table B.1: Non-seismic observations

Star	T_{eff} [K]	[Fe/H]	Luminosity [L_{\odot}]
KIC 6603624	5602±100	0.29±0.1	1.241±0.018
KIC 6116048	6012±100	-0.26±0.1	1.862±0.006
KIC 4914923	5823±100	0.12±0.1	2.135±0.035
KIC 6106415	5975±100	-0.09±0.1	1.882±0.006
KIC 3656476	5664±100	0.28±0.1	1.719±0.028
16CygA	5777±100	0.01±0.1	1.563±0.005
KIC 9098294	5869±100	-0.18±0.1	1.413±0.007
KIC 8006161	5422±100	0.32±0.1	0.646±0.005
KIC 11295426	5784±100	0.04±0.1	1.62±0.01
KIC 8394589	6051±100	-0.4±0.1	1.853±0.007
16CygB	5734±100	-0.01±0.1	1.221±0.005
KIC 10963065	6100±100	-0.22±0.1	1.934±0.007

Table B.2: Reference Model Parameters

Star	$M[M_{\odot}]$	Y_{initial}	Z_{initial}	α_{mlt}	X_c	χ_{fit}^2
KIC 6603624	1.116	0.249	0.037	2.111	0.039	4.751
KIC 6116048	1.068	0.253	0.015	2.227	0.047	4.238
KIC 4914923	1.098	0.276	0.021	1.849	0.001	5.441
KIC 6106415	1.145	0.248	0.019	2.341	0.134	3.113
KIC 3656476	1.071	0.255	0.027	1.755	0.001	14.846
16CygA	1.104	0.246	0.023	2.145	0.028	4.661
KIC 9098294	1.003	0.252	0.016	2.173	0.059	4.012
KIC 11295426	1.123	0.253	0.027	1.967	0.034	3.387
KIC 8006161	1.037	0.256	0.034	2.265	0.445	2.623
KIC 8394589	1.075	0.250	0.011	2.266	0.269	3.541
16CygB	1.048	0.246	0.021	2.281	0.135	3.410
10963065	1.100	0.257	0.014	2.278	0.154	1.851

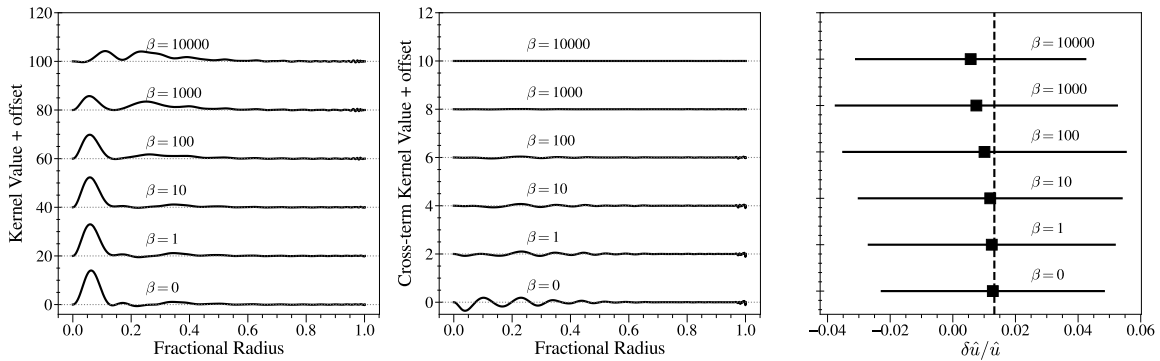


Figure B.1: Results of varying β for the innermost target radius of KIC 6603624. The left (center) panel shows the averaging kernels (cross-term kernels) that result from the indicated value of β . The right panel shows the result of a representative model-model inversion for each value of β . The true value of $\delta\hat{u}/\hat{u}$ is indicated by the vertical line. The error bars show the uncertainty of the inversion result.

with increasing values of μ the quality of the averaging kernel degrades faster than the uncertainty of the final result is reduced. We minimize \mathcal{M} separately for each target radius, and so the value of μ can vary between different target radii of the same star. This optimization is more stable when only one variable is minimized, and so we set the cross-term trade-off parameter $\beta = 0$.

As the effect of this choice is similar for all target radii across all stars in our sample, we use the innermost target radius of KIC 6603624 as an example. Figure B.1 shows the averaging kernels, cross-term kernels, and model-model inversion results for several values of β using the same value of μ . Increasing β has the expected effect of damping the cross-term kernel, however, it also reduces the quality of the averaging kernel, making it less localized. This is particularly noticeable when $\beta = 10\,000$. As the model-model inversions show, the results are much more sensitive to the quality of the averaging kernel than to the amplitude of the cross-term kernel, and so we conclude that setting $\beta = 0$ is justified.

B.2.2. Mean Density Scaling

To mitigate the effect of a difference in mean density between a star and its model, we calculate the dimensionless frequency differences before applying our structure inversions. One method of obtaining this difference was proposed in Basu (2003) and used by Bellinger et al. (2021). This approach notes that the proportional scaling with mean density shows up as a constant offset in the frequency differences. This constant offset can be approximated by taking a weighted mean of the frequency differences. This term can then be subtracted from the raw frequency differences to remove any differences due to mean density. We have found that this approximation is valid only when the frequency differences due to different mean densities are larger than the differences resulting from structure differences. Thus, in this work, we take a different approach and use the large frequency separation of the star and its reference model to calculate a dimensionless frequency difference. The dimensionless frequency is

$$\hat{\nu} = \sqrt{\frac{R^3}{GM}} \nu \quad (\text{B.2})$$

where R is the stellar radius, M is the stellar mass, and G is the gravitational constant. For two stars with stellar radii R_1, R_2 and stellar masses M_1, M_2 the dimensionless relative frequency difference of any given mode is

$$\frac{\delta\hat{\nu}}{\hat{\nu}} = \frac{\sqrt{\frac{R_1^3}{GM_1}}\nu_1 - \sqrt{\frac{R_2^3}{GM_2}}\nu_2}{\sqrt{\frac{R_2^3}{GM_2}}\nu_2} = \sqrt{\frac{R_1^3}{M_1} \frac{M_2}{R_2^3} \frac{\nu_1}{\nu_2}} - 1 \quad (\text{B.3})$$

Since $\Delta\nu \propto \sqrt{M/R^3}$,

$$\frac{\Delta\nu_2}{\Delta\nu_1} \approx \sqrt{\frac{M_2}{R_2^3} \frac{R_1^3}{M_1}}, \quad (\text{B.4})$$

with this Equation B.3 reduces to

$$\frac{\delta\hat{\nu}}{\hat{\nu}} \approx \frac{\Delta\nu_2}{\Delta\nu_1} \frac{\nu_1}{\nu_2} - 1. \quad (\text{B.5})$$

While this method results in different values for the dimensionless frequency differences, the effect on the inversion result is small compared to the uncertainty of the inversion result,

as seen for KIC 6116048 in Figure B.2. This small difference can be understood by carrying forward the effect of a small difference in mean density through the inversion procedure.

A difference in mean density shows up as a constant offset when calculating the dimensionless frequency differences. Mathematically, this is expressed as

$$\frac{\delta \hat{\nu}_i}{\hat{\nu}_i} = \frac{\delta \nu_i}{\nu_i} + \frac{\delta q}{q}, \quad (\text{B.6})$$

where $\delta q/q$ is the offset introduced by a difference in mean density. As $\delta q/q$ is independent of the frequencies, its contribution to the final inversion result will be

$$\left(\sum c_i \right) \frac{\delta q}{q}. \quad (\text{B.7})$$

Thus, the error introduced by a mismatch in mean density is proportional to the sum of the inversion coefficients for each target radius. We do not explicitly try to minimize this sum; however, the uncertainty of each result, which we do attempt to minimize, depends on the magnitude of the inversion coefficients. Thus, in the process of a standard inversion, we reduce the effect of a difference in mean density.

Equation B.7 also suggests a check to determine if a difference in mean density is the dominant difference present in our inversion results. While the sum of the coefficients will be different for each target radius, $\delta q/q$ will be the same. Thus, if the mean density differences dominate the inversion results, a plot of the inversion results at each target radius divided by the sum of the coefficients for that target radius should be a straight line. We checked this for all the stars in our sample and did not find such a constant, so we conclude that the error introduced by a difference in the mean density is not the dominant source of difference in our inversion results.

B.2.3. Sun as a star

In addition to the twelve target stars, we also obtain a reference model and structure inversion results using solar data that have been degraded to the level that was expected of results from *Kepler* (for details, see Lund et al., 2017). Table B.3 lists the parameters of the reference model obtained with these data. The parameters of our model are comparable to those found across all the pipelines used in Lund et al. (2017). To assess the quality of the fit in \hat{u} , we compare the \hat{u} profile of our reference model to that of the calibrated standard solar model S of Christensen-Dalsgaard et al. (1996), shown in Figure B.3. Although we are not able to reproduce the full structure of a model calibrated with all the solar data, our reference model is a close match in the area probed by structure inversions using only low-degree modes. These differences are of the same order of magnitude as the differences inferred between model S and the Sun (Basu et al., 2009). Thus, despite the limitations of the degraded data, we find a reference model sufficiently close for structure inversions.

Using this reference model, we obtain suitable averaging kernels at four target radii and infer the difference in \hat{u} using the degraded solar frequencies as shown by Figure B.3. At all four target radii, our structure inversions show agreement within 1σ in \hat{u} . Helioseismic inversions that use non-degraded solar data do show differences between the structure of the Sun and the structure of calibrated solar models (e.g., Basu, 2016); however, this results from using many more modes, with higher precision and at higher angular degrees, than are available for stars observed by *Kepler*.

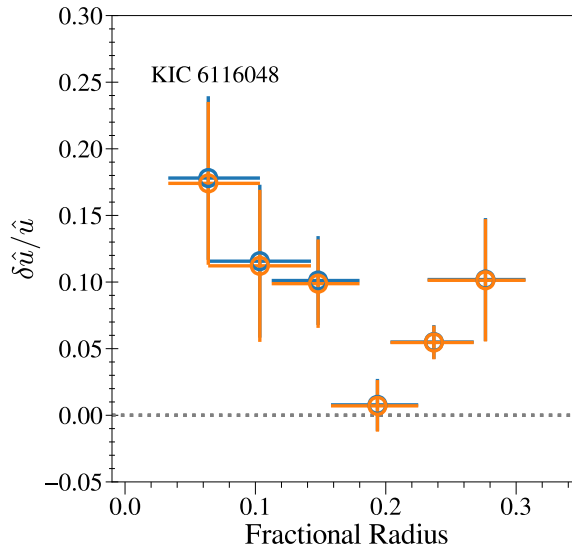


Figure B.2: Inversion results for KIC 6116048 found using two different methods of calculating the dimensionless frequency differences. The blue points show the results when frequencies are scaled using the large frequency separations, described in Section 2.3, and the orange points use the differences calculated from a weighted mean, described in Basu (2003).

Table B.3: Reference Model using Degraded Solar Data

Parameter	Unit	Value
M	$[M_{\odot}]$	1.001
Y_{initial}	...	0.282
Z_{initial}	...	0.021
L	$[L_{\odot}]$	1.057
T_{eff}	[K]	5849
R	$[R_{\odot}]$	1.001
[Fe/H]	...	0.051

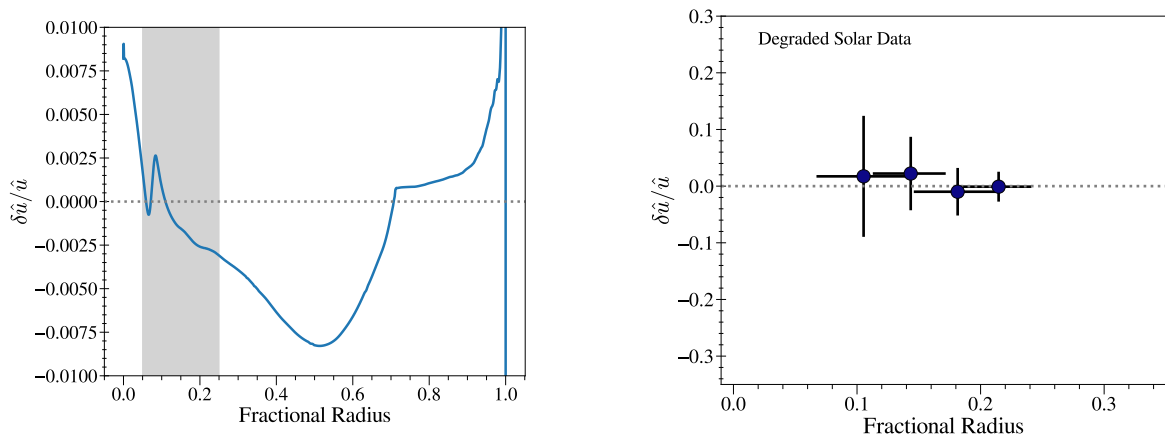


Figure B.3: Left: Relative difference in \hat{u} between our reference model, calculated from degraded solar data, and the calibrated solar model S Christensen-Dalsgaard et al. (1996). The shaded region shows the area that can be probed by structure inversions using only the reduced mode set of the degraded frequency data. Right: Inversion results of the degraded solar data. All symbols and colors have the same meaning as in Figure 2.1.

B.3. Full Inversion Results

For each target star, we attempt a structure inversion at target radii of

$$r_0/R = 0.05, 0.10, 0.15, 0.20, 0.25, 0.30.$$

The target radius, however, is not necessarily the fractional radius where the averaging kernel is at its maximum value. We report the location of the maximum and FWHM of each averaging kernel and the \hat{u} values inferred at each target radius of each star in Table B.4. Figures B.4 and B.5 show the averaging and cross-term kernels for these stars, respectively. We show in Figure B.6 the results of model-model inversions between our reference model and one of the calibration models, as a test of the averaging kernel's ability to recover a known difference.

Table B.4: Location of the averaging kernel maximum (in fractional radius) and the corresponding FWHM and the inferred dimensionless squared isothermal sound speed \hat{u} , for each target radii $r_0/R = 0.05, 0.10, 0.15, 0.20, 0.25, 0.30$

Star	$r_{\max}(0.05)$	$\hat{u}(0.05)/10^{-8}$	$r_{\max}(0.10)$	$\hat{u}(0.10)/10^{-8}$	$r_{\max}(0.15)$	$\hat{u}(0.15)/10^{-8}$
KIC 6603624	$0.062^{+0.033}_{-0.030}$	6.311 ± 0.199	$0.102^{+0.040}_{-0.040}$	6.167 ± 0.138	$0.142^{+0.033}_{-0.037}$	5.503 ± 0.126
KIC 6116048	$0.064^{+0.040}_{-0.031}$	7.660 ± 0.399	$0.103^{+0.039}_{-0.040}$	7.151 ± 0.368	$0.148^{+0.032}_{-0.036}$	6.270 ± 0.190
KIC 4914923	$0.122^{+0.039}_{-0.040}$	6.922 ± 0.381	$0.151^{+0.038}_{-0.041}$	6.042 ± 0.226
KIC 6106415	$0.060^{+0.035}_{-0.030}$	6.805 ± 0.423	$0.104^{+0.036}_{-0.038}$	6.590 ± 0.338	$0.144^{+0.035}_{-0.035}$	5.612 ± 0.194
KIC 3656476	$0.058^{+0.102}_{-0.035}$	5.755 ± 0.404	$0.116^{+0.038}_{-0.045}$	5.721 ± 0.389	$0.147^{+0.036}_{-0.040}$	5.395 ± 0.195
16CygA	$0.059^{+0.040}_{-0.032}$	6.205 ± 0.147	$0.107^{+0.035}_{-0.039}$	6.180 ± 0.115	$0.146^{+0.038}_{-0.037}$	5.583 ± 0.058
KIC 9098294	$0.068^{+0.027}_{-0.025}$	5.242 ± 1.084	$0.079^{+0.045}_{-0.027}$	5.513 ± 0.810	$0.154^{+0.030}_{-0.035}$	5.172 ± 0.509
KIC 8006161	$0.052^{+0.027}_{-0.026}$	5.354 ± 0.436	$0.093^{+0.030}_{-0.033}$	5.223 ± 0.393	$0.133^{+0.028}_{-0.031}$	5.025 ± 0.275
KIC 11295426	$0.082^{+0.051}_{-0.033}$	6.085 ± 0.559	$0.150^{+0.032}_{-0.039}$	5.391 ± 0.308
KIC 8394589	$0.134^{+0.041}_{-0.053}$	5.063 ± 0.858	$0.158^{+0.039}_{-0.032}$	4.984 ± 0.502
16CygB	$0.059^{+0.037}_{-0.031}$	5.660 ± 0.125	$0.109^{+0.034}_{-0.036}$	5.711 ± 0.089	$0.144^{+0.038}_{-0.036}$	5.347 ± 0.053
KIC 10963065	$0.063^{+0.029}_{-0.028}$	6.220 ± 1.094	$0.099^{+0.061}_{-0.044}$	6.184 ± 0.698	$0.151^{+0.030}_{-0.034}$	5.570 ± 0.417

Star	$r_{\max}(0.20)$	$\hat{u}(0.20)/10^{-8}$	$r_{\max}(0.25)$	$\hat{u}(0.25)/10^{-8}$	$r_{\max}(0.30)$	$\hat{u}(0.30)/10^{-8}$
KIC 6603624	$0.187^{+0.033}_{-0.042}$	4.772 ± 0.088	$0.237^{+0.032}_{-0.038}$	4.127 ± 0.055	$0.259^{+0.032}_{-0.042}$	3.893 ± 0.077
KIC 6116048	$0.194^{+0.031}_{-0.036}$	4.857 ± 0.094	$0.237^{+0.031}_{-0.033}$	4.316 ± 0.052	$0.276^{+0.031}_{-0.044}$	3.913 ± 0.164
KIC 4914923	$0.198^{+0.035}_{-0.040}$	4.930 ± 0.119	$0.236^{+0.034}_{-0.035}$	4.273 ± 0.049	$0.269^{+0.034}_{-0.053}$	3.870 ± 0.130
KIC 6106415	$0.194^{+0.032}_{-0.036}$	4.759 ± 0.087	$0.235^{+0.030}_{-0.033}$	4.185 ± 0.057	$0.259^{+0.029}_{-0.043}$	3.890 ± 0.063
KIC 3656476	$0.194^{+0.040}_{-0.054}$	4.696 ± 0.132	$0.235^{+0.032}_{-0.035}$	4.055 ± 0.080	$0.249^{+0.042}_{-0.040}$	3.846 ± 0.093
16CygA	$0.193^{+0.031}_{-0.037}$	4.761 ± 0.035	$0.238^{+0.034}_{-0.036}$	4.082 ± 0.028	$0.267^{+0.029}_{-0.040}$	3.700 ± 0.032
KIC 9098294	$0.189^{+0.078}_{-0.046}$	4.569 ± 0.265	$0.233^{+0.032}_{-0.042}$	3.658 ± 0.232
KIC 8006161	$0.180^{+0.026}_{-0.031}$	4.399 ± 0.141	$0.232^{+0.037}_{-0.042}$	3.791 ± 0.160	$0.258^{+0.031}_{-0.043}$	3.496 ± 0.174
KIC 11295426	$0.215^{+0.053}_{-0.065}$	4.435 ± 0.147	$0.235^{+0.031}_{-0.036}$	4.217 ± 0.107	$0.246^{+0.033}_{-0.040}$	4.066 ± 0.109
KIC 8394589	$0.213^{+0.039}_{-0.039}$	4.308 ± 0.127	$0.238^{+0.031}_{-0.035}$	4.003 ± 0.070	$0.262^{+0.029}_{-0.040}$	3.669 ± 0.063
16CygB	$0.193^{+0.030}_{-0.038}$	4.633 ± 0.031	$0.234^{+0.031}_{-0.035}$	4.028 ± 0.022	$0.258^{+0.029}_{-0.040}$	3.732 ± 0.023
KIC 10963065	$0.211^{+0.043}_{-0.048}$	4.437 ± 0.138	$0.236^{+0.031}_{-0.035}$	4.112 ± 0.079	$0.258^{+0.028}_{-0.042}$	3.718 ± 0.110



Figure B.4: Averaging kernels \mathcal{K} for each of the target stars in our sample. For readability, the averaging kernels are offset, with a horizontal dotted line indicating the zero line for each kernel.

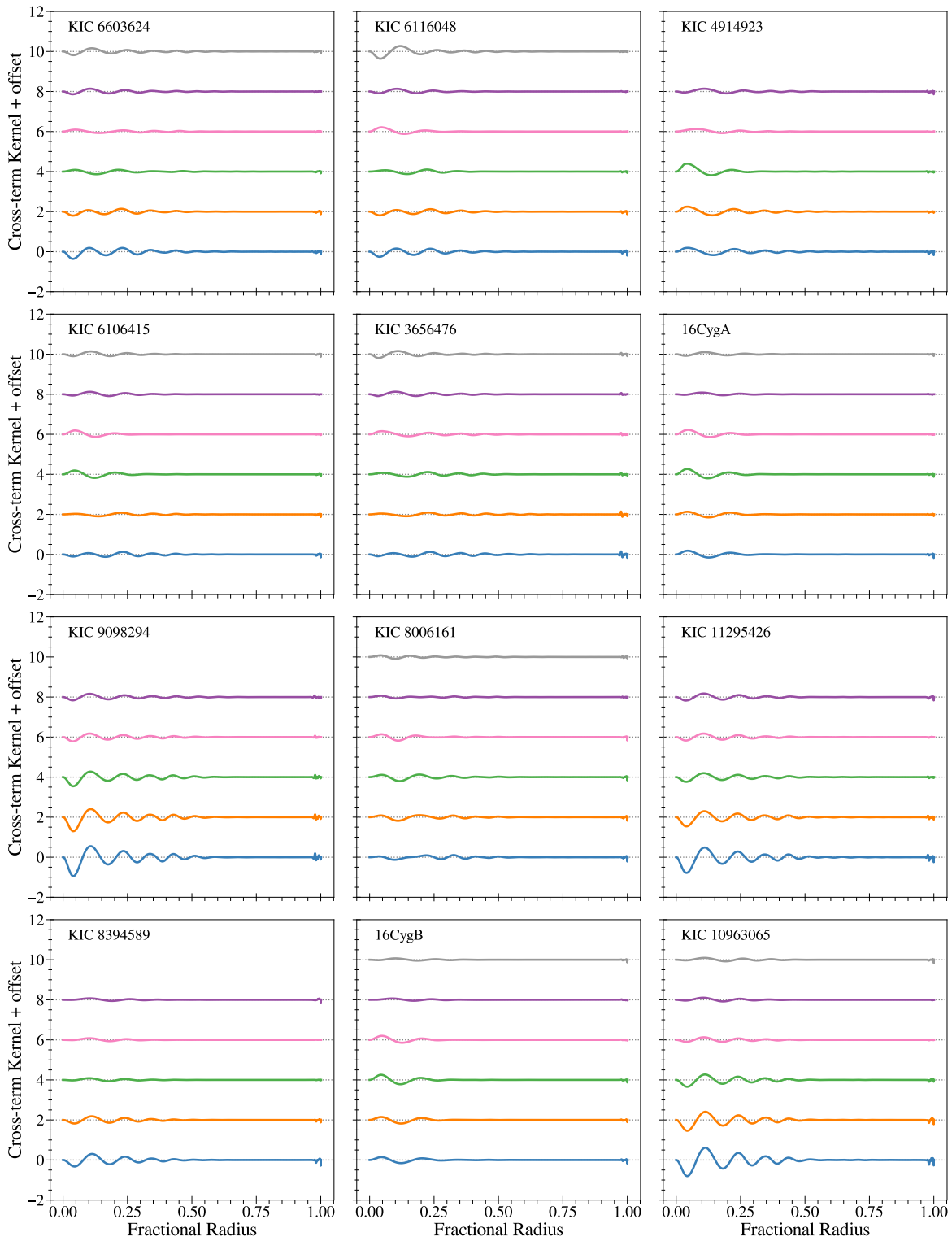


Figure B.5: Cross-term kernels C for each of the target stars in our sample. As with Figure B.4, the kernels are offset for readability. Note that the y-axis scales differs from Figure B.4.

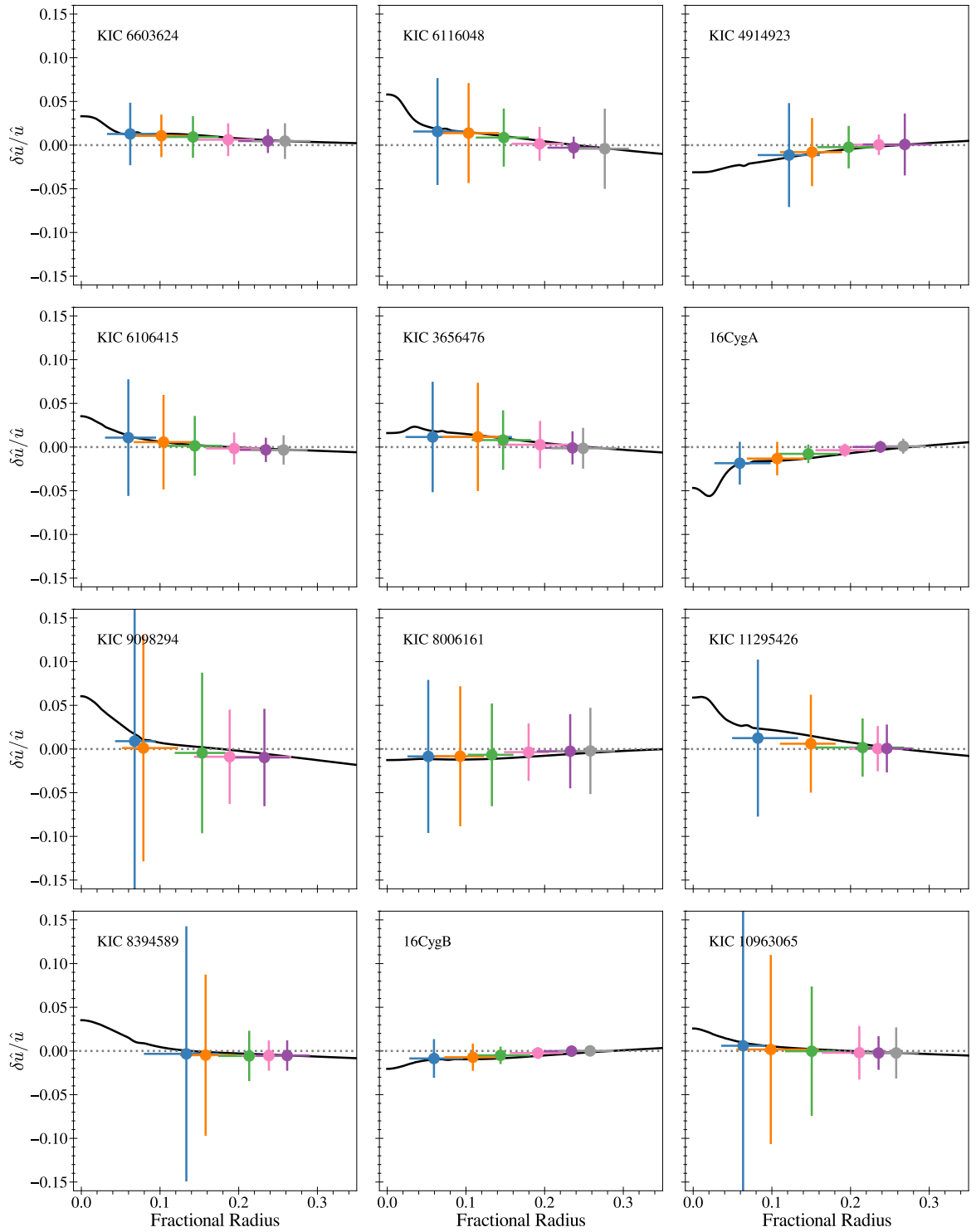


Figure B.6: Results of using the averaging and cross term kernels shown in Figures B.4 and B.5 to recover the difference between the reference model and one of the additional models used to calibrate our inversion parameters. The black line indicates the true $\delta\hat{u}/\hat{u}$ between the two models. The color of each point matches its corresponding averaging and cross-term kernels in Figures B.4 and B.5.



Appendices for Chapter 3: Asteroseismic Structure Inversions of Main-Sequence Solar-like Oscillators with Convective Cores

C.1. Appendix Modeling Details

C.1.1. Model Grids

Here, we provide more details about the grid used to find our reference models for Chapter 3. We use metal abundances scaled to the GS98 solar composition (Grevesse and Sauval, 1998), and the corresponding high-temperature opacity tables from OPAL (Iglesias and Rogers, 1993, 1996), and low-temperature opacity tables from Ferguson et al. (2005). We blend the equation of state data from OPAL (Rogers and Nayfonov, 2002), SCVH (Saumon et al., 1995), FreeEOS (Irwin, 2004), and Skye (Jermyn et al., 2021) with the default settings. This blending is described in more detail in Jermyn et al. (2022). Our nuclear reaction network is `pp_cno_extras_o18_ne22.net` and we use reaction rates from JINA REACLIB (Cyburt et al., 2010) and NACRE (Angulo et al., 1999), with additional tabulated weak reaction rates (Fuller et al., 1985; Oda et al., 1994; Langanke and Martínez-Pinedo, 2000). Electron screening is included via the prescription of Chugunov et al. (2007). Thermal neutrino loss rates are from Itoh et al. (1996). We use the time-dependent local convection formalism of Kuhfuss (1986), which, as described in Jermyn et al. (2022), reverts in the limit of long time steps to standard mixing length theory as described in Cox and Giuli (1968). We use an Eddington-gray atmosphere and include the structure of the atmosphere out to an optical depth of $\tau = 10^{-3}$ when calculating both our oscillation frequencies and structure kernels.

C.1.1.1 Convective Penetration

As MESA does not implement convective penetration by default, we make use of the `other_after_set_mixing_info` hook in `run_star_extras`. This allows us to use MESA's

procedure for calculating the extent of step overshooting region and simply change the temperature gradient after these regions have been identified. It also simplifies the process of including overshoot from the convective core and at the base of the outer convection zone.

C.1.2. Modeling Information

In Table C.1, we provide the non-seismic constraints used in our modeling procedure. For all but three stars, we take our spectroscopic measurements from Furlan et al. (2018, , Table 9) and adopt their suggested uncertainties of 100K and 0.1 dex for T_{eff} and $[\text{Fe}/\text{H}]$, respectively. Two of our stars, KIC 434952 and KIC 5773345, are not analyzed by Furlan et al. (2018). In these cases, we use the values from Mathur et al. (2017). The values in Furlan et al. (2018) for KIC 9965715 were found to be discrepant from other literature values, so instead we use the measurements from Morel et al. (2021). To reduce the computation time when finding a best-fit model, we calculate χ_{fit}^2 only for models within 6σ of the observed effective temperature and metallicity and 10σ of the observed luminosity. We primarily use the FLAME luminosity value from Gaia DR3 (Gaia Collaboration et al., 2016; Creevey et al., 2023), although some stars are only available in Gaia DR2 (Gaia Collaboration et al., 2018), or not at all.

Table C.2 provides the parameters of our reference model for each star and the star’s category based on our inversion results as defined in Section 3.4. To compare the quality of our fits, we obtain the surface-term corrected frequencies of the best fitting models found using the YMCM pipeline of Silva Aguirre et al. (2015, 2017). We obtained results for a set of models constructed both with and without diffusion. In Figure C.1, we plot the distributions of χ_{fit}^2 values for the YMCM models with and without diffusion and the reference models used for our inversions. We find that our overall distribution is similar, with fewer outliers resulting from our modeling procedure.

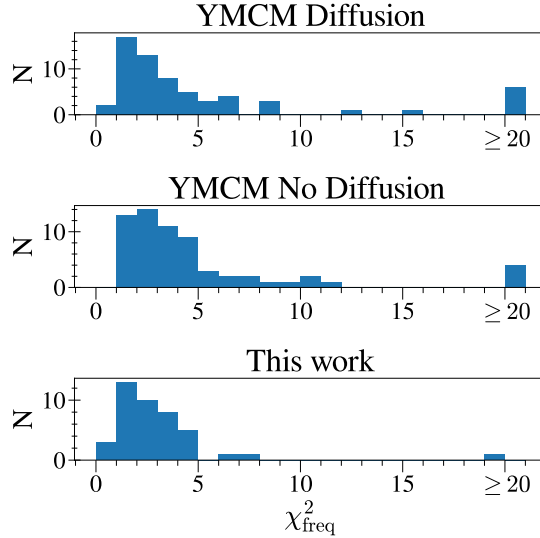


Figure C.1: Distribution of χ_{fit}^2 , as defined in Equation 3.3 for models fit using the YMCM pipeline of Silva Aguirre et al. (2015, 2017) and constructed with and without diffusion, as well as, the χ_{fit}^2 distribution of the models used in this work. Models with $\chi_{\text{fit}}^2 \geq 20$ have been collapsed into the final bin.

Additionally, we compare our stellar parameters to those reported from all the pipelines in Silva Aguirre et al. (2017) in Figure C.2. In general, our values of mass and radius fall within the spread of values in Silva Aguirre et al. (2017) without any clear biases. This is in contrast to the composition of our models which show a clear bias in favor of higher initial hydrogen mass fraction and lower initial helium mass fraction. We attribute this to our choice not to include diffusion in our models. Despite this bias, our values are still within the range of values predicted by the various pipelines used in Silva Aguirre et al. (2017).

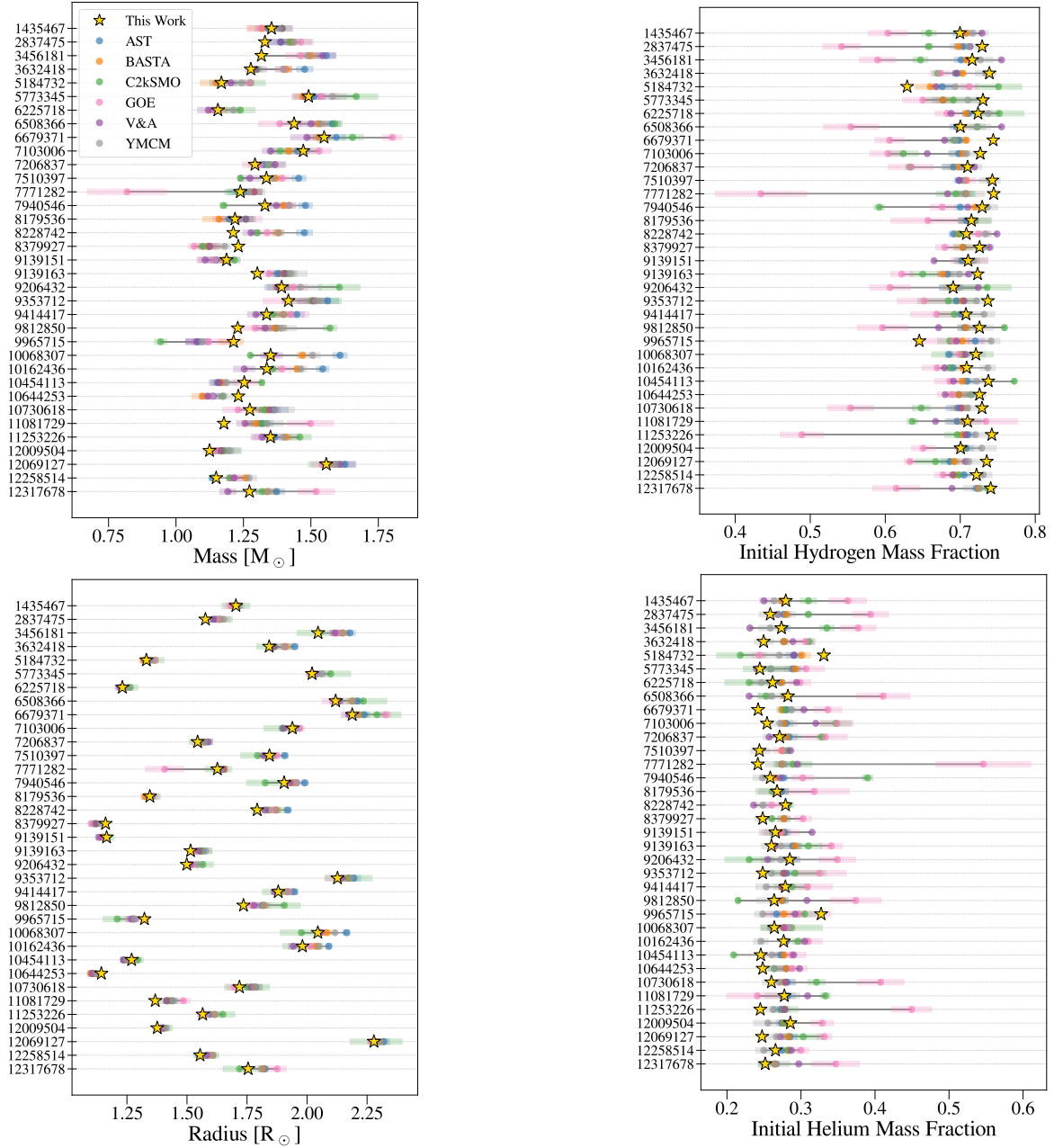


Figure C.2: Comparison of our model parameters to several pipelines used in Silva Aguirre et al. (2017). The results of each pipeline are indicated with a dot and the uncertainties of that result a shaded region of the same color.

Table C.1: Non-seismic observations

Star	T_{eff} [K]	[Fe/H]	L [L_{\odot}]
KIC 1435467	6325.0±100.0 ^a	0.04±0.1 ^a	4.051±0.073 ^d
KIC 2837475	6488.0±100.0 ^a	-0.07±0.1 ^a	4.7±0.019 ^d
KIC 3456181	6214.0±100.0 ^a	-0.26±0.1 ^a	6.72±0.04 ^d
KIC 3632418	6112.0±100.0 ^a	-0.16±0.1 ^a	4.973±0.073 ^d
KIC 4349452	6267.0±81.0 ^b	-0.06±0.15 ^b	2.379±0.015 ^d
KIC 5184732	5874.0±100.0 ^a	0.41±0.1 ^a	1.995±0.008 ^d
KIC 5773345	6127.0±82.0 ^b	0.21±0.1 ^b	5.429±0.03 ^d
KIC 5866724	6138.0±100.0 ^a	0.14±0.1 ^a	2.667±0.017 ^d
KIC 6225718	6203.0±100.0 ^a	-0.12±0.1 ^a	2.208±0.007 ^d
KIC 6508366	6249.0±100.0 ^a	-0.06±0.1 ^a	6.959±0.031 ^d
KIC 6679371	6387.0±100.0 ^a	-0.04±0.1 ^a	7.865±0.036 ^d
KIC 7103006	6362.0±100.0 ^a	0.05±0.1 ^a	5.747±0.019 ^d
KIC 7206837	6325.0±100.0 ^a	0.12±0.1 ^a	3.664±0.022 ^d
KIC 7510397	6109.0±100.0 ^a	-0.25±0.1 ^a	...
KIC 7670943	6302.0±100.0 ^a	0.01±0.1 ^a	2.98±0.041 ^d
KIC 7771282	6138.0±100.0 ^a	-0.07±0.1 ^a	3.654±0.029 ^d
KIC 7940546	6126.0±100.0 ^a	-0.27±0.1 ^a	5.443±0.059 ^d
KIC 8179536	6281.0±100.0 ^a	-0.04±0.1 ^a	2.666±0.015 ^d
KIC 8228742	6046.0±100.0 ^a	-0.09±0.1 ^a	4.273±0.042 ^d
KIC 8292840	6212.0±100.0 ^a	-0.21±0.1 ^a	2.608±0.054 ^d
KIC 8379927	6022.0±77.0 ^b	-0.24±0.35 ^b	...
KIC 8866102	6273.0±100.0 ^a	-0.09±0.1 ^a	2.814±0.013 ^d
KIC 9139151	6040.0±100.0 ^a	0.04±0.1 ^a	1.669±0.007 ^d
KIC 9139163	6350.0±100.0 ^a	0.09±0.1 ^a	3.755±0.028 ^d
KIC 9206432	6490.0±100.0 ^a	0.17±0.1 ^a	3.934±0.029 ^d
KIC 9353712	6140.0±100.0 ^a	-0.09±0.1 ^a	6.346±0.057 ^d
KIC 9414417	6283.0±100.0 ^a	-0.09±0.1 ^a	5.502±0.024 ^d
KIC 9592705	6148.0±100.0 ^a	0.27±0.1 ^a	5.987±0.098 ^d
KIC 9812850	6314.0±100.0 ^a	-0.18±0.1 ^a	4.621±0.021 ^d
KIC 9965715	6335.0±40.0 ^c	0.29±0.04 ^c	2.716±0.042 ^d
KIC 10068307	6050.0±100.0 ^a	-0.21±0.1 ^a	5.391±0.021 ^d
KIC 10162436	6134.0±100.0 ^a	-0.14±0.1 ^a	5.374±0.019 ^d
KIC 10454113	6136.0±100.0 ^a	-0.07±0.1 ^a	2.784±0.046 ^d
KIC 10644253	6020.0±100.0 ^a	0.09±0.1 ^a	1.515±0.006 ^d
KIC 10666592	6264.0±100.0 ^a	0.01±0.1 ^a	6.183±0.081 ^e
KIC 10730618	6423.0±168.0 ^b	-0.16±0.3 ^b	4.545±0.04 ^d
KIC 11081729	6416.0±100.0 ^a	-0.13±0.1 ^a	3.386±0.054 ^d
KIC 11253226	6474.0±100.0 ^a	-0.19±0.1 ^a	4.605±0.032 ^d
KIC 11807274	6150.0±100.0 ^a	-0.12±0.1 ^a	3.34±0.027 ^d
KIC 12009504	6129.0±100.0 ^a	-0.08±0.1 ^a	2.659±0.009 ^d
KIC 12069127	6186.0±100.0 ^a	0.03±0.1 ^a	7.677±0.082 ^d
KIC 12258514	5948.0±100.0 ^a	0.01±0.1 ^a	3.016±0.009 ^d
KIC 12317678	6395.0±100.0 ^a	-0.42±0.1 ^a	5.653±0.091 ^e

(a) Furlan et al. (2018), (b) Mathur et al. (2017), (c) Morel et al. (2021), (d) Creevey et al. (2023), (e) Gaia Collaboration et al. (2018)

Table C.2: Reference Model Parameters

Star	$M[M_{\odot}]$	Y_{initial}	Z_{initial}	α_{mlt}	f_{ov}	X_c	χ^2_{fit}	Category
KIC 1435467	1.3540	0.2794	0.0209	2.2396	0.0231	0.2689	2.32	H
KIC 2837475	1.3297	0.2584	0.0123	2.1497	0.0243	0.4000	7.2	A
KIC 3456181	1.3165	0.2736	0.0104	2.2254	0.0504	0.2191	6.1	H
KIC 3632418	1.2773	0.2496	0.0116	1.9093	0.0219	0.1037	2.29	A
KIC 4349452	1.1394	0.2867	0.0166	2.0684	0.0344	0.3853	1.13	H
KIC 5184732	1.1683	0.3309	0.0399	2.2366	0.0124	0.1589	27.77	A
KIC 5773345	1.4914	0.2443	0.0254	2.0132	0.0464	0.2997	3.8	A
KIC 5866724	1.2668	0.2619	0.0235	2.1377	0.0250	0.3511	1.82	L
KIC 6225718	1.1553	0.2617	0.0147	2.3102	0.0392	0.4493	7.73	HL
KIC 6508366	1.4378	0.2824	0.0175	2.1715	0.0394	0.2403	5.88	L
KIC 6679371	1.5490	0.2421	0.0140	2.1485	0.0110	0.1463	4.38	A
KIC 7103006	1.4718	0.2541	0.0192	2.1252	0.0294	0.3029	1.49	H
KIC 7206837	1.2928	0.2711	0.0191	1.9863	0.0355	0.4079	2.27	A
KIC 7510397	1.3352	0.2438	0.0134	2.1562	0.0168	0.0838	5.46	A
KIC 7670943	1.2531	0.2456	0.0169	2.3065	0.0165	0.2911	1.62	A
KIC 7771282	1.2384	0.2417	0.0137	2.0294	0.0401	0.2714	1.85	L
KIC 7940546	1.3297	0.2584	0.0123	2.1497	0.0243	0.1338	7.97	H
KIC 8179536	1.2186	0.2677	0.0174	2.1525	0.0329	0.4253	3.1	H
KIC 8228742	1.2124	0.2791	0.0128	2.1034	0.0261	0.0278	3.35	A
KIC 8292840	1.1336	0.2461	0.0099	1.9458	0.0127	0.1372	2.28	H
KIC 8379927	1.2308	0.2483	0.0259	2.1166	0.0085	0.5646	6.51	L
KIC 8866102	1.2175	0.2505	0.0139	2.1005	0.0026	0.2313	2.06	A
KIC 9139151	1.1872	0.2655	0.0240	2.3548	0.0143	0.4026	4.92	L
KIC 9139163	1.3016	0.2601	0.0167	2.0525	0.0370	0.4446	5.65	LH
KIC 9206432	1.3915	0.2849	0.0245	2.0034	0.0062	0.5158	4.49	A
KIC 9353712	1.4165	0.2483	0.0149	2.0718	0.0390	0.2046	1.94	A
KIC 9414417	1.3359	0.2789	0.0135	2.3704	0.0200	0.1195	2.79	A
KIC 9592705	1.4472	0.3096	0.0262	2.0641	0.0135	0.0848	3.29	H
KIC 9812850	1.2289	0.2637	0.0106	2.1612	0.0590	0.2986	1.27	H
KIC 9965715	1.2133	0.3272	0.0273	1.9746	0.0147	0.4504	20.35	A
KIC 10068307	1.3505	0.2640	0.0151	2.2139	0.0354	0.0988	7.49	A
KIC 10162436	1.3365	0.2766	0.0149	2.1053	0.0276	0.1281	3.87	A
KIC 10454113	1.2531	0.2456	0.0169	2.3065	0.0165	0.4990	9.16	A
KIC 10644253	1.2308	0.2483	0.0259	2.1166	0.0085	0.6138	2.5	H
KIC 10666592	1.5095	0.2403	0.0193	2.0247	0.0130	0.2321	1.86	A
KIC 10730618	1.2735	0.2600	0.0110	2.2181	0.0435	0.2946	3.46	A
KIC 11081729	1.1776	0.2775	0.0126	1.9915	0.0186	0.3516	4.65	L
KIC 11253226	1.3502	0.2450	0.0129	2.0507	0.0410	0.4803	7.3	A
KIC 11807274	1.2015	0.2445	0.0120	2.1044	0.0203	0.1399	3.65	H
KIC 12009504	1.1244	0.2856	0.0140	2.1580	0.0232	0.2365	4.7	A
KIC 12069127	1.5569	0.2474	0.0173	2.0223	0.0103	0.0847	1.8	A
KIC 12258514	1.1489	0.2656	0.0127	2.1986	0.0307	0.0890	10.74	A
KIC 12317678	1.2723	0.2517	0.0077	1.9616	0.0089	0.0771	4.0	A



Appendices for Chapter 4: Linearity of Structure Kernels in Main-sequence and Subgiant Solar-like Oscillators

D.1. Propagation of Kernel Errors

To understand why the high kernel errors cancel out in the test inversions of our main-sequence model but not our subgiant model, it is useful to see how each kernel error of each mode contributes to the overall result. To visualize this we define the quantity ε :

$$\varepsilon(j) = \sum_{i=0}^j c_i \text{KE}_i. \quad (\text{D.1})$$

Here, the index variables i, j correspond to a specific combination of n and ℓ , KE_i is the kernel error of the i -th mode (calculated using Equation 4.2), and c_i is the corresponding inversion coefficient. $\varepsilon(j)$ represents the cumulative kernel error after j modes have been added to the sum. Thus $\varepsilon(N)$, where N is the total number of modes, represents the total kernel error term in the inversion. In Figure D.1, we plot $\varepsilon(j)$ for one set of test inversions in each evolutionary stage. For the main-sequence star, the test model is the ‘High Kernel Error’ model and for the subgiant star, we use the ‘Match Less Mixed Modes’ model.

For the main-sequence test inversions across all target radii, the value of $\varepsilon(j)$ oscillates around zero and the final point, $\varepsilon(N)$, is smaller than the uncertainties of the inversion result. In the subgiant case however, there are a few modes that contribute much more to ε than others resulting in values of $\varepsilon(N)$ that are greater than the uncertainties propagated from observations.

D.2. Subgiant Higher Degree Modes and Singularity

D.2.1. Higher degree modes

Here we show the kernel errors of our subgiant grid for modes of spherical degree $\ell = 2$, Figure D.2, and $\ell = 3$, Figure D.3. These modes fall into two categories based on the character

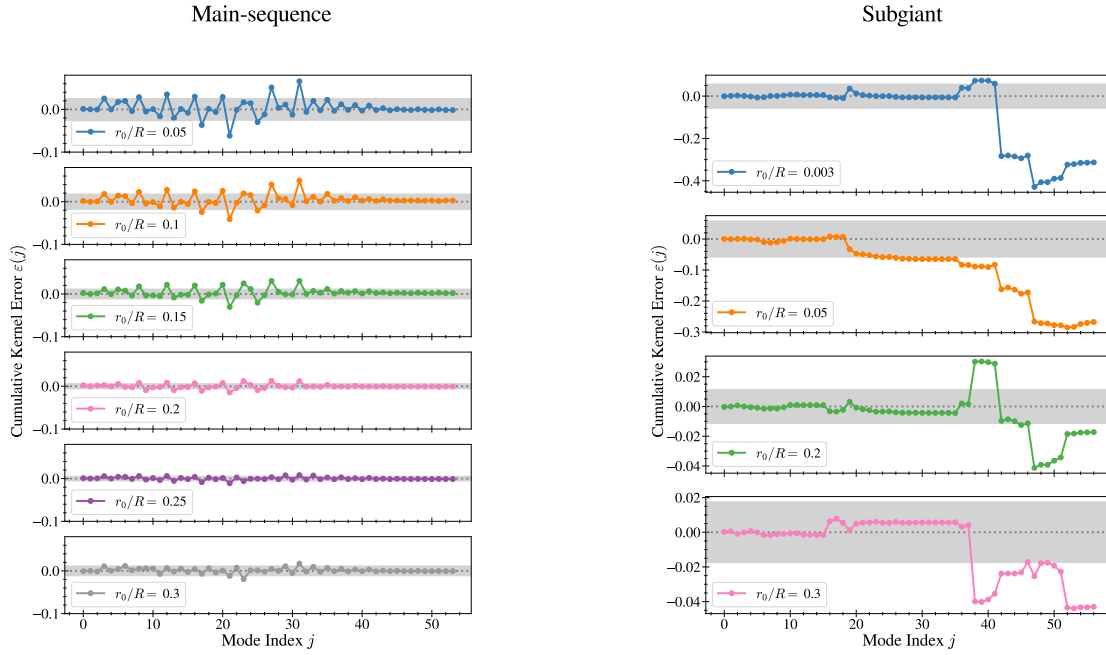


Figure D.1: Cumulative values of the kernel error, ($\varepsilon(j)$), defined in Equation D.1 for our test inversions on the main sequence (left) and subgiant branch (right). The rightmost point in each panel represents $\varepsilon(N)$, the total error in the inversion due to the underlying kernel errors. The gray-shaded region represents the uncertainty of the inversion result propagated from the uncertainty of the observed modes. The mode index values are discrete, however we connect the points to guide the eye.

of the mode in the reference model. For modes that are p-dominated in the reference model (high E_p/E) the kernel errors are low for test models that are in the same ridge of high E_p/E and high for all other models. Modes that are g-dominated in the reference model show similar behavior to the g-dominated dipole modes discussed in Section 4.4.1, although the region of linearity is smaller. This is due to the fact that higher-order modes evolve more quickly through avoided crossings.

D.2.2. Singularity

Bellinger et al. (2021) found a singularity in the equation used to obtain the u, Y kernels. They note that this singularity occurs when $\lambda = 1$ where λ is the eigenvalue of the homogeneous eigenvalue analogous to the differential equation used to obtain the u, Y kernels. As a model evolves through this singularity the peaks of the mode kernels on either side of the hydrogen-burning shell increase rapidly in amplitude and then change signs at the singularity, see Figure 4 of Bellinger et al. (2021). This singularity affects all of the mode kernels of the model. However, it does not appear to affect the kernel errors as long as the reference model used is not passing through the singularity.

We also calculate the kernel errors using a reference model that is passing through this singularity $\lambda = 1.0001$. As seen in Figure D.4, the region of linearity for this new reference model is extremely small even for the radial modes. This is in agreement with the conclusion in Bellinger et al. (2021) that models with $|\lambda - 1| \gtrsim 0.005$ should not be used for structure inversions.

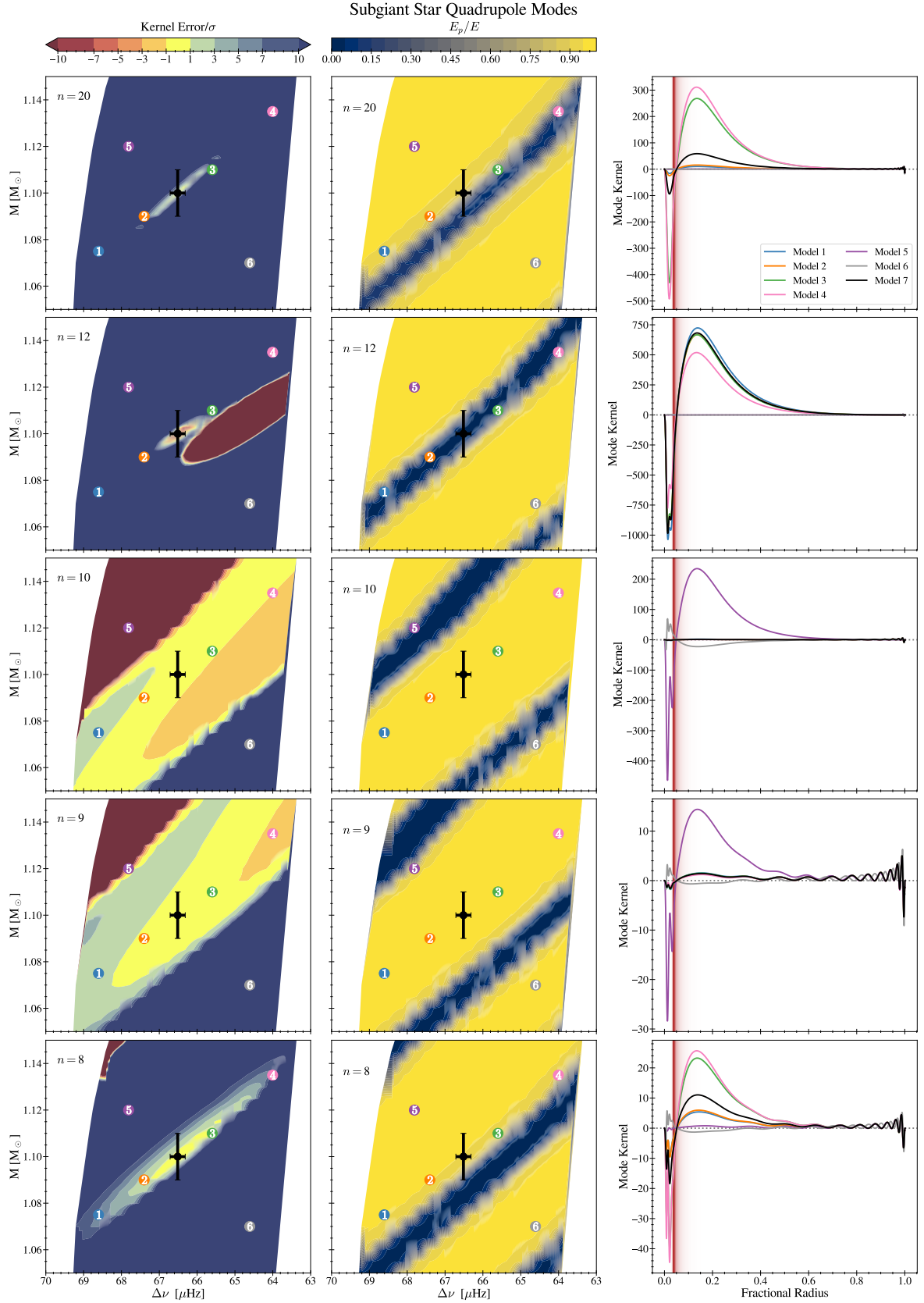


Figure D.2: Kernel errors for the quadrupole modes of the subgiant stars. All colors and symbols have the same meaning as in Figure 4.4.

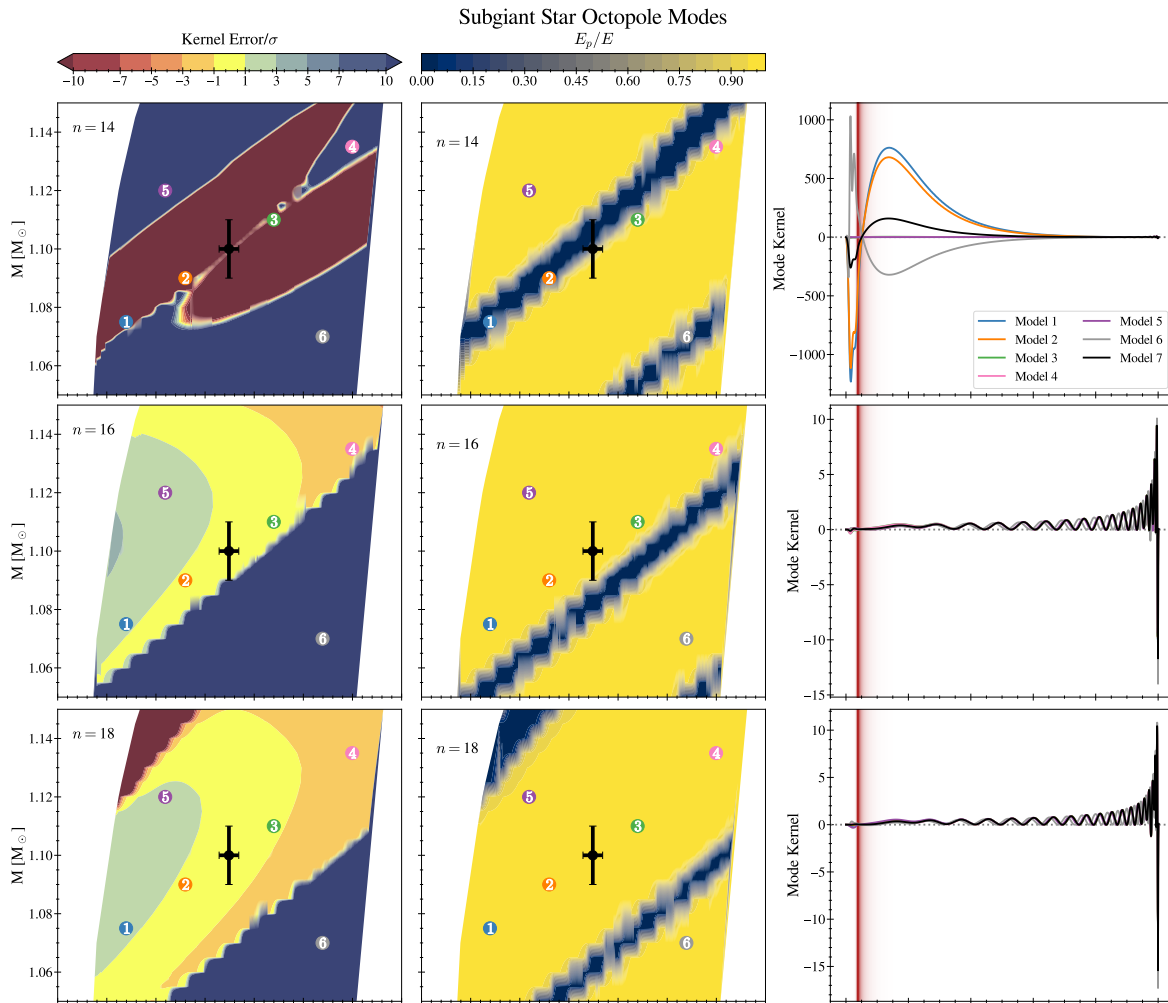


Figure D.3: Kernel errors for the octopole modes of the subgiant stars. All colors and symbols have the same meaning as in Figure 4.4.

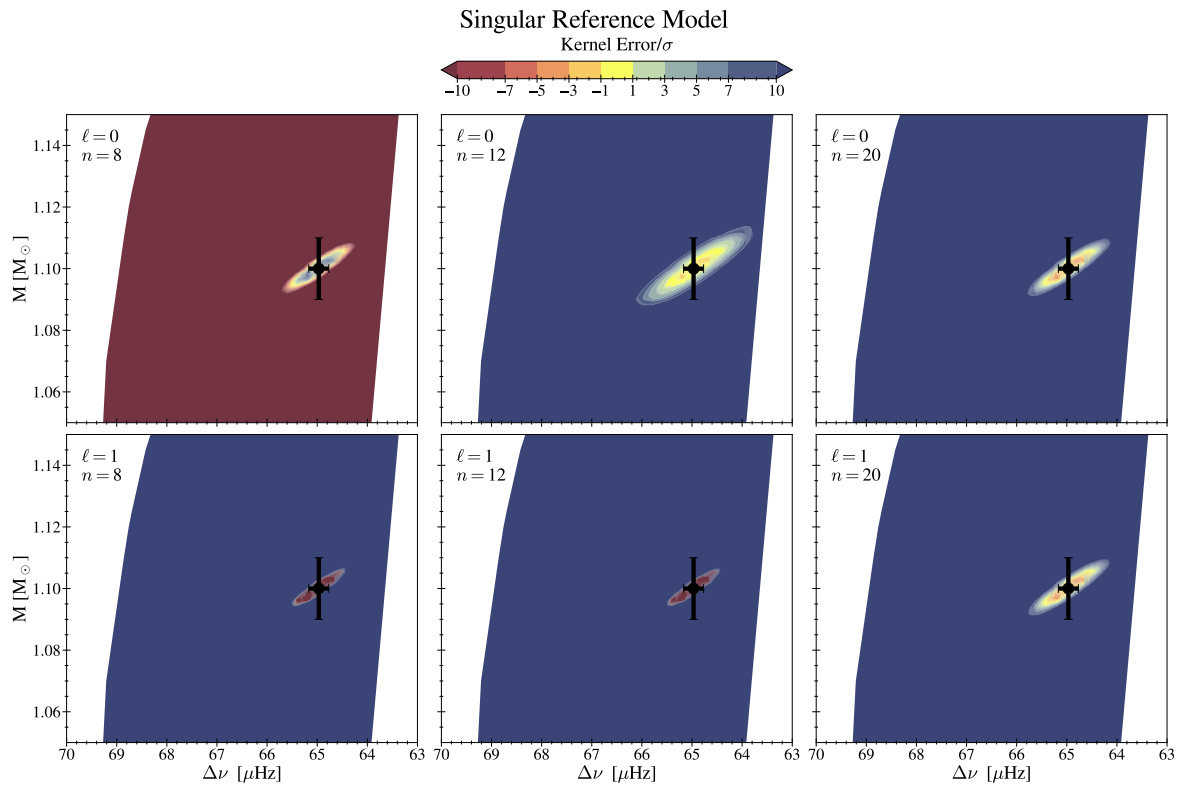


Figure D.4: Kernel errors for several modes when the reference model used is passing through the singularity discussed in Bellinger et al. (2021). The symbols have the same meaning as in Figure 4.3.

List of publications

Papers used in this thesis:

- [1] **Lynn Buchele**; Earl P. Bellinger; Saskia Hekker; Sarbani Basu; soon to be submitted; *Linearity of Structure Kernels in Main-sequence and Subgiant Solar-like Oscillators*
- [2] **Lynn Buchele**; Earl P. Bellinger; Saskia Hekker; Sarbani Basu; under review for publication in the *Astrophysical Journal*; *Asteroseismic Structure Inversions of Main-Sequence Solar-like Oscillators with Convective Cores*
- [3] **Lynn Buchele**; Earl P. Bellinger; Saskia Hekker; Sarbani Basu,; Warrick Ball; Jørgen Christensen-Dalsgaard; 2024, *ApJ*, 961, 198; *Asteroseismic Inversions for Internal Sound Speed Profiles of Main-sequence Stars with Radiative Cores*

Papers not used in this thesis:

- [1] A Solomey, N.; Folkerts, J.; Meyer, H.; Gimar, C.; Novak, J.; Doty, B.; English, T.; **Buchele, L.**; Nelsen, A.; McTaggart, R.; Christl, M. 2023, *NIMRA*, 1049, 168064: *Concept for a space-based near-solar neutrino detector*

Bibliography

- Aerts, C., “Probing the interior physics of stars through asteroseismology,” *Reviews of Modern Physics*, vol. 93, no. 1, 015001, 2021, doi:10.1103/RevModPhys.93.015001.
- Aerts, C., Christensen-Dalsgaard, J., and Kurtz, D. W., *Asteroseismology*, Springer, 2010, doi:10.1007/978-1-4020-5803-5.
- Aguirre Børsen-Koch, V., Rørsted, J. L., Justesen, A. B., Stokholm, A., Verma, K., Winther, M. L., Knudstrup, E., Nielsen, K. B., Sahlholdt, C., Larsen, J. R., et al., “The BAYesian STellar algorithm (BASTA): a fitting tool for stellar studies, asteroseismology, exoplanets, and Galactic archaeology,” *MNRAS*, vol. 509, no. 3, pp. 4344–4364, 2022, doi:10.1093/mnras/stab2911.
- Ahlborn, F., Bellinger, E. P., Hekker, S., Basu, S., and Angelou, G. C., “Asteroseismic sensitivity to internal rotation along the red-giant branch,” *A&A*, vol. 639, A98, 2020, doi:10.1051/0004-6361/201936947.
- Ahlborn, F., Bellinger, E. P., Hekker, S., Basu, S., and Mokrytska, D., “Improved asteroseismic inversions for red-giant surface rotation rates,” *A&A*, vol. 668, A98, 2022, doi:10.1051/0004-6361/202142510.
- Ahlborn, F., Bellinger, E. P., Hekker, S., Basu, S., and Mokrytska, D., “The robustness of inferred envelope and core rotation rates of red giant stars from asteroseismology,” *A&A*, vol. 693, A274, 2025, doi:10.1051/0004-6361/202449901.
- Aizenman, M., Smeyers, P., and Weigert, A., “Avoided Crossing of Modes of Non-radial Stellar Oscillations,” *A&A*, vol. 58, p. 41, 1977.
- Alexander, D. R. and Ferguson, J. W., “Low-Temperature Rosseland Opacities,” *ApJ*, vol. 437, p. 879, 1994, doi:10.1086/175039.
- Anders, F., Gispert, P., Ratcliffe, B., Chiappini, C., Minchev, I., Nepal, S., Queiroz, A. B. A., Amarante, J. A. S., Antoja, T., Casali, G., et al., “Spectroscopic age estimates for APOGEE red-giant stars: Precise spatial and kinematic trends with age in the Galactic disc,” *A&A*, vol. 678, A158, 2023, doi:10.1051/0004-6361/202346666.
- Angelou, G. C., Bellinger, E. P., Hekker, S., Mints, A., Elsworth, Y., Basu, S., and Weiss, A., “Convective boundary mixing in low- and intermediate-mass stars - I. Core properties from pressure-mode asteroseismology,” *MNRAS*, vol. 493, no. 4, pp. 4987–5004, 2020, doi:10.1093/mnras/staa390.
- Angulo, C., Arnould, M., Rayet, M., Descouvemont, P., Baye, D., Leclercq-Willain, C.,

- Coc, A., Barhoumi, S., Aguer, P., Rolfs, C., et al., “A compilation of charged-particle induced thermonuclear reaction rates,” *Nucl. Phys. A*, vol. 656, no. 1, pp. 3–183, 1999, doi:10.1016/S0375-9474(99)00030-5.
- Asplund, M., Grevesse, N., Sauval, A. J., and Scott, P., “The Chemical Composition of the Sun,” *ARA&A*, vol. 47, no. 1, pp. 481–522, 2009, doi:10.1146/annurev.astro.46.060407.145222.
- Auvergne, M., Bodin, P., Boissard, L., Buey, J. T., Chaintreuil, S., Epstein, G., Joutet, M., Lam-Trong, T., Levacher, P., Magnan, A., et al., “The CoRoT satellite in flight: description and performance,” *A&A*, vol. 506, no. 1, pp. 411–424, 2009, doi:10.1051/0004-6361/200810860.
- Backus, G. and Gilbert, F., “The Resolving Power of Gross Earth Data,” *Geophysical Journal*, vol. 16, no. 2, pp. 169–205, 1968, doi:10.1111/j.1365-246X.1968.tb00216.x.
- Backus, G. and Gilbert, F., “Uniqueness in the Inversion of Inaccurate Gross Earth Data,” *Philosophical Transactions of the Royal Society of London Series A*, vol. 266, no. 1173, pp. 123–192, 1970, doi:10.1098/rsta.1970.0005.
- Baglin, A., Auvergne, M., Barge, P., Deleuil, M., Michel, E., and CoRoT Exoplanet Science Team, “CoRoT: Description of the Mission and Early Results,” in Pont, F., Sasselov, D., and Holman, M. J. (editors), “Transiting Planets,” *IAU Symposium*, vol. 253, pp. 71–81, 2009, doi:10.1017/S1743921308026252.
- Ball, W. H. and Gizon, L., “A new correction of stellar oscillation frequencies for near-surface effects,” *A&A*, vol. 568, A123, 2014, doi:10.1051/0004-6361/201424325.
- Basu, S., “Stellar Inversions,” *Ap&SS*, vol. 284, no. 1, pp. 153–164, 2003, doi:10.1023/A:1023223115165.
- Basu, S., “Global seismology of the Sun,” *Living Reviews in Solar Physics*, vol. 13, no. 1, 2, 2016, doi:10.1007/s41116-016-0003-4.
- Basu, S. and Chaplin, W. J., *Asteroseismic Data Analysis: Foundations and Techniques*, Princeton University Press, 2017.
- Basu, S., Chaplin, W. J., Elsworth, Y., New, R., and Serenelli, A. M., “Fresh Insights on the Structure of the Solar Core,” *ApJ*, vol. 699, no. 2, pp. 1403–1417, 2009, doi:10.1088/0004-637X/699/2/1403.
- Basu, S. and Christensen-Dalsgaard, J., “Equation of state and helioseismic inversions.” *A&A*, vol. 322, pp. L5–L8, 1997, doi:10.48550/arXiv.astro-ph/9702162.
- Basu, S., Christensen-Dalsgaard, J., and Thompson, M. J., “SOLA inversions for the core structure of solar-type stars,” in Battrick, B., Favata, F., Roxburgh, I. W., and Galadi, D. (editors), “Stellar Structure and Habitable Planet Finding,” *ESA Special Publication*, vol. 485, pp. 249–252, 2002, doi:10.48550/arXiv.astro-ph/0110446.
- Basu, S., Pinsonneault, M. H., and Bahcall, J. N., “How Much Do Helioseismological Inferences Depend on the Assumed Reference Model?” *ApJ*, vol. 529, no. 2, pp. 1084–1100, 2000, doi:10.1086/308302.
- Batchelor, G. K., *The Theory of Homogeneous Turbulence*, Cambridge University Press, 1953.
- Bazot, M., Bourguignon, S., and Christensen-Dalsgaard, J., “Estimation of stellar parameters using Monte Carlo Markov Chains,” *Mem. Soc. Astron. Italiana*, vol. 79, p. 660, 2008, doi:10.48550/arXiv.0803.2529.
- Bedding, T. R., Butler, R. P., Kjeldsen, H., Baldry, I. K., O’Toole, S. J., Tinney, C. G.,

- Marcy, G. W., Kienzie, F., and Carrier, F., “Evidence for Solar-like Oscillations in β Hydri,” *ApJ*, vol. 549, no. 1, pp. L105–L108, 2001, doi:10.1086/319139.
- Bedding, T. R. and Kjeldsen, H., “Observations of solar-like oscillations,” *Communications in Asteroseismology*, vol. 150, p. 106, 2007, doi:10.1553/cia150s106.
- Bellinger, E. P., Angelou, G. C., Hekker, S., Basu, S., Ball, W. H., and Guggenberger, E., “Fundamental Parameters of Main-Sequence Stars in an Instant with Machine Learning,” *ApJ*, vol. 830, no. 1, 31, 2016, doi:10.3847/0004-637X/830/1/31.
- Bellinger, E. P., Basu, S., and Hekker, S., “Inverse Analysis of Asteroseismic Data: A Review,” in Monteiro, M. J. P. F. G., García, R. A., Christensen-Dalsgaard, J., and McIntosh, S. W. (editors), “Dynamics of the Sun and Stars; Honoring the Life and Work of Michael J. Thompson,” *Astrophysics and Space Science Proceedings*, vol. 57, pp. 171–183, 2020a, doi:10.1007/978-3-030-55336-4_25.
- Bellinger, E. P., Basu, S., Hekker, S., and Ball, W. H., “Model-independent Measurement of Internal Stellar Structure in 16 Cygni A and B,” *ApJ*, vol. 851, no. 2, 80, 2017, doi:10.3847/1538-4357/aa9848.
- Bellinger, E. P., Basu, S., Hekker, S., and Christensen-Dalsgaard, J., “Testing Stellar Evolution with Asteroseismic Inversions of a Main-sequence Star Harboring a Small Convective Core,” *ApJ*, vol. 885, no. 2, 143, 2019a, doi:10.3847/1538-4357/ab4a0d.
- Bellinger, E. P., Basu, S., Hekker, S., Christensen-Dalsgaard, J., and Ball, W. H., “Asteroseismic Inference of the Central Structure in a Subgiant Star,” *ApJ*, vol. 915, no. 2, 100, 2021, doi:10.3847/1538-4357/ac0051.
- Bellinger, E. P. and Christensen-Dalsgaard, J., “Asteroseismic Constraints on the Cosmic-time Variation of the Gravitational Constant from an Ancient Main-sequence Star,” *ApJ*, vol. 887, no. 1, L1, 2019, doi:10.3847/2041-8213/ab43e7.
- Bellinger, E. P., Hekker, S., Angelou, G. C., Stokholm, A., and Basu, S., “Stellar ages, masses, and radii from asteroseismic modeling are robust to systematic errors in spectroscopy,” *A&A*, vol. 622, A130, 2019b, doi:10.1051/0004-6361/201834461.
- Bellinger, E. P., Kanbur, S. M., Bhardwaj, A., and Marconi, M., “When a period is not a full stop: Light-curve structure reveals fundamental parameters of Cepheid and RR Lyrae stars,” *MNRAS*, vol. 491, no. 4, pp. 4752–4767, 2020b, doi:10.1093/mnras/stz3292.
- Benomar, O., Takata, M., Shibahashi, H., Ceillier, T., and García, R. A., “Nearly uniform internal rotation of solar-like main-sequence stars revealed by space-based asteroseismology and spectroscopic measurements,” *MNRAS*, vol. 452, no. 3, pp. 2654–2674, 2015, doi:10.1093/mnras/stv1493.
- Bertelli, G., Bressan, A., Chiosi, C., and Angerer, K., “Evolutionary models for low and intermediate mass stars with convective overshooting,” *A&AS*, vol. 66, pp. 191–234, 1986.
- Bétrisey, J., Buldgen, G., Reese, D. R., and Meynet, G., “Asteroseismic modelling strategies in the PLATO era. II. Automation of seismic inversions and quality assessment procedure,” *A&A*, vol. 681, A99, 2024, doi:10.1051/0004-6361/202347594.
- Bétrisey, J., Eggenberger, P., Buldgen, G., Benomar, O., and Bazot, M., “Testing angular momentum transport processes with asteroseismology of solar-type main-sequence stars,” *A&A*, vol. 673, L11, 2023, doi:10.1051/0004-6361/202245764.
- Borucki, W. J., Koch, D., Basri, G., Batalha, N., Brown, T., Caldwell, D., Caldwell, J., Christensen-Dalsgaard, J., Cochran, W. D., DeVore, E., et al., “Kepler Planet-Detection Mission: Introduction and First Results,” *Science*, vol. 327, no. 5968, p. 977, 2010,

- doi:10.1126/science.1185402.
- Bowman, D. M. and Bugnet, L., “Asteroseismology,” *arXiv e-prints*, arXiv:2410.01715, 2024, doi:10.48550/arXiv.2410.01715.
- Broomhall, A. M., Chaplin, W. J., Davies, G. R., Elsworth, Y., Fletcher, S. T., Hale, S. J., Miller, B., and New, R., “Definitive Sun-as-a-star p-mode frequencies: 23 years of BiSON observations,” *MNRAS*, vol. 396, no. 1, pp. L100–L104, 2009, doi:10.1111/j.1745-3933.2009.00672.x.
- Brown, T. M., Gilliland, R. L., Noyes, R. W., and Ramsey, L. W., “Detection of possible p-mode oscillations on Procyon,” *Astrophysical Journal; (USA)*, vol. 368, 1991, doi:10.1086/169725.
- Brown, T. M., Gilliland, R. L., Noyes, R. W., and Ramsey, L. W., “Detection of Possible p-Mode Oscillations on Procyon,” *ApJ*, vol. 368, p. 599, 1991, doi:10.1086/169725.
- Buchele, L., Bellinger, E. P., Hekker, S., and Basu, S., “Asteroseismic Structure Inversions of Main-Sequence Solar-like Oscillators with Convective Cores,” *arXiv e-prints*, arXiv:2412.05094, 2024a, doi:10.48550/arXiv.2412.05094.
- Buchele, L., Bellinger, E. P., Hekker, S., Basu, S., Ball, W., and Christensen-Dalsgaard, J., “Asteroseismic Inversions for Internal Sound Speed Profiles of Main-sequence Stars with Radiative Cores,” *ApJ*, vol. 961, no. 2, 198, 2024b, doi:10.3847/1538-4357/ad1680.
- Buldgen, G., Bétrisey, J., Roxburgh, I. W., Vorontsov, S. V., and Reese, D. R., “Inversions of Stellar Structure From Asteroseismic Data,” *Frontiers in Astronomy and Space Sciences*, vol. 9, 942373, 2022a, doi:10.3389/fspas.2022.942373.
- Buldgen, G., Farnir, M., Eggenberger, P., Bétrisey, J., Pezzotti, C., Pinçon, C., Deal, M., and Salmon, S. J. A. J., “Thorough characterisation of the 16 Cygni system. II. Seismic inversions of the internal structure,” *A&A*, vol. 661, A143, 2022b, doi:10.1051/0004-6361/202142001.
- Buldgen, G., Reese, D. R., and Dupret, M. A., “Using seismic inversions to obtain an indicator of internal mixing processes in main-sequence solar-like stars,” *A&A*, vol. 583, A62, 2015a, doi:10.1051/0004-6361/201526390.
- Buldgen, G., Reese, D. R., and Dupret, M. A., “Analysis of the linear approximation of seismic inversions for various structural pairs,” *A&A*, vol. 598, A21, 2017, doi:10.1051/0004-6361/201629485.
- Buldgen, G., Reese, D. R., and Dupret, M. A., “Constraining convective regions with asteroseismic linear structural inversions,” *A&A*, vol. 609, A95, 2018, doi:10.1051/0004-6361/201730693.
- Buldgen, G., Reese, D. R., Dupret, M. A., and Samadi, R., “Stellar acoustic radii, mean densities, and ages from seismic inversion techniques,” *A&A*, vol. 574, A42, 2015b, doi:10.1051/0004-6361/201424613.
- Busso, M., Gallino, R., and Wasserburg, G. J., “Nucleosynthesis in Asymptotic Giant Branch Stars: Relevance for Galactic Enrichment and Solar System Formation,” *ARA&A*, vol. 37, pp. 239–309, 1999, doi:10.1146/annurev.astro.37.1.239.
- Campilho, B., Deal, M., and Bossini, D., “Atomic diffusion in solar-like stars with MESA. Comparison with the Montreal/Montpellier and CESTAM stellar evolution codes,” *A&A*, vol. 659, A162, 2022, doi:10.1051/0004-6361/202140821.
- Castelli, F. and Kurucz, R. L., “New Grids of ATLAS9 Model Atmospheres,” in Piskunov, N., Weiss, W. W., and Gray, D. F. (editors), “Modelling of Stellar Atmospheres,” *IAU*

- Symposium*, vol. 210, p. A20, 2003, doi:10.48550/arXiv.astro-ph/0405087.
- Chandrasekhar, S., “A General Variational Principle Governing the Radial and the Non-Radial Oscillations of Gaseous Masses.” *ApJ*, vol. 139, p. 664, 1964, doi:10.1086/147792.
- Chaplin, W. J. and Miglio, A., “Asteroseismology of Solar-Type and Red-Giant Stars,” *ARA&A*, vol. 51, no. 1, pp. 353–392, 2013, doi:10.1146/annurev-astro-082812-140938.
- Charpinet, S., Fontaine, G., Brassard, P., Green, E. M., and Chayer, P., “Structural parameters of the hot pulsating B subdwarf δ ASTROBJ δ PG 1219+534 δ /ASTROBJ δ from asteroseismology,” *A&A*, vol. 437, no. 2, pp. 575–597, 2005, doi:10.1051/0004-6361:20052709.
- Christensen-Dalsgaard, J., “Helioseismology,” *Reviews of Modern Physics*, vol. 74, no. 4, pp. 1073–1129, 2002, doi:10.1103/RevModPhys.74.1073.
- Christensen-Dalsgaard, J., “Solar structure and evolution,” *Living Reviews in Solar Physics*, vol. 18, no. 1, 2, 2021, doi:10.1007/s41116-020-00028-3.
- Christensen-Dalsgaard, J. and Berthomieu, G., “Theory of solar oscillations.” in Cox, A. N., Livingston, W. C., and Matthews, M. S. (editors), “Solar Interior and Atmosphere,” pp. 401–478, 1991.
- Christensen-Dalsgaard, J., Dappen, W., Ajukov, S. V., Anderson, E. R., Antia, H. M., Basu, S., Baturin, V. A., Berthomieu, G., Chaboyer, B., Chitre, S. M., et al., “The Current State of Solar Modeling,” *Science*, vol. 272, no. 5266, pp. 1286–1292, 1996, doi:10.1126/science.272.5266.1286.
- Christensen-Dalsgaard, J. and Perez Hernandez, F., “The phase function for stellar acoustic oscillations. I - Theory,” *MNRAS*, vol. 257, no. 1, pp. 62–88, 1992, doi:10.1093/mnras/257.1.62.
- Chugunov, A. I., Dewitt, H. E., and Yakovlev, D. G., “Coulomb tunneling for fusion reactions in dense matter: Path integral MonteCarlo versus mean field,” *Phys. Rev. D*, vol. 76, no. 2, 025028, 2007, doi:10.1103/PhysRevD.76.025028.
- Claverie, A., Isaak, G. R., McLeod, C. P., van der Raay, H. B., and Roca Cortes, T., “Solar structure from global studies of the 5-minute oscillation,” *Nature*, vol. 282, pp. 591–594, 1979, doi:10.1038/282591a0.
- Colgan, J., Kilcrease, D. P., Magee, N. H., Sherrill, M. E., Abdallah, J., Jr., Hakel, P., Fontes, C. J., Guzik, J. A., and Mussack, K. A., “A New Generation of Los Alamos Opacity Tables,” *ApJ*, vol. 817, no. 2, 116, 2016, doi:10.3847/0004-637X/817/2/116.
- Cox, J. P. and Giuli, R. T., *Principles of stellar structure*, Gordon and Breach, 1968.
- Creevey, O. L., Sordo, R., Pailler, F., Frémat, Y., Heiter, U., Thévenin, F., Andrae, R., Fouesneau, M., Lobel, A., Bailer-Jones, C. A. L., et al., “Gaia Data Release 3. Astrophysical parameters inference system (Apsis). I. Methods and content overview,” *A&A*, vol. 674, A26, 2023, doi:10.1051/0004-6361/202243688.
- Creevey, O. L., Sordo, R., Pailler, F., Frémat, Y., Heiter, U., Thévenin, F., Andrae, R., Fouesneau, M., Lobel, A., Bailer-Jones, C. A. L., et al., “Gaia Data Release 3: Astrophysical parameters inference system (Apsis). I. Methods and content overview,” *Astronomy & Astrophysics*, vol. 674, p. A26, 2023, doi:10.1051/0004-6361/202243688.
- Cunha, M. S., Roxburgh, I. W., Aguirre Børsen-Koch, V., Ball, W. H., Basu, S., Chaplin, W. J., Goupil, M. J., Nsamba, B., Ong, J., Reese, D. R., et al., “PLATO hare-and-hounds exercise: asteroseismic model fitting of main-sequence solar-like pulsators,” *MNRAS*,

- vol. 508, no. 4, pp. 5864–5885, 2021, doi:10.1093/mnras/stab2886.
- Cyburt, R. H., Amthor, A. M., Ferguson, R., Meisel, Z., Smith, K., Warren, S., Heger, A., Hoffman, R. D., Rauscher, T., Sakharuk, A., et al., “The JINA REACLIB Database: Its Recent Updates and Impact on Type-I X-ray Bursts,” *ApJS*, vol. 189, pp. 240–252, 2010, doi:10.1088/0067-0049/189/1/240.
- Davies, G. R., Silva Aguirre, V., Bedding, T. R., Handberg, R., Lund, M. N., Chaplin, W. J., Huber, D., White, T. R., Benomar, O., Hekker, S., et al., “Oscillation frequencies for 35 Kepler solar-type planet-hosting stars using Bayesian techniques and machine learning,” *MNRAS*, vol. 456, no. 2, pp. 2183–2195, 2016, doi:10.1093/mnras/stv2593.
- Deal, M., Alecian, G., Lebreton, Y., Goupil, M. J., Marques, J. P., LeBlanc, F., Morel, P., and Pichon, B., “Impacts of radiative accelerations on solar-like oscillating main-sequence stars,” *A&A*, vol. 618, A10, 2018, doi:10.1051/0004-6361/201833361.
- Deal, M., Goupil, M. J., Cunha, M. S., Monteiro, M. J. P. F. G., Lebreton, Y., Christophe, S., Pereira, F., Samadi, R., Oreshina, A. V., and Buldgen, G., “Glitches in solar-like oscillating F-type stars. Theoretical signature of the base of the convective envelope on the ratios r_{010} ,” *A&A*, vol. 673, A49, 2023, doi:10.1051/0004-6361/202245103.
- Deal, M., Goupil, M. J., Marques, J. P., Reese, D. R., and Lebreton, Y., “Chemical mixing in low mass stars. I. Rotation against atomic diffusion including radiative acceleration,” *A&A*, vol. 633, A23, 2020, doi:10.1051/0004-6361/201936666.
- Deheuvels, S., Doğan, G., Goupil, M. J., Appourchaux, T., Benomar, O., Bruntt, H., Campante, T. L., Casagrande, L., Ceillier, T., Davies, G. R., et al., “Seismic constraints on the radial dependence of the internal rotation profiles of six Kepler subgiants and young red giants,” *A&A*, vol. 564, A27, 2014, doi:10.1051/0004-6361/201322779.
- Deheuvels, S. and Michel, E., “Constraints on the structure of the core of subgiants via mixed modes: the case of HD 49385,” *A&A*, vol. 535, A91, 2011, doi:10.1051/0004-6361/201117232.
- Deubner, F.-L. and Gough, D., “Helioseismology: Oscillations as a Diagnostic of the Solar Interior,” *ARA&A*, vol. 22, pp. 593–619, 1984, doi:10.1146/annurev.aa.22.090184.003113.
- Dziembowski, W. A., “Nonradial Oscillations of Evolved Stars. I. Quasiadiabatic Approximation,” *Acta Astron.*, vol. 21, pp. 289–306, 1971.
- Dziembowski, W. A., Pamyatnykh, A. A., and Sienkiewicz, R., “Solar model from helioseismology and the neutrino flux problem,” *MNRAS*, vol. 244, pp. 542–550, 1990.
- Elliott, J. R., “Equation of state in the solar convection zone and the implications of helioseismology,” *Monthly Notices of the Royal Astronomical Society*, vol. 280, no. 4, pp. 1244–1256, 1996, doi:10.1093/mnras/280.4.1244.
- Elliott, J. R., “Equation of state in the solar convection zone and the implications of helioseismology,” *MNRAS*, vol. 280, no. 4, pp. 1244–1256, 1996, doi:10.1093/mnras/280.4.1244.
- Evans, J. W. and Michard, R., “Observational Study of Macroscopic Inhomogeneities in the Solar Atmosphere. III. Vertical Oscillatory Motions in the Solar Photosphere.” *ApJ*, vol. 136, p. 493, 1962, doi:10.1086/147403.
- Farnir, M., Dupret, M. A., Buldgen, G., Salmon, S. J. A. J., Noels, A., Pinçon, C., Pezzotti, C., and Eggenberger, P., “Thorough characterisation of the 16 Cygni system. I. Forward seismic modelling with WhoSGLAd,” *A&A*, vol. 644, A37, 2020, doi:10.1051/0004-

- 6361/202038522.
- Farrell, E., Buldgen, G., Meynet, G., Eggenberger, P., Dupret, M.-A., and Bowman, D. M., “A method for non-linear inversion of the stellar structure applied to gravity-mode pulsators,” *A&A*, vol. 686, A267, 2024, doi:10.1051/0004-6361/202449430.
- Ferguson, J. W., Alexander, D. R., Allard, F., Barman, T., Bodnarik, J. G., Hauschildt, P. H., Heffner-Wong, A., and Tamanai, A., “Low-Temperature Opacities,” *ApJ*, vol. 623, pp. 585–596, 2005, doi:10.1086/428642.
- Frandsen, S., Carrier, F., Aerts, C., Stello, D., Maas, T., Burnet, M., Bruntt, H., Teixeira, T. C., de Medeiros, J. R., Bouchy, F., et al., “Detection of Solar-like oscillations in the G7 giant star ξ Hya,” *A&A*, vol. 394, pp. L5–L8, 2002, doi:10.1051/0004-6361:20021281.
- Freytag, B., Ludwig, H. G., and Steffen, M., “Hydrodynamical models of stellar convection. The role of overshoot in DA white dwarfs, A-type stars, and the Sun.” *A&A*, vol. 313, pp. 497–516, 1996.
- Fuller, G. M., Fowler, W. A., and Newman, M. J., “Stellar weak interaction rates for intermediate-mass nuclei. IV - Interpolation procedures for rapidly varying lepton capture rates using effective log (ft)-values,” *ApJ*, vol. 293, pp. 1–16, 1985, doi:10.1086/163208.
- Furlan, E., Ciardi, D. R., Cochran, W. D., Everett, M. E., Latham, D. W., Marcy, G. W., Buchhave, L. A., Endl, M., Isaacson, H., Petigura, E. A., et al., “The Kepler Follow-up Observation Program. II. Stellar Parameters from Medium- and High-resolution Spectroscopy,” *The Astrophysical Journal*, vol. 861, no. 2, p. 149, 2018, doi:10.3847/1538-4357/aaca34.
- Furlan, E., Ciardi, D. R., Cochran, W. D., Everett, M. E., Latham, D. W., Marcy, G. W., Buchhave, L. A., Endl, M., Isaacson, H., Petigura, E. A., et al., “The Kepler Follow-up Observation Program. II. Stellar Parameters from Medium- and High-resolution Spectroscopy,” *ApJ*, vol. 861, no. 2, 149, 2018, doi:10.3847/1538-4357/aaca34.
- Gaia Collaboration, Brown, A. G. A., Vallenari, A., Prusti, T., de Bruijne, J. H. J., Babusiaux, C., Bailer-Jones, C. A. L., Biermann, M., Evans, D. W., Eyer, L., et al., “Gaia Data Release 2. Summary of the contents and survey properties,” *A&A*, vol. 616, A1, 2018, doi:10.1051/0004-6361/201833051.
- Gaia Collaboration, Prusti, T., de Bruijne, J. H. J., Brown, A. G. A., Vallenari, A., Babusiaux, C., Bailer-Jones, C. A. L., Bastian, U., Biermann, M., Evans, D. W., et al., “The Gaia mission,” *A&A*, vol. 595, A1, 2016, doi:10.1051/0004-6361/201629272.
- Gaia Collaboration, Vallenari, A., Brown, A. G. A., Prusti, T., de Bruijne, J. H. J., Arenou, F., Babusiaux, C., Biermann, M., Creevey, O. L., Ducourant, C., et al., “Gaia Data Release 3: Summary of the content and survey properties,” *arXiv e-prints*, arXiv:2208.00211, 2022, doi:10.48550/arXiv.2208.00211.
- García, R. A. and Ballot, J., “Asteroseismology of solar-type stars,” *Living Reviews in Solar Physics*, vol. 16, no. 1, 4, 2019, doi:10.1007/s41116-019-0020-1.
- Gent, M. R., Bergemann, M., Serenelli, A., Casagrande, L., Gerber, J. M., Heiter, U., Kovalev, M., Morel, T., Nardetto, N., Adibekyan, V., et al., “The SAPP pipeline for the determination of stellar abundances and atmospheric parameters of stars in the core program of the PLATO mission,” *A&A*, vol. 658, A147, 2022, doi:10.1051/0004-6361/202140863.
- Giammichele, N., Charpinet, S., Fontaine, G., Brassard, P., Green, E. M., Van Grootel, V., Bergeron, P., Zong, W., and Dupret, M. A., “A large oxygen-dominated core from the seismic cartography of a pulsating white dwarf,” *Nature*, vol. 554, no. 7690, pp. 73–76, 2018, doi:10.1038/nature25136.

- Goldreich, P., Murray, N., Willette, G., and Kumar, P., “Implications of Solar p-Mode Frequency Shifts,” *ApJ*, vol. 370, p. 752, 1991, doi:10.1086/169858.
- Gough, D. O., “Comments on Helioseismic Inference,” in Osaki, Y. and Shibahashi, H. (editors), “Progress of Seismology of the Sun and Stars,” vol. 367, p. 283, Springer-Verlag, 1990, doi:10.1007/3-540-53091-610.1007/3-540-53091-6_93.
- Gough, D. O., “Linear adiabatic stellar pulsation.” in “Astrophysical Fluid Dynamics - Les Houches 1987,” pp. 399–560, 1993.
- Gough, D. O. and Kosovichev, A. G., “Initial asteroseismic inversions,” in Weiss, W. W. and Baglin, A. (editors), “IAU Colloq. 137: Inside the Stars,” *Astronomical Society of the Pacific Conference Series*, vol. 40, p. 541, 1993.
- Gough, D. O. and Thompson, M. J., “The inversion problem.” in Cox, A. N., Livingston, W. C., and Matthews, M. S. (editors), “Solar Interior and Atmosphere,” pp. 519–561, University of Arizona Press, 1991.
- Grevesse, N. and Sauval, A. J., “Standard Solar Composition,” *Space Sci. Rev.*, vol. 85, pp. 161–174, 1998, doi:10.1023/A:1005161325181.
- Gruberbauer, M., Guenther, D. B., and Kallinger, T., “Toward a New Kind of Asteroseismic Grid Fitting,” *ApJ*, vol. 749, no. 2, 109, 2012, doi:10.1088/0004-637X/749/2/109.
- Gruberbauer, M., Guenther, D. B., MacLeod, K., and Kallinger, T., “Bayesian asteroseismology of 23 solar-like Kepler targets,” *MNRAS*, vol. 435, no. 1, pp. 242–254, 2013, doi:10.1093/mnras/stt1289.
- Grundahl, F., Fredslund Andersen, M., Christensen-Dalsgaard, J., Antoci, V., Kjeldsen, H., Handberg, R., Houdek, G., Bedding, T. R., Pallé, P. L., Jessen-Hansen, J., et al., “First Results from the Hertzsprung SONG Telescope: Asteroseismology of the G5 Subgiant Star μ Herculis,” *ApJ*, vol. 836, no. 1, 142, 2017, doi:10.3847/1538-4357/836/1/142.
- Grundahl, F., Kjeldsen, H., Christensen-Dalsgaard, J., Arentoft, T., and Frandsen, S., “Stellar Oscillations Network Group,” *Communications in Asteroseismology*, vol. 150, p. 300, 2007, doi:10.1553/cia150s300.
- Guo, Z. and Jiang, C., “Asteroseismic determination of fundamental parameters for exoplanet host stars with deep learning,” *Astronomy and Computing*, vol. 42, 100686, 2023, doi:10.1016/j.ascom.2023.100686.
- Hauschildt, P. H., Allard, F., and Baron, E., “The NextGen Model Atmosphere Grid for $3000_i=T_{eff_i}=10,000$ K,” *ApJ*, vol. 512, no. 1, pp. 377–385, 1999a, doi:10.1086/306745.
- Hauschildt, P. H., Allard, F., Ferguson, J., Baron, E., and Alexander, D. R., “The NEXTGEN Model Atmosphere Grid. II. Spherically Symmetric Model Atmospheres for Giant Stars with Effective Temperatures between 3000 and 6800 K,” *ApJ*, vol. 525, no. 2, pp. 871–880, 1999b, doi:10.1086/307954.
- Hekker, S. and Christensen-Dalsgaard, J., “Giant star seismology,” *A&A Rev.*, vol. 25, no. 1, 1, 2017, doi:10.1007/s00159-017-0101-x.
- Henneco, J., Schneider, F. R. N., Hekker, S., and Aerts, C., “Merger seismology: Distinguishing massive merger products from genuine single stars using asteroseismology,” *A&A*, vol. 690, A65, 2024, doi:10.1051/0004-6361/202450508.
- Herwig, F., “The evolution of AGB stars with convective overshoot,” *A&A*, vol. 360, pp. 952–968, 2000, doi:10.48550/arXiv.astro-ph/0007139.
- Hon, M., Bellinger, E. P., Hekker, S., Stello, D., and Kuszlewicz, J. S., “Asteroseismic inference of subgiant evolutionary parameters with deep learning,” *MNRAS*, vol. 499,

- no. 2, pp. 2445–2461, 2020, doi:10.1093/mnras/staa2853.
- Iglesias, C. A. and Rogers, F. J., “Radiative opacities for carbon- and oxygen-rich mixtures,” *ApJ*, vol. 412, pp. 752–760, 1993, doi:10.1086/172958.
- Iglesias, C. A. and Rogers, F. J., “Updated Opal Opacities,” *ApJ*, vol. 464, p. 943, 1996, doi:10.1086/177381.
- Irwin, A. W., “The FreeEOS Code for Calculating the Equation of State for Stellar Interiors,” , 2004.
- Itoh, N., Hayashi, H., Nishikawa, A., and Kohyama, Y., “Neutrino Energy Loss in Stellar Interiors. VII. Pair, Photo-, Plasma, Bremsstrahlung, and Recombination Neutrino Processes,” *ApJS*, vol. 102, p. 411, 1996, doi:10.1086/192264.
- Jermyn, A. S., Bauer, E. B., Schwab, J., Farmer, R., Ball, W. H., Bellinger, E. P., Dotter, A., Joyce, M., Marchant, P., Mombarg, J. S. G., et al., “Modules for Experiments in Stellar Astrophysics (MESA): Time-Dependent Convection, Energy Conservation, Automatic Differentiation, and Infrastructure,” *arXiv e-prints*, arXiv:2208.03651, 2022.
- Jermyn, A. S., Bauer, E. B., Schwab, J., Farmer, R., Ball, W. H., Bellinger, E. P., Dotter, A., Joyce, M., Marchant, P., Mombarg, J. S. G., et al., “Modules for Experiments in Stellar Astrophysics (MESA): Time-dependent Convection, Energy Conservation, Automatic Differentiation, and Infrastructure,” *ApJS*, vol. 265, no. 1, 15, 2023a, doi:10.3847/1538-4365/acae8d.
- Jermyn, A. S., Bauer, E. B., Schwab, J., Farmer, R., Ball, W. H., Bellinger, E. P., Dotter, A., Joyce, M., Marchant, P., Mombarg, J. S. G., et al., “Modules for Experiments in Stellar Astrophysics (MESA): Time-dependent Convection, Energy Conservation, Automatic Differentiation, and Infrastructure,” *ApJS*, vol. 265, no. 1, 15, 2023b, doi:10.3847/1538-4365/acae8d.
- Jermyn, A. S., Schwab, J., Bauer, E., Timmes, F. X., and Potekhin, A. Y., “Skye: A Differentiable Equation of State,” *ApJ*, vol. 913, no. 1, 72, 2021, doi:10.3847/1538-4357/abf48e.
- Jiang, C. and Gizon, L., “BESTP - An automated Bayesian modeling tool for asteroseismology,” *Research in Astronomy and Astrophysics*, vol. 21, no. 9, 226, 2021, doi:10.1088/1674-4527/21/9/226.
- Joyce, M. and Tayar, J., “A Review of the Mixing Length Theory of Convection in 1D Stellar Modeling,” *Galaxies*, vol. 11, no. 3, 75, 2023, doi:10.3390/galaxies11030075.
- Kiefer, R. and Broomhall, A.-M., “Empirical relations for the sensitivities of solar-like oscillations to magnetic perturbations,” *MNRAS*, vol. 496, no. 4, pp. 4593–4605, 2020, doi:10.1093/mnras/staa1807.
- Kippenhahn, R., Weigert, A., and Weiss, A., *Stellar Structure and Evolution*, Springer, 2013, doi:10.1007/978-3-642-30304-3.
- Kjeldsen, H. and Bedding, T. R., “Amplitudes of stellar oscillations: the implications for asteroseismology.” *A&A*, vol. 293, pp. 87–106, 1995, doi:10.48550/arXiv.astro-ph/9403015.
- Kjeldsen, H., Bedding, T. R., and Christensen-Dalsgaard, J., “Correcting Stellar Oscillation Frequencies for Near-Surface Effects,” *ApJ*, vol. 683, no. 2, p. L175, 2008, doi:10.1086/591667.
- Kjeldsen, H., Bedding, T. R., Viskum, M., and Frandsen, S., “Solarlike Oscillations in eta Boo,” *AJ*, vol. 109, p. 1313, 1995, doi:10.1086/117363.
- Koch, D. G., Borucki, W. J., Basri, G., Batalha, N. M., Brown, T. M., Caldwell, D.,

- Christensen-Dalsgaard, J., Cochran, W. D., DeVore, E., Dunham, E. W., et al., “Kepler Mission Design, Realized Photometric Performance, and Early Science,” *ApJ*, vol. 713, no. 2, pp. L79–L86, 2010, doi:10.1088/2041-8205/713/2/L79.
- Kosovichev, A. G., “Inversion methods in helioseismology and solar tomography.” *Journal of Computational and Applied Mathematics*, vol. 109, no. 1, pp. 1–39, 1999.
- Kosovichev, A. G., “Advances in Global and Local Helioseismology: An Introductory Review,” in Rozelot, J.-P. and Neiner, C. (editors), “Lecture Notes in Physics, Berlin Springer Verlag,” vol. 832, p. 3, Springer-Verlag, 2011, doi:10.1007/978-3-642-19928-8_1.
- Kosovichev, A. G. and Kitiashvili, I. N., “Resolving Power of Asteroseismic Inversion of the Kepler Legacy Sample,” in Kosovichev, A., Strassmeier, S., and Jardine, M. (editors), “Solar and Stellar Magnetic Fields: Origins and Manifestations,” *IAU Symposium*, vol. 354, pp. 107–115, 2020, doi:10.1017/S1743921320001416.
- Kuhfuss, R., “A model for time-dependent turbulent convection,” *A&A*, vol. 160, no. 1, pp. 116–120, 1986.
- Kumar, P., Franklin, J., and Goldreich, P., “Distribution Functions for the Time-averaged Energies of Stochastically Excited Solar p-Modes,” *ApJ*, vol. 328, p. 879, 1988, doi:10.1086/166345.
- Kurtz, D. W., “Asteroseismology Across the Hertzsprung–Russell Diagram,” *Annual Review of Astronomy and Astrophysics*, vol. 60, no. Volume 60, 2022, pp. 31–71, 2022, doi:https://doi.org/10.1146/annurev-astro-052920-094232.
- Kurtz, D. W., Saio, H., Takata, M., Shibahashi, H., Murphy, S. J., and Sekii, T., “Asteroseismic measurement of surface-to-core rotation in a main-sequence A star, KIC 11145123,” *MNRAS*, vol. 444, no. 1, pp. 102–116, 2014, doi:10.1093/mnras/stu1329.
- Langanke, K. and Martínez-Pinedo, G., “Shell-model calculations of stellar weak interaction rates: II. Weak rates for nuclei in the mass range $A=45-65$ in supernovae environments,” *Nuclear Physics A*, vol. 673, pp. 481–508, 2000, doi:10.1016/S0375-9474(00)00131-7.
- Lebreton, Y. and Goupil, M. J., “Seismic signature of envelope penetrative convection: the CoRoT star HD 52265,” *A&A*, vol. 544, L13, 2012, doi:10.1051/0004-6361/201220000.
- Ledoux, P. and Walraven, T., “Variable Stars.” *Handbuch der Physik*, vol. 51, pp. 353–604, 1958, doi:10.1007/978-3-642-45908-5_6.
- Leighton, R. B., Noyes, R. W., and Simon, G. W., “Velocity Fields in the Solar Atmosphere. I. Preliminary Report.” *ApJ*, vol. 135, p. 474, 1962, doi:10.1086/147285.
- Levenberg, K., “A method for the solution of certain non-linear problems in least squares,” *Quart. Appl. Math.*, vol. 2, pp. 164–168, 1944, doi:https://doi.org/10.1090/qam/10666.
- Li, G., Deheuvels, S., Ballot, J., and Lignières, F., “Magnetic fields of 30 to 100 kG in the cores of red giant stars,” *Nature*, vol. 610, no. 7930, pp. 43–46, 2022, doi:10.1038/s41586-022-05176-0.
- Li, G., Deheuvels, S., Li, T., Ballot, J., and Lignières, F., “Internal magnetic fields in 13 red giants detected by asteroseismology,” *A&A*, vol. 680, A26, 2023, doi:10.1051/0004-6361/202347260.
- Li, Y., Bedding, T. R., Li, T., Bi, S., Stello, D., Zhou, Y., and White, T. R., “Asteroseismology of 36 Kepler subgiants - I. Oscillation frequencies, linewidths, and amplitudes,” *MNRAS*, vol. 495, no. 2, pp. 2363–2386, 2020, doi:10.1093/mnras/staa1335.
- Li, Y. and Joyce, M., “Beyond MESA Defaults: The Impact of Structural Resolution

- Uncertainty in p-mode Asteroseismology,” *arXiv e-prints*, arXiv:2501.13207, 2025, doi:10.48550/arXiv.2501.13207.
- Lindsay, C. J., Ong, J. M. J., and Basu, S., “Fossil Signatures of Main-sequence Convective Core Overshoot Estimated through Asteroseismic Analyses,” *ApJ*, vol. 965, no. 2, 171, 2024, doi:10.3847/1538-4357/ad2ae5.
- Lund, M. N., Silva Aguirre, V., Davies, G. R., Chaplin, W. J., Christensen-Dalsgaard, J., Houdek, G., White, T. R., Bedding, T. R., Ball, W. H., Huber, D., et al., “Standing on the Shoulders of Dwarfs: the Kepler Asteroseismic LEGACY Sample. I. Oscillation Mode Parameters,” *ApJ*, vol. 835, no. 2, 172, 2017, doi:10.3847/1538-4357/835/2/172.
- Magg, E., Bergemann, M., Serenelli, A., Bautista, M., Plez, B., Heiter, U., Gerber, J. M., Ludwig, H.-G., Basu, S., Ferguson, J. W., et al., “Observational constraints on the origin of the elements. IV. Standard composition of the Sun,” *A&A*, vol. 661, A140, 2022, doi:10.1051/0004-6361/202142971.
- Marigo, P. and Aringer, B., “Low-temperature gas opacity. *ÆSOPUS*: a versatile and quick computational tool,” *A&A*, vol. 508, no. 3, pp. 1539–1569, 2009, doi:10.1051/0004-6361/200912598.
- Mathur, S., Huber, D., Batalha, N. M., Ciardi, D. R., Bastien, F. A., Bieryla, A., Buchhave, L. A., Cochran, W. D., Endl, M., Esquerdo, G. A., et al., “Revised Stellar Properties of Kepler Targets for the Q1-17 (DR25) Transit Detection Run,” *The Astrophysical Journal Supplement Series*, vol. 229, no. 2, p. 30, 2017, doi:10.3847/1538-4365/229/2/30.
- Metcalf, T. S. and Charbonneau, P., “Stellar structure modeling using a parallel genetic algorithm for objective global optimization,” *Journal of Computational Physics*, vol. 185, no. 1, pp. 176–193, 2003, doi:10.1016/S0021-9991(02)00053-0.
- Metcalf, T. S., Creevey, O. L., and Christensen-Dalsgaard, J., “A Stellar Model-fitting Pipeline for Asteroseismic Data from the Kepler Mission,” *ApJ*, vol. 699, no. 1, pp. 373–382, 2009, doi:10.1088/0004-637X/699/1/373.
- Metcalf, T. S., Creevey, O. L., Doğan, G., Mathur, S., Xu, H., Bedding, T. R., Chaplin, W. J., Christensen-Dalsgaard, J., Karoff, C., Trampedach, R., et al., “Properties of 42 Solar-type Kepler Targets from the Asteroseismic Modeling Portal,” *ApJS*, vol. 214, no. 2, 27, 2014, doi:10.1088/0067-0049/214/2/27.
- Metcalf, T. S., Townsend, R. H. D., and Ball, W. H., “Overview and Validation of the Asteroseismic Modeling Portal v2.0,” *Research Notes of the American Astronomical Society*, vol. 7, no. 8, 164, 2023, doi:10.3847/2515-5172/acebef.
- Michaud, G., Alecian, G., and Richer, J., *Atomic Diffusion in Stars*, Springer, 2015, doi:10.1007/978-3-319-19854-5.
- Miglio, A. and Montalbán, J., “Constraining fundamental stellar parameters using seismology. Application to α Centauri AB,” *A&A*, vol. 441, no. 2, pp. 615–629, 2005, doi:10.1051/0004-6361:20052988.
- Moedas, N., Bossini, D., Deal, M., and Cunha, M. S., “Characterisation of FG-type stars with improved transport of chemical elements,” *A&A*, vol. 684, A113, 2024, doi:10.1051/0004-6361/202348506.
- Moedas, N., Deal, M., Bossini, D., and Campilho, B., “Atomic diffusion and turbulent mixing in solar-like stars: Impact on the fundamental properties of FG-type stars,” *A&A*, vol. 666, A43, 2022, doi:10.1051/0004-6361/202243210.
- Morel, T., Creevey, O. L., Montalbán, J., Miglio, A., and Willett, E., “Testing abundance-age

- relations beyond solar analogues with Kepler LEGACY stars,” *Astronomy & Astrophysics*, vol. 646, p. A78, 2021, doi:10.1051/0004-6361/202039212.
- Mosser, B., Goupil, M. J., Belkacem, K., Michel, E., Stello, D., Marques, J. P., Elsworth, Y., Barban, C., Beck, P. G., Bedding, T. R., et al., “Probing the core structure and evolution of red giants using gravity-dominated mixed modes observed with Kepler,” *A&A*, vol. 540, A143, 2012, doi:10.1051/0004-6361/201118519.
- Nelder, J. A. and Mead, R., “A Simplex Method for Function Minimization,” *The Computer Journal*, vol. 7, no. 4, pp. 308–313, 1965, doi:10.1093/comjnl/7.4.308.
- Noll, A. and Deheuvels, S., “Impact of central mixing scheme and nuclear reaction network on the extent of convective cores,” *A&A*, vol. 676, A70, 2023, doi:10.1051/0004-6361/202245710.
- Noll, A., Deheuvels, S., and Ballot, J., “Probing core overshooting using subgiant asteroseismology: The case of KIC10273246,” *A&A*, vol. 647, A187, 2021, doi:10.1051/0004-6361/202040055.
- Nsamba, B., Campante, T. L., Monteiro, M. J. P. F. G., Cunha, M. S., Rendle, B. M., Reese, D. R., and Verma, K., “Asteroseismic modelling of solar-type stars: internal systematics from input physics and surface correction methods,” *MNRAS*, vol. 477, no. 4, pp. 5052–5063, 2018, doi:10.1093/mnras/sty948.
- Oda, T., Hino, M., Muto, K., Takahara, M., and Sato, K., “Rate Tables for the Weak Processes of sd-Shell Nuclei in Stellar Matter,” *Atomic Data and Nuclear Data Tables*, vol. 56, pp. 231–403, 1994, doi:10.1006/adnd.1994.1007.
- Ong, J. M. J. and Basu, S., “Semianalytic Expressions for the Isolation and Coupling of Mixed Modes,” *ApJ*, vol. 898, no. 2, 127, 2020, doi:10.3847/1538-4357/ab9ffb.
- Ong, J. M. J., Basu, S., Lund, M. N., Bieryla, A., Viani, L. S., and Latham, D. W., “Mixed Modes and Asteroseismic Surface Effects. II. Subgiant Systematics,” *ApJ*, vol. 922, no. 1, 18, 2021a, doi:10.3847/1538-4357/ac1e8b.
- Ong, J. M. J., Basu, S., and Roxburgh, I. W., “Mixed Modes and Asteroseismic Surface Effects. I. Analytic Treatment,” *ApJ*, vol. 920, no. 1, 8, 2021b, doi:10.3847/1538-4357/ac12ca.
- Osaki, Y., “Nonradial oscillations of a 10 solar mass star in the main-sequence stage.” *PASJ*, vol. 27, no. 2, pp. 237–258, 1975.
- Paxton, B., Bildsten, L., Dotter, A., Herwig, F., Lesaffre, P., and Timmes, F., “Modules for Experiments in Stellar Astrophysics (MESA),” *ApJS*, vol. 192, 3, 2011a, doi:10.1088/0067-0049/192/1/3.
- Paxton, B., Bildsten, L., Dotter, A., Herwig, F., Lesaffre, P., and Timmes, F., “Modules for Experiments in Stellar Astrophysics (MESA),” *ApJS*, vol. 192, no. 1, 3, 2011b, doi:10.1088/0067-0049/192/1/3.
- Paxton, B., Cantiello, M., Arras, P., Bildsten, L., Brown, E. F., Dotter, A., Mankovich, C., Montgomery, M. H., Stello, D., Timmes, F. X., et al., “Modules for Experiments in Stellar Astrophysics (MESA): Planets, Oscillations, Rotation, and Massive Stars,” *ApJS*, vol. 208, 4, 2013a, doi:10.1088/0067-0049/208/1/4.
- Paxton, B., Cantiello, M., Arras, P., Bildsten, L., Brown, E. F., Dotter, A., Mankovich, C., Montgomery, M. H., Stello, D., Timmes, F. X., et al., “Modules for Experiments in Stellar Astrophysics (MESA): Planets, Oscillations, Rotation, and Massive Stars,” *ApJS*, vol. 208, no. 1, 4, 2013b, doi:10.1088/0067-0049/208/1/4.

- Paxton, B., Marchant, P., Schwab, J., Bauer, E. B., Bildsten, L., Cantiello, M., Dessart, L., Farmer, R., Hu, H., Langer, N., et al., “Modules for Experiments in Stellar Astrophysics (MESA): Binaries, Pulsations, and Explosions,” *ApJS*, vol. 220, 15, 2015a, doi:10.1088/0067-0049/220/1/15.
- Paxton, B., Marchant, P., Schwab, J., Bauer, E. B., Bildsten, L., Cantiello, M., Dessart, L., Farmer, R., Hu, H., Langer, N., et al., “Modules for Experiments in Stellar Astrophysics (MESA): Binaries, Pulsations, and Explosions,” *ApJS*, vol. 220, no. 1, 15, 2015b, doi:10.1088/0067-0049/220/1/15.
- Paxton, B., Schwab, J., Bauer, E. B., Bildsten, L., Blinnikov, S., Duffell, P., Farmer, R., Goldberg, J. A., Marchant, P., Sorokina, E., et al., “Modules for Experiments in Stellar Astrophysics (MESA): Convective Boundaries, Element Diffusion, and Massive Star Explosions,” *ApJS*, vol. 234, 34, 2018, doi:10.3847/1538-4365/aaa5a8.
- Paxton, B., Smolec, R., Schwab, J., Gautschy, A., Bildsten, L., Cantiello, M., Dotter, A., Farmer, R., Goldberg, J. A., Jermyn, A. S., et al., “Modules for Experiments in Stellar Astrophysics (MESA): Pulsating Variable Stars, Rotation, Convective Boundaries, and Energy Conservation,” *ApJS*, vol. 243, no. 1, 10, 2019a, doi:10.3847/1538-4365/ab2241.
- Paxton, B., Smolec, R., Schwab, J., Gautschy, A., Bildsten, L., Cantiello, M., Dotter, A., Farmer, R., Goldberg, J. A., Jermyn, A. S., et al., “Modules for Experiments in Stellar Astrophysics (MESA): Pulsating Variable Stars, Rotation, Convective Boundaries, and Energy Conservation,” *ApJS*, vol. 243, no. 1, 10, 2019b, doi:10.3847/1538-4365/ab2241.
- Pijpers, F. P., *Methods in helio- and asteroseismology*, Imperial College Press, 2006.
- Pijpers, F. P. and Thompson, M. J., “Faster formulations of the optimally localized averages method for helioseismic inversions,” *A&A*, vol. 262, no. 2, pp. L33–L36, 1992.
- Pijpers, F. P. and Thompson, M. J., “The SOLA method for helioseismic inversion,” *A&A*, vol. 281, no. 1, pp. 231–240, 1994.
- Pinsonneault, M. H., Zinn, J. C., Tayar, J., Serenelli, A., García, R. A., Mathur, S., Vrad, M., Elsworth, Y. P., Mosser, B., Stello, D., et al., “APOKASC-3: The Third Joint Spectroscopic and Asteroseismic Catalog for Evolved Stars in the Kepler Fields,” *ApJS*, vol. 276, no. 2, 69, 2025, doi:10.3847/1538-4365/ad9fef.
- Rabello-Soares, M. C., Basu, S., and Christensen-Dalsgaard, J., “A Study of the Parameters for Solar Structure Inversion Methods,” in Korzennik, S. (editor), “Structure and Dynamics of the Interior of the Sun and Sun-like Stars,” *ESA Special Publication*, vol. 418, p. 505, 1998.
- Rauer, H., Aerts, C., Cabrera, J., Deleuil, M., Erikson, A., Gizon, L., Goupil, M., Heras, A., Lorenzo-Alvarez, J., Marliani, F., et al., “The PLATO Mission,” *arXiv e-prints*, arXiv:2406.05447, 2024, doi:10.48550/arXiv.2406.05447.
- Rauer, H., Catala, C., Aerts, C., Appourchaux, T., Benz, W., Brandeker, A., Christensen-Dalsgaard, J., Deleuil, M., Gizon, L., Goupil, M. J., et al., “The PLATO 2.0 mission,” *Experimental Astronomy*, vol. 38, no. 1-2, pp. 249–330, 2014, doi:10.1007/s10686-014-9383-4.
- Reese, D. R., Marques, J. P., Goupil, M. J., Thompson, M. J., and Deheuvels, S., “Estimating stellar mean density through seismic inversions,” *A&A*, vol. 539, A63, 2012, doi:10.1051/0004-6361/201118156.
- Rendle, B. M., Buldgen, G., Miglio, A., Reese, D., Noels, A., Davies, G. R., Campante, T. L., Chaplin, W. J., Lund, M. N., Kuszlewicz, J. S., et al., “AIMS - a new tool for stellar parameter determinations using asteroseismic constraints,” *MNRAS*, vol. 484, no. 1, pp.

- 771–786, 2019, doi:10.1093/mnras/stz031.
- Rogers, F. J. and Nayfonov, A., “Updated and Expanded OPAL Equation-of-State Tables: Implications for Helioseismology,” *ApJ*, vol. 576, pp. 1064–1074, 2002, doi:10.1086/341894.
- Roxburgh, I., Audard, N., Basu, S., Christensen-Dalsgaard, J., and Vorontsov, S., “Inversion for the internal structure of an evolved small-mass star using modes with $l=0-3$,” in Provost, J. and Schmider, F. (editors), “Proc. IAU Symp. 181: Sounding Solar and Stellar Interiors (poster vol.),” p. 245, Observatoire de la Côte d’Azur, Université de Nice, 1998.
- Roxburgh, I. W., “Anomalies in the Kepler Asteroseismic Legacy Project Data A re-analysis of 16 Cyg A & B, KIC 8379927 and 6 solar-like stars,” *A&A*, vol. 604, A42, 2017, doi:10.1051/0004-6361/201731057.
- Roxburgh, I. W. and Vorontsov, S. V., “The ratio of small to large separations of acoustic oscillations as a diagnostic of the interior of solar-like stars,” *A&A*, vol. 411, pp. 215–220, 2003, doi:10.1051/0004-6361:20031318.
- Salabert, D., Régulo, C., Pérez Hernández, F., and García, R. A., “Frequency dependence of p-mode frequency shifts induced by magnetic activity in Kepler solar-like stars,” *A&A*, vol. 611, A84, 2018, doi:10.1051/0004-6361/201731714.
- Santos, A. R. G., Campante, T. L., Chaplin, W. J., Cunha, M. S., Lund, M. N., Kiefer, R., Salabert, D., García, R. A., Davies, G. R., Elsworth, Y., et al., “Signatures of Magnetic Activity in the Seismic Data of Solar-type Stars Observed by Kepler,” *ApJS*, vol. 237, no. 1, 17, 2018, doi:10.3847/1538-4365/aac9b6.
- Santos, A. R. G., Campante, T. L., Chaplin, W. J., Cunha, M. S., Lund, M. N., Kiefer, R., Salabert, D., García, R. A., Davies, G. R., Elsworth, Y., et al., “Signatures of Magnetic Activity in the Seismic Data of Solar-type Stars Observed by Kepler,” *The Astrophysical Journal Supplement Series*, vol. 237, no. 1, p. 17, 2018, doi:10.3847/1538-4365/aac9b6.
- Saumon, D., Chabrier, G., and van Horn, H. M., “An Equation of State for Low-Mass Stars and Giant Planets,” *ApJS*, vol. 99, p. 713, 1995, doi:10.1086/192204.
- Seaton, M. J., “Opacity Project data on CD for mean opacities and radiative accelerations,” *MNRAS*, vol. 362, no. 1, pp. L1–L3, 2005, doi:10.1111/j.1365-2966.2005.00019.x.
- Shibahashi, H., “Modal Analysis of Stellar Nonradial Oscillations by an Asymptotic Method,” *PASJ*, vol. 31, pp. 87–104, 1979.
- Silva Aguirre, V., Davies, G. R., Basu, S., Christensen-Dalsgaard, J., Creevey, O., Metcalfe, T. S., Bedding, T. R., Casagrande, L., Handberg, R., Lund, M. N., et al., “Ages and fundamental properties of Kepler exoplanet host stars from asteroseismology,” *MNRAS*, vol. 452, no. 2, pp. 2127–2148, 2015, doi:10.1093/mnras/stv1388.
- Silva Aguirre, V., Lund, M. N., Antia, H. M., Ball, W. H., Basu, S., Christensen-Dalsgaard, J., Lebreton, Y., Reese, D. R., Verma, K., Casagrande, L., et al., “Standing on the Shoulders of Dwarfs: the Kepler Asteroseismic LEGACY Sample. II. Radii, Masses, and Ages,” *ApJ*, vol. 835, no. 2, 173, 2017, doi:10.3847/1538-4357/835/2/173.
- Sobol’, I., “On the distribution of points in a cube and the approximate evaluation of integrals,” *USSR Computational Mathematics and Mathematical Physics*, vol. 7, no. 4, pp. 86–112, 1967, doi:https://doi.org/10.1016/0041-5553(67)90144-9.
- Stokholm, A., Nissen, P. E., Silva Aguirre, V., White, T. R., Lund, M. N., Mosumgaard, J. R., Huber, D., and Jessen-Hansen, J., “The subgiant HR 7322 as an asteroseismic benchmark star,” *MNRAS*, vol. 489, no. 1, pp. 928–940, 2019, doi:10.1093/mnras/stz2222.

- Takata, M., “Analysis of Adiabatic Dipolar Oscillations of Stars,” PASJ, vol. 58, pp. 893–908, 2006, doi:10.1093/pasj/58.5.893.
- Tassoul, M., “Asymptotic approximations for stellar nonradial pulsations.” ApJS, vol. 43, pp. 469–490, 1980, doi:10.1086/190678.
- Teixeira, T. C., Christensen-Dalsgaard, J., Carrier, F., Aerts, C., Frandsen, S., Stello, D., Maas, T., Burnet, M., Bruntt, H., de Medeiros, J. R., et al., “Giant Vibrations in Dip,” Ap&SS, vol. 284, no. 1, pp. 233–236, 2003.
- Thompson, M. J. and Christensen-Dalsgaard, J., “On inverting asteroseismic data,” in Battrick, B., Favata, F., Roxburgh, I. W., and Galadi, D. (editors), “Stellar Structure and Habitable Planet Finding,” *ESA Special Publication*, vol. 485, pp. 95–101, 2002, doi:10.48550/arXiv.astro-ph/0110447.
- Townsend, R. H. D., Goldstein, J., and Zweibel, E. G., “Angular momentum transport by heat-driven g-modes in slowly pulsating B stars,” MNRAS, vol. 475, no. 1, pp. 879–893, 2018, doi:10.1093/mnras/stx3142.
- Townsend, R. H. D. and Teitler, S. A., “GYRE: an open-source stellar oscillation code based on a new Magnus Multiple Shooting scheme,” MNRAS, vol. 435, no. 4, pp. 3406–3418, 2013, doi:10.1093/mnras/stt1533.
- Triana, S. A., Corsaro, E., De Ridder, J., Bonanno, A., Pérez Hernández, F., and García, R. A., “Internal rotation of 13 low-mass low-luminosity red giants in the Kepler field,” A&A, vol. 602, A62, 2017, doi:10.1051/0004-6361/201629186.
- Unno, W., Osaki, Y., Ando, H., Saio, H., and Shibahashi, H., *Nonradial oscillations of stars*, University of Tokyo Press, 1989.
- Vandakurov, Y. V., “The Frequency Distribution of Stellar Oscillations.” AZh, vol. 44, p. 786, 1967.
- Vanlaer, V., Aerts, C., Bellinger, E. P., and Christensen-Dalsgaard, J., “Feasibility of structure inversions for gravity-mode pulsators,” A&A, vol. 675, A17, 2023, doi:10.1051/0004-6361/202245597.
- Verma, K., Raodeo, K., Antia, H. M., Mazumdar, A., Basu, S., Lund, M. N., and Silva Aguirre, V., “Seismic Measurement of the Locations of the Base of Convection Zone and Helium Ionization Zone for Stars in the Kepler Seismic LEGACY Sample,” ApJ, vol. 837, no. 1, 47, 2017, doi:10.3847/1538-4357/aa5da7.
- Verma, K. and Silva Aguirre, V., “Helium settling in F stars: constraining turbulent mixing using observed helium glitch signature,” MNRAS, vol. 489, no. 2, pp. 1850–1858, 2019, doi:10.1093/mnras/stz2272.
- Wang, S. and Zhang, Q.-S., “Asteroseismology of 16 Kepler Solar-like Stars: Stellar Parameters and the Effects of Element Diffusion,” *Research in Astronomy and Astrophysics*, vol. 23, no. 7, 075017, 2023, doi:10.1088/1674-4527/acd58f.
- Zahn, J. P., “Convective penetration in stellar interiors.” A&A, vol. 252, pp. 179–188, 1991.
- Zhang, J., “Is there large convective-core overshooting in Kepler targets KIC 2837475 and 11081729?” MNRAS, vol. 497, no. 4, pp. 4042–4050, 2020, doi:10.1093/mnras/staa2199.

Acknowledgments

It has been a wonderful 3.5 years in Heidelberg and for that there are many people I need to thank.

First, I would like to thank all the people at HITS who have made life easy enough for me to focus on my research. This includes the kitchen and custodial staff who kept me well-fed and the offices clean, the IT staff who kept the computing clusters running, and the HR and accounting departments for assisting with residence permit issues and also my many business trips. A very special thank you to Kristin, whose presence in the TOS group immediately lowered the stress level of everyone.

When I chose my specific project, I was warned that it was one of the more difficult options (not that any PhD project is easy). Fortunately, this project also came with built-in support from a full advising team. Sarbani, thank you for sharing your deep knowledge of stellar structure and helping me develop my own intuition for structure inversions. Thank you also for the kick to get my applications started and to aim a bit higher with them.

Earl, thank you for all the support, scientific and otherwise, and also for getting me connected to the broader MESA community. You have set a high bar for “postdoc who stays involved to help the next PhD student to pick up the project.” I’ll do my best to carry your example forward.

Saskia, I deeply appreciate your guidance on doing science and doing a career in science. I have also benefited enormously from the push to “say what you mean” when writing about my work. I can already see this skill being applied far beyond my paper writing.

Over the course of my PhD, I have had the good fortune to travel and meet new friends and collaborators around the world. Of these people, I own the most thanks to the MESA Down Under organizing committee: May, Giulia, and Jared. I think that our teamwork has spoiled me forever. After every meeting, even the ones that kept me up till midnight, I was so deeply grateful for your enthusiasm and insights.

As I was finding my feet in Heidelberg, I often had to remind myself that I was doing a hard thing (a PhD) on hard mode (in a different country far from home). When I started feeling like a part of the community (and dare I say, found family) at HITS, things got much easier. To that end, I owe a huge debt of gratitude to all of the friends I have made here.

To TOS members past and present, Daria, Julian, Teresa, Alba, Anastasia, Lucas, Tobias, Jan, Bea, Fran, Jonas, Jeong, Felix, Anthony, and Jordan: thank you for all the coffee breaks, movie nights, and for being the best moving crew I've ever seen. I specifically need to thank Nathalie for setting the precedent that this is a group that cares deeply for one another. Last, but certainly not least, Quentin, it has been an honor to be PhD/desk buddies with you for the last 3.5 years. We said we'd get through this together and the end is in sight.

The community I have found here extends far beyond the TOS group including: Anna, Javier, Lukrécia, Jeff, Rajika, Mike, Marco, Roel, Mathias, Alex, Alessandro, Laura, and Andreas. I am deeply appreciative for your friendship in all its forms (venting sessions, distractions, bouldering buddies, etc.) Rhys, your friendship has been invaluable over the last few years. I have grown in ways I never would have thought possible.

To Ali, it was really important to me to have the perspective of a friend not pursuing an academic career, and through knowing you I have managed to find several. I am inspired by the actions you take to care for everyone around you. To the whole Monday workout crew: our sessions kept me physically strong, but more importantly mentally healthy.

There are also many people in my life who have helped me become the kind of person who can survive and thrive as a PhD student in another country.

To my Wichita climbing crew, Alec, Jeff, Ollie, Thane, Michael, Mikael, Lyle, Tony, Hannah: watching the eclipse with you was one of the most sacred experiences I've had. Although the jokes are just as immature, it has been a joy to see us all grow up and deepen our care for each other.

To Alex, I don't have the words for you much our nearly 10 year friendship means to me, so I will simply say: I love you, my friend. No matter how crappy your couch, I will always be excited to crash with you, even (especially) when it means dealing with silly cats at 3am.

Since childhood, I have been blessed with a number of, as my dad would say, caring adults. This list is surely incomplete but thank you to Sheron, Curtis, Steve, Sue, Mary, Rob, Daryl, Randy, Russ, Ron, Pansy, Joseph, Laura, Martin, and Peter. Also on this list are Dr. Ferguson and Dr. Behrman whose fanatic teaching and kind mentorship are responsible for me starting and continuing my physics studies.

And now to try and put into words my gratitude to the three people who have known me longer anyone in the world. Steven, I think it is fair to say that we are similar people, in ways that go far beyond the values we got from our parents. In the past, I think these similarities led to destructive interference, but as we've grown up that has (slowly) shifted to constructive interference. At the very least, I'm no longer running away from hobbies purely because "that's my brother's thing." I am so proud to be your sibling.

Mom, I think you planted the seed of my decision to move abroad. The stories of your trips and our hosting of exchange students were such a constant growing up. I wanted the experiences you always talked about, to live in another country rather than just visit. There are many ways a mom could respond to her child moving to another country for at least three years. I have yet to imagine a better response than "I can't wait to come visit you!" In every way I can imagine, I am so lucky to be your kid.

Dad, you aren't here to read this but a lot has changed since our last conversations. My life path looks pretty different. Even so, I'm keeping my final promise.